Radiation Damage in Advanced Materials for Next Generation Nuclear Power Plants

Mark James Wootton

A Doctoral Thesis
Submitted in partial fulfilment of the requirements for the award of
Doctor of Philosophy at Loughborough University

September 2017

This thesis is dedicated to my wife, Shan,
for your love and support,
and for making it all worthwhile.

Abstract

The ageing state of the world's nuclear power infrastructure, and the need to reduce humanity's dependency on fossil fuels, requires that this electrical energy generating capacity is replaced. Economic factors, and its physical and chemical properties, make high purity iron-chromium binary alloys a strong candidate for use in the construction of the pressure vessels of the next generation of nuclear reactors. This relatively inexpensive metal retains the oxidation resistance property of so-called "stainless steel" alloys, and has demonstrated dimensional stability and low degradation under harsh experimental environments of temperature and radiation.

In this work, we consider radiation induced interstitial damage to the atomic lattices of iron-chromium binary alloys using the atomistic modelling methods, Molecular Dynamics and Adaptive Kinetic Monte Carlo, simulating collision cascade sequences, and the migration of defects in the aftermath. Variations in chromium content does not effect the initial damage production in terms of the number of Frenkel pairs produced, but iron and chromium atoms are not evenly distributed in defect atoms with respect to the bulk concentration. In simulations conducted at low temperature, chromium is under-represented, and at high temperature, a greater proportion of interstitial atoms are chromium than in the lattice overall. The latter phenomena is most strongly pronounced in systems of low bulk chromium content. During the simulation of post-cascade defect migration, interstitials atoms are observed to form temporary clusters and vacancies align along adjacent lattice sites, with the two types of defect also migrating to annihilate by recombination.

Calculating the energy spectra of cascade events corresponding to an example experimental configuration using the SRIM package, we investigated the evolution of lattice systems in which a sequence of multiple cascade events occurred, both with and without a physically representative time gap between events. These simulations gave us the opportunity to observe the behaviour of cascades in the proximity of damage remaining from previous events, such as the promotion of defect clustering when this occurs.

Acknowledgements

Debts of gratitude are owed to those who have enabled the completion of this thesis, and the years of work it describes. I would like to thank my supervisor, Professor Steven Kenny, for his patience and for his sagacious and insightful guidance, and EPRSC for providing the funding for this project. Additionally, I would like to thank Loughborough University for the use of their facilities during my work, in particular, their high performance computing installations – the Hydra and Hera supercomputers. I must also express my gratitude to all my colleagues in the Atomistic Modelling Group at Loughborough University and especially to Christopher Scott, Miao Yu, and Adam Lloyd. I could not have done it without you. To Pär Olsson, Giovanni Bonny, Christopher Cooper, and Peter Klaver, I would like to thank you for your illuminating conversations and correspondences, which were of great assistance to me, and to Joseph Abiy, the supervision of whose final year project I was given the opportunity to assist with, I say thank-you and good luck. Finally, for your support, both emotional and material, not to mention the proof-reading, I say a big thank-you to all of my family. I am very lucky to have you.

Additional gratitude must also be expressed towards the authors of the citations referenced in this thesis – the giants, upon whose shoulders we stand.

"It's only a model"

– Monty Python and the Holy Grail, 1975

Contents

List of Figures

List of Tables

Chapter 1

Introduction and Background

The majority of the world's nuclear reactors were built between 1970 and 1985 [1]. With public opinion turning against the construction of new nuclear power plants, following disasters such as the Chernobyl incident of 1986, we are now left with many of our reactors operating beyond their originally intended lifespans, and in need of decommissioning and replacement. For example, in the United Kingdom, nuclear power accounts for 21% of the country's electrical supply, but under the government's current schedule, just under half of the fifteen reactors active at the time of writing shall have been decommissioned by 2025 [2]. With renewable technologies having not yet reached the maturity required to form the core of most countries' civil energy infrastructures, and with traditional fossil-fuel technologies rendered unattractive by climatological, environmental, and resource availability concerns, the prospect of constructing new nuclear power installations must be taken seriously.

In the interest of efficiency, the fourth generation of nuclear power plants will be required to endure elevated temperatures and harsh radiation environments, while operating safely for upwards of six decades [3], and *in potentia* nuclear fusion devices will produce an even greater hostility of internal environment [4]. For a summary of proposed GenIV designs' anticipated operating conditions see figure 1.1.

Metals subjected to radiation are known to experience degradation of their physical properties, including swelling, embrittlement, and the segregation of their alloying elements

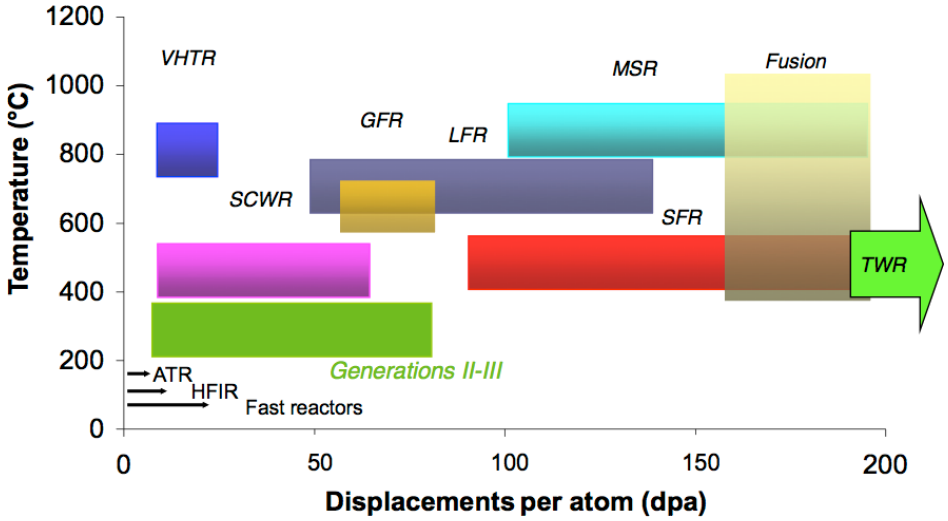

Figure 1.1: Temperature and anticipated radiation damage conditions for various nuclear reactors, given in units of degrees Celsius and displacements per atom, see section 1.1 (image from [5]). Proposed GenIV reactors: VHTR – Very High Temperature Reactor, MSR – Molten-Salt Reactor, SCWR – Super-Critical Water-cooled Reactor, GFR – Gas-cooled Fast Reactor, SFR – Sodium-cooled Fast Reactor, LFR – Lead-cooled Fast Reactor, TWR – Travelling Wave Reactor.

[6, 7], as is highly visible in figure 1.2. An important candidate material for new reactors are high purity Ferritic/Marsinetic steels, having demonstrated dimensional stability and creep resistance during radiation exposure [8–10], along with thermal shock resistance [11]. In a nuclear reactor, the form of radiation of predominant concern is that of energetic neutrons, but few facilities have the means to conduct neutron-based experimentation [12], and to do so is both expensive and time consuming, given safety concerns arising from radiation induced activation [13]. Cheaper and faster alternatives exist, such as electron, proton, light ion, or heavy ion irradiation, but none of these produce results perfectly analogous to those of neutrons [12, 14]. Furthermore, physical analysis techniques struggle to detect the damage introduced to samples by irradiation before the defects have accumulated into clusters on the order of nanometres in size [15].

For these reasons, we turn to atomistic modelling, employing the Molecular Dynamics (MD) and Adaptive Kinetic Monte Carlo[1] (AKMC) methods to simulate radiation induced collision cascades in iron-chromium binary alloys, and the recovery process that follows. It is the purpose of this work to contribute to informing the important materials engineering

[1]Not to be confused with *Atomistic Kinetic Monte Carlo*

decisions that must be considered for the construction of the next generation of nuclear power plants.

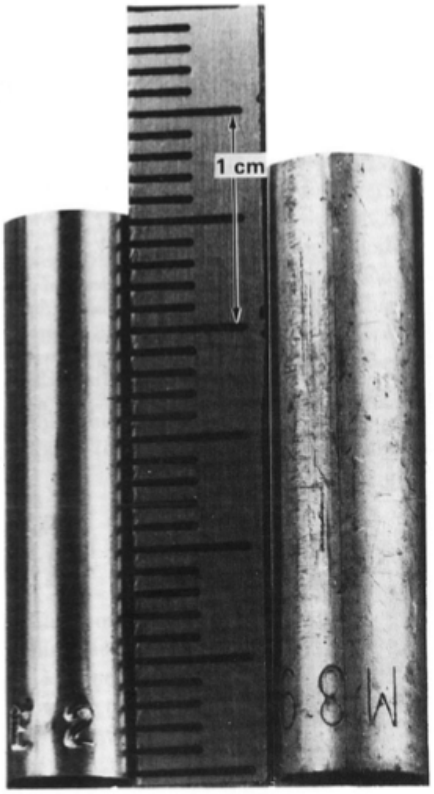

Figure 1.2: The right-hand steel rod has been irradiated using neutrons (n) of kinetic energy, $E > 0.1$ MeV, with a overall dose of 1.5×10^{23} n $\cdot$ cm^{-2}. By comparison to the control sample, seen on the left, it has swollen considerably [16, 17].

1.1 Important Terminology

Atomic Percentage (at.%) This notation is used to describe the composition of a material in terms of the relative abundance of atomic species, as opposed to specifying the concentrations by mass (wt.%). Since we study binary alloys in this work, we can quote an iron-chromium concentration unambiguously with one number, e.g. $\mathrm{FeCr}_{10\ \mathrm{at.\%}}$, which refers to a material whose bulk contains nine iron atoms for every chromium atom.

Mixing Enthalpy The thermodynamical term used to describe the system energy change

when two or more substances are mixed without a chemical reaction occurring. Endothermic processes are indicated by positive mixing enthalpies, while negative mixing enthalpies are given when the process is exothermic [18]. The alloying of BCC iron and chromium has the unusual property of negative mixing enthalpy for low chromium concentrations, and as a consequence, the largest ideal lattice parameter (see section 1.1.1) that can be achieved by an iron-chromium mixture is greater than the ideal lattice parameters of either metal individually [19–21].

Primary Knock-on Atom (PKA) An atom that, through interaction with an incident particle (a neutron or alpha particle, for example), receives a large amount of kinetic energy, the dissipation of which to its surroundings results in a collision cascade. To give the reader a sense of scale, an iron or chromium atom with a kinetic energy of 1 keV is travelling at approximately 60 km/s.

Collision Cascade An event wherein a PKA introduces damage to an atomic lattice by the displacement of its neighbours.

Displacements per Atom (DPA) A generalised unit used in radiation materials science to describe an object's accumulated radiation induced damage in terms of the average number of times each atom in the system has been displaced from a lattice site.

Cascade Splitting When a high energy PKA will transfer large amounts of momentum to a small number of secondary knock-on atoms, which propagate in diverging directions, and effectively cause their own cascade events in other parts of the system.

Ballistic Phase The period of the simulation during which there are atoms with sufficient kinetic energy to move easily between lattice sites.

Recovery Phase The period after the equipartition of the kinetic energy introduced by the PKA occurs when the time spent by the system in a given state becomes large relative to the ballistic phase, and its dynamics are best described by transition state theory.

Equipartition of Energy The phenomenon where additional kinetic energy introduced to the lattice system tends towards being evenly distributed between thermal and potential energy, given sufficient time.

Vacancy A lattice site where an atom is absent.

Interstitial An atom which does not have its own lattice site.

Lone Interstitial Atom An atom which is not situated on a lattice site (LIA).

Split-Interstitial/Dumbbell A Split-Interstitial (SI) is a pair of atoms occupying the same lattice site, that is, lying either side of it. Colloquially, these also known as dumbbells, a moniker which stems from their appearance on many diagrams, such as in figure 1.3. The orientation of a split-interstitial relative to the lattice structure is specified using Millier indices.

Split-Vacancy A defect configuration where an interstitial atom resides between two vacant lattice sites.

Defect Atom An atom which is part of a lattice defect object. For example, if one has a lattice with three lone interstitials and five split-interstitials, there are a total of thirteen defect atoms.

Frenkel Pair When an ideal lattice is disrupted, and an atom is removed from a lattice site, both a vacancy and an interstitial atom are created. Together, they are referred to as a Frenkel pair.

Recombination When a Frenkel pair is annihilated by an interstitial atom moving into a vacant lattice site.

Replacement Collision Sequence Often occurring during collision cascades, this is a temporary displacement of atoms from the lattice along a straight line, normally leav-

ing the atom at the end of the chain as an interstitial, while the others relax back onto their original sites.

Defect Formation Energy An ideal lattice is the lowest energy state for a system of atoms. If a defect is introduced, this implies that the energy of the system has increased. To calculate the formation energy, E_{f}, of some defect, we use the following equation:

$$E_{\mathrm{f}} = E_{\mathrm{total}}^{\mathrm{def}} - \sum_{m} \left(\frac{N_m^{\mathrm{def}}}{N_m^{\mathrm{bulk}}} E_m^{\mathrm{bulk}} \right) \tag{1.1}$$

where $E_{\mathrm{total}}^{\mathrm{def}}$ is the total system energy with a defect, and the sum over m represents all the atomic species present in the system. E_m^{bulk} is the energy of all the atoms of element m in a system without defects, N_m^{bulk} is the number of atoms of element m in a defectless system, and N_m^{def} is the number of atoms of element m in the defect system [22].

In figure 1.3, four varieties of defect are shown.

1.1.1 The Body Centred Cubic Lattice Structure

At the mesoscopic scale, metals take the form of crystals, whose atoms may be described as being arranged in a Bravais lattice, formed by a repeating pattern of identical unit cells, and surrounded by a free electron gas [23]. The iron-chromium binary alloys studied in this work have a Body Centred Cubic (BCC) structure. The atoms of the BCC structure are arranged into repeating cubes, each with an additional single atom placed at its centre, as shown in figure 1.4. The distance over which the pattern repeats itself is called the lattice parameter, and is denoted a_0. In the BCC structure, this distance is also the second nearest neighbour distance. The first nearest neighbour distance is the separation between one of the cube's vertex atoms, and the central atom. The distances to, and number of, neighbours up to the fifth nearest neighbour are shown in table 1.1.

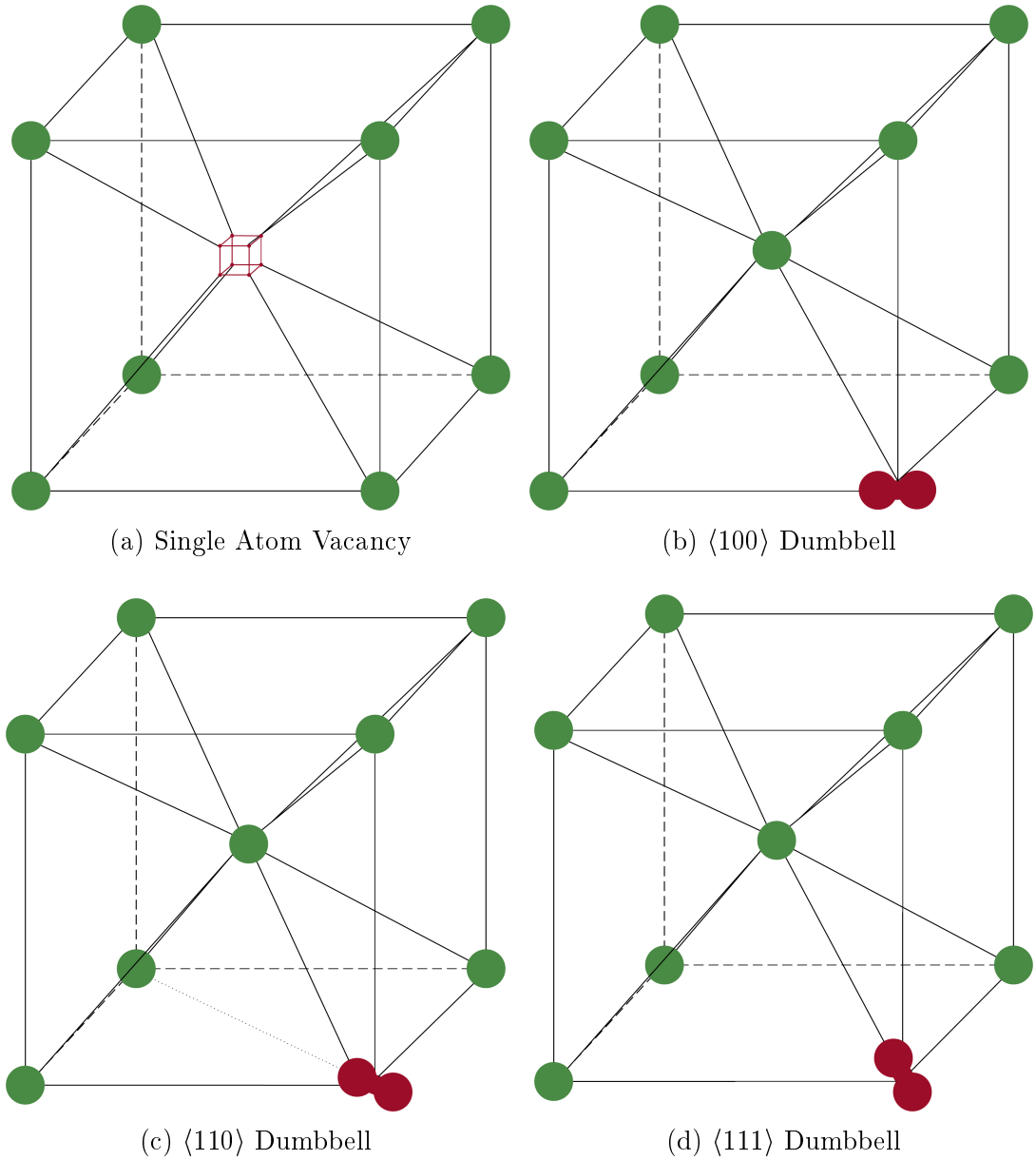

(a) Single Atom Vacancy

(b) ⟨100⟩ Dumbbell

(c) ⟨110⟩ Dumbbell

(d) ⟨111⟩ Dumbbell

Figure 1.3: Illustration of four types of defect in a BCC lattice. Miller indices are used to indicate orientation relative to the lattice structure.

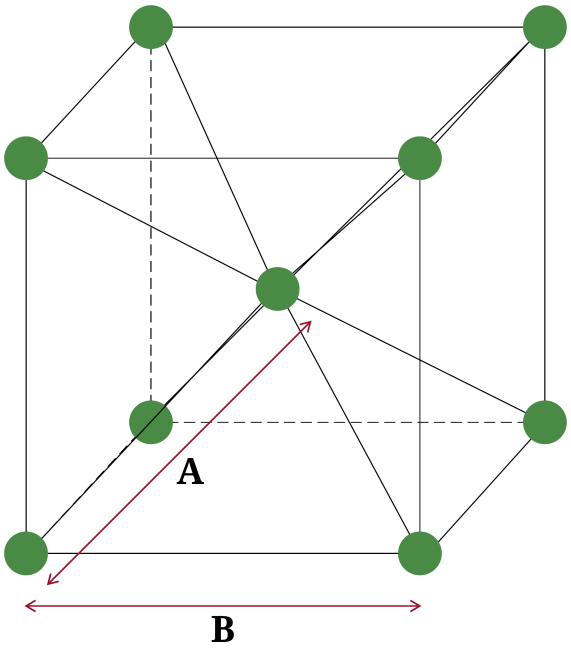

Figure 1.4: The Body Centred Cubic lattice structure, with first and second nearest neighbour distances labelled as **A** and **B** respectively.

Table 1.1: The distances to, and number of, neighbours up to the fifth nearest neighbour in the Body Centred Cubic lattice structure.

N^{th} Nearest Neighbour	Separation/a_0	Number of N^{th} Nearest Neighbours
1^{st}	$\sqrt{3}/2$	8
2^{nd}	1	6
3^{rd}	$\sqrt{2}$	12
4^{th}	$\sqrt{11}/2$	12
5^{th}	$\sqrt{3}$	8

1.1.2 PKA Vectors

The spacial direction of travel of a PKA is called the PKA vector, and is defined relative to the surrounding crystal structure. PKA vectors are specified using Millier indices, in the form $\langle a\ b\ c \rangle$, such that this specifies any point on the unit sphere that can be specified via a permutation of the given a, b, and c values.

1.2 Literature Context & Research Aims

To put this project into context amongst the existing literature, in this section we discuss prior works, which are divided into those that discuss the empirical physical properties of relevant steels and the experimental work performed, and those utilising computational methodologies in the simulation of irradiated materials.

1.2.1 Experimental Work & the Properties of Steel

It is apparent from empirical evidence, that Ferritic/Marsenetic (F/M) steels demonstrate more suitable behaviour than Austenitic steels[2] for nuclear reactor construction purposes, exhibiting lesser thermal expansion, as well as less swelling or segregation when subject to radiation [10, 24], suffering little nuclear activation [25]. Furthermore, incorporating even modest amounts of chromium into the steel benefits its radiation damage resistance [24, 26, 27], as well as introducing the oxidation resistance quality [28], from which the moniker, "stainless steel" is derived. Nevertheless, F/M steels are not immune to degradation; even without the effects of radiation, chromium is observed separating from the iron bulk at grain boundaries when heated [10]. Radiation is found to promote segregation in metals, particularly at temperatures approximate to one third of their melting point[3] [30]; With the segregation of materials comes the formation of chromium depleted regions, vulnerable to corrosion by oxidation, as observed by Brodyanski *et al.* 2011 [31].

Bhattacharya *et al.* 2014 [28] studied bombardment of iron-chromium binary alloys with chromium content between 5.8 and 15.1 at.%, using 2 MeV Fe^{2+} and 2 MeV He^{+} ions; they found the chromium segregation induced was inversely proportional to the bulk chromium content. They performed their experimentation at 773 Kelvin, but by annealing their samples post-irradiation at 900 Kelvin, the apparent damage to the lattice structure healed, without the restoration of chromium distribution. The work of Was *et al.* 2011 [32] indicates that the

[2] A phase of steel with a Face Centred Cubic (FCC) structure
[3] Steels typically have melting points in the region of 1700 to 1800 Kelvin [29]

formation of chromium enriched regions is more likely in alloys of low bulk concentration, while Hu *et al.* 2013 [10] found evidence that the presence of Carbon in their samples inhibited the segregation of chromium. Little and Stow 1979 [26] and Garner *et al.* 2000 [24] showed that by comparison to pure iron, the addition of chromium reduces radiation induced swelling. The optimal range for chromium concentration appears to be in the range 9 and 12 wt.% [8, 26], with concentrations between 2 and 6 wt.% yielding inferior performance by comparison [33–35]. Suganuma and Kayano 1983 [36] recorded another notable difference between iron and iron-chromium alloys, insofar as the latter must be annealed at a higher temperature following irradiation to see the recovery of the lattice structure, with Arakawa *et al.* 2004 [37] finding that the presence of chromium atoms suppresses the mobility of interstitial atom structures.

1.2.2 Computational Studies

When studying radiation damage effects, the simulation of collision cascades using MD (see Chapter 2) is frequently the starting point for computational studies. Given the experimental evidence collected regarding the optimal range for the bulk concentration of chromium in F/M steels, the focus of the literature has been on binary alloys between 0 to 15 at.% chromium [38–46]. Within this range, the number of Frenkel pairs at the end of the ballistic phase seems to be largely unaffected by the chromium concentration, meaning that the radiation damage resistance observed on macroscopic scales must emerge over longer timescales than those used in MD [44], although in high energy cascades, chromium is demonstrated to promote cascade splitting [39, 42, 44]. Furthermore, chromium appears to form more stable interstitial defects by comparison to iron, appearing in defect atoms at a higher rate than would be commensurate with the bulk concentration[4] [39, 42, 44, 47], and the presence of chromium atoms appears to reduce overall defect mobility [7, 44]. The grain size of F/M steel is very large compared to the scale over which cascade damage is produced [26], so

[4] Malerba *et al.* 2013 [44] reports that this effect is negatively correlated with bulk chromium concentration.

by restraining and containing the migration of defects, the migration of defects towards each other is promoted over the migration towards grain boundaries, thus favouring the recombination of Frenkel pairs [44]. Olsson 2009 [48] predicts that regions of relative high concentration of chromium will inhibit the formation of interstitial clusters, however, the findings of Terentyev *et al.* 2011 [43] show that the number of defects that are found in clustered formations after a collision cascade is positively correlated with bulk chromium concentration. Terentyev *et al.* 2011's [43] also find that the insertion of dislocation loops into lattices prior to the simulation of a collision cascade, results in the creation of less lattice damage.

The simulation in the literature infrequently include trace elements, although these must inevitably exist in real alloys to some degree, even in high purity binary alloys. Nevertheless, Malerba *et al.* 2013 [44] report that trace elements, such as Carbon, are not observed to effect the cascade evolution, and the computational literature is consistent with experimentation in its prediction of the optimal chromium concentration for radiation damage resistance [47]. As with physical reality, the segregation of alloy elements occurs more readily at higher temperatures [47].

1.2.3 This Project

While a considerable contribution to issues surrounding radiation damage effects maybe found in the literature, there are a number of points we believe we may address. Firstly, many of the computational works that simulate collision cascades using MD, do so with minimal application of computing resources, drawing their statistics from tens of simulations [43, 49, 50]. With the HPC facilities available to us, see section 1.3.2, we will be drawing our statistics from thousands of data points for high confidence results. Additionally, many papers attempt to save computing power through the use of "representative vectors", see section 1.1.2, for the orientation of their PKAs [39, 43, 47, 51, 52], which allows them to draw statistics from a smaller data set. With the computing power available to us, we will

be able to create statistical samples of cascade simulations, wherein the PKA vectors used evenly sample the unit sphere – in section 4.4, we explore the validity of this computational labour saving method. Many of the works described in section 1.2.2 focus on high energy cascades [43, 44, 47], but this may give misleading results. When considering the motion of very energetic atoms, the normal interatomic potentials used become inadequate, given that they do not give separate consideration to electronic stopping [53]. Furthermore, given the tendency of a high energy cascade to split into sub-cascades, one may simulate these smaller events, thinking of them as having been initiated by a larger parent cascade sequence. Indeed, in section 5.2.1.3, it is seen how much more common small events can be with respect to the very energetic events.

Molecular dynamics is a very commonly employed technique in the field of radiation materials science, but less work involving AKMC has been conducted, and comparatively little work has explored collision cascades in lattices having already sustained damage from one or more previous cascade events. With AKMC able to explore the recovery of a system after damage introducing events, we hope to explore the aftermath of collision cascades, and achieve timescales appropriate for the simulation of multiple events.

1.3 Computational Resources

1.3.1 Software

1.3.1.1 LBOMD

Lough**bo**rough **M**olecular **D**ynamics (LBOMD) is our in-house implementation of the Molecular Dynamics technique, which is covered in detail in chapter 2. Presently, the software's features include the simulation of collision cascades, thin-film deposition, nano-indentation, thermalisation, and damped-MD relaxation.

1.3.1.2 LAKMC

Loughborough **A**daptive **K**inetic **M**onte-**C**arlo is our in house implementation of the Adaptive Kinetic Monte Carlo method, as described in chapter 3. The software requires an ancillary package for its interatomic force calculations and presently, supported software includes LBOMD and LAMMPS [54]. Additionally, LAKMC includes the ability to incorporate MD simulations, e.g. of collision cascades, as events in its roulette tables, for which it leverages an MD package. LAKMC requires the explicit identification of defect objects, and for this task, Atoman is employed, see section 1.3.1.3.

1.3.1.3 Atoman

Atoman, developed and maintained by C.D.J. Scott, and freely available on-line [55], is used for the identification and visualisation of defect in the lattices resulting from our atomistic simulations, supporting files produced by LBOMD and LAKMC, as well as third-party packages such as LAMMPS [54]; the images produced that depict our simulated lattices are created using this software. A brief description of some of the methods available to Atoman may be found in section 2.4.

1.3.1.4 SRIM

The **S**topping & **R**ange of **I**ons in **M**atter (SRIM) is a third-party software package [56, 57] that we use in chapter 5 to generate data regarding the collision cascade event frequency and distribution of PKA energies for a sample exposed to a given radiation environment. A description of its modelling methods is given in section 5.2.1.

1.3.2 Hardware

For the computationally expensive tasks and large number of simulations performed during our research, we were granted access to the "Hydra" High Performance System at Loughborough University. The Hydra supercomputer has 176 nodes available for general computing,

of which 122 provide twelve processing cores and 34 provide twenty processing cores, with an additional five nodes equipped with GPUs. Over the course of this project[5], we expended approximately three million core-hours.

1.4 Thesis Layout

Chapter 1: Introduction and Background

In this chapter, we introduce the motivation for our project, its context in the literature, and some useful background information.

Chapter 2: Methodology 1: Molecular Dynamics & Semi-Empirical Potentials

Here, the methodology behind Molecular Dynamics is presented, along with the inter-atomic potential that is used to calculate the potential energy and forces that act on atoms, are presented. A background regarding the analysis of lattice defects is also given.

Chapter 3: Methodology 2: Adaptive Kinetic Monte Carlo & the Superbasin Method

The operation of our long timescale dynamics modelling by way of the Adaptive Kinetic Monte Carlo algorithm and the Super-Basin method are lain out in this chapter.

Chapter 4: Collision Cascades and Displacement Threshold Energy

In the first of our results chapters, we discuss statistics produced by many simulations of single collision cascade events in a variety of contexts, and our examination of the concept of displacement threshold energy.

Chapter 5: Modelling Experimental Work

In the second of our results chapters, we attempt to create a multiple cascade event model, based on an experimental procedure.

[5]During Hydra's refurbishment, we also made use of HPC Midlands' "Hera" system.

Chapter 6: Conclusions

In our final main chapter, we summarise this work and give recommendations for future endeavours.

Chapter 7: References

A list of academic publications and other references cited in this work.

Chapter 8: Appendix

In the appendix, one may find supplementary information, not part of the main body of this thesis.

Chapter 2

Methodology 1: Molecular Dynamics & Semi-Empirical Potentials

2.1 Operation of Molecular Dynamics

Molecular Dynamics is a deterministic method for atomistic simulations. A continuous potential is defined as a function of the relative positions of the system's atoms and their subsequent trajectory is produced by the numerical integration of Newton's laws of motion.

2.1.1 Velocity Verlet Algorithm

In this work, the integration of Newton's laws of motion in the MD simulations are implemented via the *Verlet Velocity Algorithm* [58]. First, consider an atom with the vector position, velocity, and acceleration, $\vec{r}$, $\vec{v}$, $\vec{a}$, respectively. For a potential energy function, $U(\vec{r})$, the force acting on the atom, $\vec{F}$, is:

$$\vec{F} = -\nabla U(\vec{r}) \tag{2.1}$$

Recalling Newton's second law in the form of $\vec{F} = m\vec{a}$ implies:

$$\vec{a} = -\frac{\nabla U\left(\vec{r}\right)}{m} \tag{2.2}$$

For the first timestep of the algorithm, the position and velocity are advanced by the truncated Taylor expansions found in equations (2.3) and (2.4):

$$\vec{r}(t + \Delta t) = \vec{r} + t\Delta t + \frac{\vec{a}(t)\Delta t^2}{2} \tag{2.3}$$

$$\vec{v}(t + \Delta t) = \vec{v}(t) + \frac{\vec{a}(t) + \vec{a}(t + \Delta t)}{2}\Delta t \tag{2.4}$$

where t is used for time and Δt as the size of the timestep, with accelerations found from equation (2.2). Subsequent timesteps evolve the system as follows:

1. Calculate the velocity after one half timestep, $\vec{v}\left(t + \frac{\Delta t}{2}\right)$, using the velocity and acceleration at the current time and position.

$$\vec{v}\left(t + \frac{\Delta t}{2}\right) = \vec{v}(t) + \frac{\vec{a}(t)\Delta t}{2} \tag{2.5}$$

2. Using this result, calculate the next timestep's position.

$$\vec{r}(t + \Delta t) = \vec{r}(t) + \vec{v}\left(t + \frac{\Delta t}{2}\right)\Delta t \tag{2.6}$$

3. From the new position, $\vec{r}(t + \Delta t)$, find the new acceleration, $\vec{a}(t + \Delta t)$, using equation (2.2).

4. Finally, the new velocity, $\vec{v}(t + \Delta t)$, is given by:

$$\vec{v}(t + \Delta t) = \vec{v}\left(t + \frac{\Delta t}{2}\right) + \frac{\vec{a}(t + \Delta t)\Delta t^2}{2} \tag{2.7}$$

5. One may now advance the time from t to $t + \Delta t$ and return to step 1.

2.1.2 Boundary Conditions

Being only able to simulate a finite number of atoms, we must give consideration to the boundary conditions of our cell. It is possible, although far from ideal, to fix the atoms at the boundaries, but this could distort the dynamics of the system when energetic atoms or pressure waves approach the edge. The scale of our atomistic models is far below the macroscopic, which means that an atom deep in the bulk of a material can be considered physically as if it is in an infinitely large system. To simulate an infinite bulk with a finite number of atoms, periodic boundary conditions are used. This is to say that as an atom moves off the edge of the system in one direction, it is transferred to the opposite face, retaining its coordinates in the other dimensions. This is illustrated in Figure 2.1. Likewise, interatomic forces are transferred across the boundary – two atoms with the same x and y coordinates, each 0.5 Å from the opposite extrema of the z axis will exert an identical force upon each other as two atoms separated by 1 Å in the centre of the lattice. The technique gives the illusion of an infinite space, provided that the mean free path of particles does not exceed the simulation width/height/depth. It is not acceptable for a cascade event to overlap with itself; if this becomes a danger, the simulation volume must be increased [40, 42].

2.1.3 Thermal Layers

To improve the impression of a bulk beyond the simulation cell, we can apply a thermostat to the atoms in the outermost layers, which simulates the dissipation of thermal energy to the larger system. Thermostats alter the equation of motion of these atoms, adjusting their kinetic energy to bring the system temperature closer to a desired value. Examples of thermostats include the Nosé-Hoover thermostat and the Berendsen thermostat [59–62].

The Nosé-Hoover thermostat introduces a friction coefficient of varied strength to give the desired temperature. It maintains a canonical ensemble, but has the disadvantage that

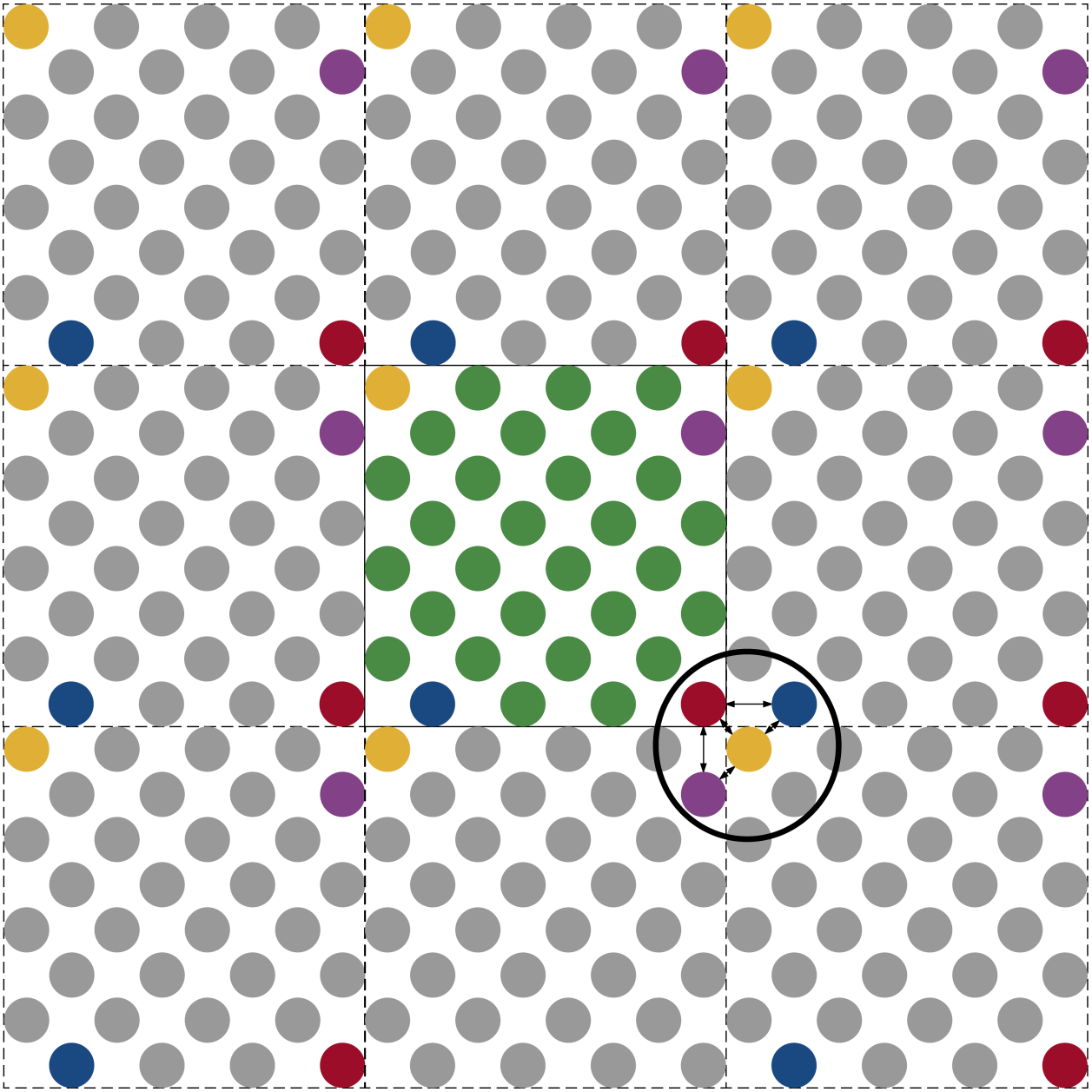

Figure 2.1: In this illustration we depict periodic boundary conditions in a two-dimensional example. An exact copy of the atomic lattice is placed on all edges of the system, fully enveloping it, and an atom that crosses the boundaries onto the next copy appears in the equivalent position in all cells. Forces transmit across the boundary such that an atom interacts with its neighbours identically, regardless of whether a boundary is crossed. In the circled example, four atoms are highlighted in red, blue, yellow and purple, and these atoms are neighbours across the periodic boundaries, with these interactions marked by double headed arrows. To illustrate how the method is applied, they retain their colouring in the original cell (green atoms), and in the copies (grey atoms).

it is prone to large temperature oscillations, limiting how quickly it can achieve the desired temperature [60–62].

The Berendsen thermostat simulates the presence of a weakly coupled heat bath. It scales its atomic velocity alterations such that the rate at which it changes the system temperature is proportional to the difference between the desired and actual temperatures. In contrast to the Nosé-Hoover thermostat, it can only approximately maintain a canonical ensemble and is not time reversible. On the other hand, the Berendsen thermostat reaches its target temperature comparatively rapidly, and its relative simplicity makes it desirable to use. As such, the Berendsen thermostat is chosen when thermal layers are used in our Molecular Dynamics work [59–62].

For the purposes of this thermostat, the current temperature of a set of N atoms is defined by T, such that:

$$T = \frac{2}{3Nk_B} \sum E_k \tag{2.8}$$

where k_B is Boltzmann constant and $\sum E_k$ is the atoms' total kinetic energy. For a timestep of Δt, and target temperature of T_0, the velocity of the atoms to which the thermostat is applied is scaled by a factor of, λ:

$$\lambda = \sqrt{1 + \frac{\Delta t}{\tau}\left(\frac{T}{T_0} - 1\right)} \tag{2.9}$$

where τ parameterises the coupling factor, such that the rate of change in temperature is,

$$\frac{\mathrm{d}T}{\mathrm{d}t} = \frac{T_0 - T}{\tau} \tag{2.10}$$

2.2 Interatomic Potentials

To simulate the behaviour of our system, an interatomic potential must be selected to describe the energy of each of the atoms, and thus the potential energy hypersurface. If

the energy of an individual atom, i, is given by U_i, the force experienced by that atom is $-\nabla U_i$, where ∇ is the differential operator. We use a style of potential known by the name, "*Embedded Atom Method*", whose origins lie with the work Dawes and Bakes in the 1980s [63,64]. EAM potentials are semi-empirical, being a combination of *Density Functional Theory* (DFT) calculations and experimental data. The general form of an embedded atom method potential (henceforth *EAM potential*) is given by equation (2.11).

$$U_i = \frac{1}{2}\left(\sum_{j\neq i} V_{ij}(r_{ij})\right) + \sum_b F_{ib}\left(\sum_{j\neq i}\phi_{jb}(r_{ij})\right) \tag{2.11}$$

While EAM potentials do use a pairwise interaction that operates directly between any two atoms in range of each other (given by the V_{ij} term), the core concept underpinning EAM is that when the potential energy of an atom is calculated, it is treated as an impurity embedded in the bulk. This is to say that the embedding functions (the F_{ib} terms) represent the energy required to implant the atom at its position in the system, considering the aggregate effect of the electrons in the region. One may include terms for as many electron bands as required, as marked by the sum over b, although in many cases, only one (the d-band) is used.

In all our potential energy calculations, we operate in units of electron volts (eV) and Ångströms (Å); our unit of force is thus eV/Å.

2.2.1 Heaviside Step Function

While the electrostatic forces which govern interatomic interactions are, in reality, infinite in range, due to the practical limitations that stem from the finite computing power available, the potentials used for atomistic modelling are limited to a cut off radius; this is acceptable because the forces exerted on an atom become diminishingly small with increasing range compared to its more immediate neighbours. The Heaviside step function is frequently used in formulating potentials with cut offs, and thus it is defined in equation (2.12).

$$H(r) = \begin{cases} 0 & \text{for} \quad r < 0 \\ 1 & \text{for} \quad r \geq 0 \end{cases} \tag{2.12}$$

2.2.2 Selecting the Potential

2.2.2.1 Issues with Olsson 2005 and Bonny 2011 source papers

Originally, it was intended that an iron-chromium EAM potential developed by Olsson *et al.* in 2005 would be used in this work, one which was an extension of the pure iron potential developed in 2004 by Ackland *et al.* [65, 66]. It transpired, however, the description of the potential given in the 2005 paper contained a number of errors, and while an erratum has been published, it is not exhaustive. With correspondence with Pär Olsson, functionality for pure iron and chromium was achieved, but we were unable to discover all necessary corrections to reproduce the mix-species interaction. Eventually, it was deemed not to be time-cost effective to continue and we discarded Olsson's potential in favour of similar work developed in 2011 by Bonny *et al.*, which takes its pure iron interaction from a 2003 paper by Mendelev *et al.* [67, 68]. The specification for this potential was published in an open report by SCK-CEN[1], but this document also contained a number of disparities between the potential as described and the authors' actual work[2]. In this case, our correspondence with Giovanni Bonny proved fruitful, and a fully functional implementation of the potential was created. A catalogue of the known errors in the papers describing the potentials may be found in the appendix of this document. Bonny *et al.*'s potential is designed to include the best features of two other potentials: the Olsson Potential from 2005, and another developed by Caro *et al.* in the same year [70]. Both Olsson *et al.* and Bonny *et al.*'s potentials use a two band model to capture the negative mixing enthalpy of iron-chromium systems with low concentration of chromium (see section 1.1).

[1] The Belgian Nuclear Materials Science Institute

[2] It should be remarked that this potential was also published in *Taylor & Francis Philosophical Magazine* [69]. The SCK-CEN report [67] is more detailed, and includes many more defect energies and other material specifics, which allows for more thorough implementation verification – This is why it was used as our main source. Both the paper and the report contain many of the same errors.

2.2.2.2 Potential Benchmarking

In recent benchmarking work conducted by Klaver *et al.*, it was concluded that insufficient attention was given to chromium-chromium interactions in two-band EAM potentials such as Olsson 2005 and Bonny 2011, and that defect formation energy for high chromium percentage materials were not physcially appropriate. Thankfully for this project, Klaver *et al.* conclude that Bonny *et al.*'s potential was the less flawed of the two, and since we do not simulate chromium concentrations above 10 at.% in this work, their findings do not present a major problem [71, 72].

2.2.3 Bonny 2011 EAM Two-Band Potential

Every atom in the system has an energy contribution comprised of a pairwise interaction and embedding terms. The pairwise term is a sum over $V_{ij}(r_{ij})$ terms, where atom i interacts separately with each of its neighbours, i.e. the j terms, with r_{ij} being the scalar separation between atoms i and j. The form of $V_{ij}(r_{ij})$ is dependent on the species pairing of i and j, with differing forms for Fe-Fe, Cr-Cr, and Fe-Cr. The embedding terms take a more complex form. First, the electron density around each atom must be found for each electron band considered. This is done by summing over functions representing the electrons of its neighbours, the form of which is dependent on the band and importantly, the neighbour's species only. Here on, we refer to the density sum for some band, b, and atom, i, by ρ_{ib}, such that:

$$\rho_{ib} = \sum_{j \neq i} \phi_{jb}(r_{ij}) \tag{2.13}$$

This density term is then used by an embedding function to give the embedding energy. This function's form is dependent on the band type and the i atom's species. Note that same species interactions only provide a d-band density contribution, whereas atoms of differing species will contribute to both of each others s and d-bands.

2.2.3.1 Pure Iron

The Bonny Potential takes its pure iron interaction from a 2003 work by Mendelev *et al.* [68]. A cubic spline is used for both the Fe-Fe pairwise interaction, and the d-band density contribution from an iron atom; these are equations (2.14) and (2.15).

$$V_{ij}(r_{ij}) = \sum_{\alpha=1}^{13} a_\alpha (r_\alpha - r_{ij})^3 H(r_\alpha - r_{ij}) \tag{2.14}$$

$$\phi_{ijd}(r_{ij}) = \sum_{\beta=1}^{3} b_\beta (r_\beta - r_{ij})^3 H(r_\beta - r_{ij}) \tag{2.15}$$

The a_α and b_β parametrise the interaction strengths, while r_α and r_β set the position of the Heaviside cut-offs. Their values are given in table 2.1. iron's d-band embedding function is given by:

$$F_{id}(\rho_{id}) = A_{[d\ 1]}\sqrt{\rho_{id}} + A_{[d\ 2]}\rho_{id}^2 \tag{2.16}$$

With $A_{[d\ 1]}$ and $A_{[d\ 2]}$ parametrising the function's strength, equalling -1 eV and $-3.5387096579929\times10^{-4}$ eV respectively.

2.2.3.2 Pure Chromium

The pairwise function for interactions between chromium atoms takes much the same form as its iron counterpart,

$$V_{ij}(r_{ij}) = \sum_{\alpha=1}^{5} a_\alpha (r_\alpha - r_{ij})^3 H(r_\alpha - r_{ij}) \tag{2.17}$$

with the relevant parameters given in table 2.2; however the d-band density contribution from a chromium atom is defined as:

$$\phi_{ijd}(r_{ij}) = \frac{1}{\phi_0}\left[\frac{r_0}{r_{ij}}\exp\left(-\beta\frac{r_{ij}}{r_0}\right) - \frac{\exp\left(-\beta x_{\text{cut}}\right)}{x_{\text{cut}}}\right] f_{\text{cut}}\left(\frac{r_{ij}}{r_0}, x_{\text{cut}}\right) \tag{2.18}$$

Indice	Coefficient	Cut-Off
α	a_α / $\left(\text{eV Å}^{-3}\right)$	r_α / (Å)
1	-24.028204854115	2.2
2	11.300691696477	2.3
3	5.3144495820462	2.4
4	-4.6659532856049	2.5
5	5.9637758529194	2.6
6	-1.7710262006061	2.7
7	0.85913830768731	2.8
8	-2.1845362968261	3.0
9	2.6424377007466	3.3
10	-1.0358345370208	3.7
11	0.33548264951582	4.2
12	-0.046448582149334	4.7
13	-0.0070294963048689	5.3
β	b_β / $\left(\text{Å}^{-3}\right)$	r_β / (Å)
1	11.686859407970	2.4
2	-0.01471074009883	3.2
3	0.47193527075943	4.2

Table 2.1: Parameters used for pure iron in the Bonny 2011 EAM Potential [68], see equations (2.14) and (2.15).

where r_0 is the first nearest neighbour distance in a BCC crystal with a lattice parameter of 2.878 Å (i.e. $r_0 = 2.878 \times \frac{\sqrt{3}}{2}$ Å ≈ 2.492 Å), and $x_{\text{cut}} = 1.65$, being a cut-off parameter[3]. There are two normalisation factors, these being $\phi_0 = 0.0676504617$ and $\beta = 5$. $f_{\text{cut}}\left(\frac{r_{ij}}{r_0}, x_{\text{cut}}\right)$ is a cut-off function, which brings the density contribution down to zero between $r_{ij} \approx 0.4012$ Å and $r_{ij} \approx 4.112$ Å. It takes the form:

$$f_{\text{cut}}\left(x, x_{\text{cut}}\right) = \begin{cases} 1 & \text{for} \quad x \leq 1 \\ 1 - \frac{(x-1)^3}{(x_{\text{cut}}-1)^3} & \text{for} \quad 1 < x \leq x_{\text{cut}} \\ 0 & \text{for} \quad x_{\text{cut}} < x \end{cases} \tag{2.19}$$

[3]Note that x_{cut} marks a specific ratio between r_{ij} and r_0, not an actual length itself, and is thus unitless.

Bonny *et al.* report that their d-band embedding function is too complicated to express as an equation in the paper. They were, however, kind enough to provide the embedding function in a tabulated form (see figure 2.2), which is what we use in this work.

Indice	Coefficient	Cut-Off
α	a_α / $\left(\text{eV Å}^{-3}\right)$	r_α / (Å)
1	7.942650649×10^{-1}	2.617042168
2	-1.275324968	2.990905335
3	2.424000178	3.364768501
4	$-8.216224618\times10^{-1}$	3.738631668
5	$-6.079639840\times10^{-2}$	4.112494835

Table 2.2: Parameters used for pure chromium in the Bonny 2011 EAM Potential [67], see equation (2.17).

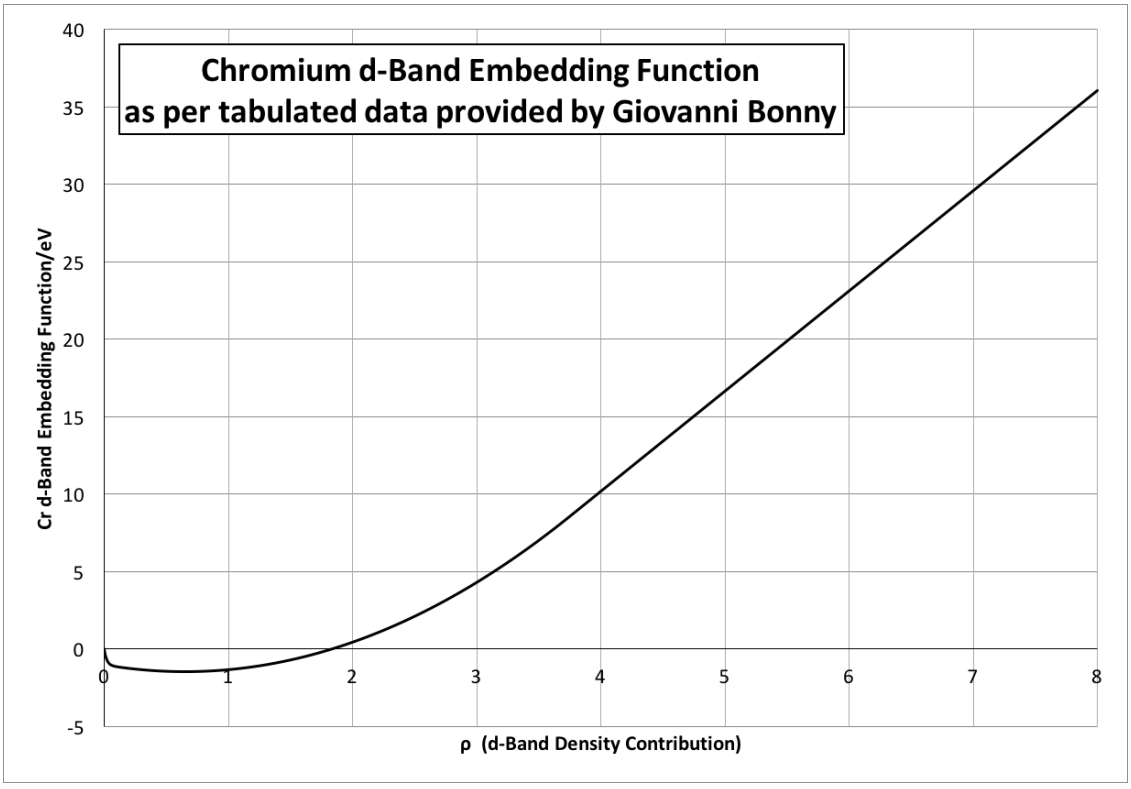

Figure 2.2: Graph depicting the d-band embedding function for chromium, provided in tabulated form by Giovanni Bonny, for the domain $0 \leq \rho \leq 8$.

2.2.3.3 Mixed Species Interaction

For the pairwise interaction between atoms of differing species, we again have a cubic/Heaviside based function,

$$V_{ij}(r_{ij}) = \sum_{\alpha=1}^{9} a_\alpha (r_\alpha - r_{ij})^3 H(r_\alpha - r_{ij}) \tag{2.20}$$

with the parameters for the mixed case given in table 2.3.

It is necessary to include an s-band electron density term in a system involving both iron and chromium. This is due to an unusual property of this element combination, i.e. a negative mixing enthalpy for some relative concentrations [67]. The s-band density contributions from a chromium atom for an iron atom, and from an iron atom for a chromium atom are the same, and given by:

$$\phi_s(r_{ij}) = \frac{\left(N_s r_{ij}^3 \exp\left[-\frac{\zeta_s r_{ij}}{r_b}\right]\right)^2}{Z} g_{\text{cut}}\left(r_{ij}\right) \tag{2.21}$$

where $N_s = 5$, $\zeta_s = 1.323$, $Z = 0.245811927$ and R_b is the Bohr Radius, 0.529177210818181818 Å, with g_{cut} being a cut-off function, taking the density contribution to zero between $r_{ij} = 5.1$ Å and $r_{ij} = 5.3$ Å by way of:

$$g_{\text{cut}}\left(r_{ij}\right) = \begin{cases} 1 & \text{for} \quad r_{ij} \leq r_i \\ \frac{1}{2}\left[1 - \sin\left(\frac{\pi(r_{ij} - r_m)}{2d}\right)\right] & \text{for} \quad r_i < r_{ij} \leq r_f \\ 0 & \text{for} \quad r_f < r_{ij} \end{cases} \tag{2.22}$$

r_m and d are given by:

$$r_m = \frac{(r_f + r_i)}{2} \qquad \text{and} \qquad d = \frac{(r_f - r_i)}{2} \tag{2.23}$$

With $r_i = 5.1$ Å and $r_f = 5.3$ Å.

By contrast, while the form of the s-band embedding function is the same for both iron

and chromium (see equation (2.24)), its parameters vary by species.

$$F_{is}(\rho_{is}) = A_{[s\ 1]}\sqrt{\rho_{is}} + A_{[s\ 2]}\rho_{is}^2 \tag{2.24}$$

For iron atoms, the coefficients take the values

$$A_{[s\ 1]} = -0.217009784 \text{ eV} \qquad \text{and} \qquad A_{[s\ 2]} = 0.388002579 \text{ eV} \tag{2.25}$$

and for chromium atoms these are

$$A_{[s\ 1]} = -0.977557632 \times 10^{-2} \text{ eV} \qquad \text{and} \qquad A_{[s\ 2]} = 0.374570104 \text{ eV} \tag{2.26}$$

Indice	Coefficient	Cut-Off
α	a_α / $\left(\text{eV Å}^{-3}\right)$	r_α / (Å)
1	100.0	2.15
2	-5.57581564	2.2
3	-16.22	2.33
4	2.55634481	2.58333333
5	0.0683226765	2.96666667
6	0.414828704	3.35
7	0.0322279809	3.73333333
8	-0.01081841	4.11666667
9	-0.0748992889	4.5

Table 2.3: Parameters used for the mixed pairwise term in the Bonny 2011 EAM Potential [67], see equation (2.20).

2.2.3.4 Short Range Interactions

The modelling assumptions of EAM break down for atoms very close to each other, and so at short range, we use the universal potential of Ziegler, Biersack and Littmark (henceforth the *ZBL potential*). It replaces the default pairwise terms in the EAM equation, that is equation

(2.11), since as separation tends to zero, the pairwise interaction becomes massively dominant in relation to the embedding terms. For two atoms, i and j, with atomic numbers, Z_i and Z_j, the ZBL potential is given by [56]:

$$V_{\mathrm{ZBL}}(r_{ij}) = \frac{Z_i Z_j e^2}{r_{ij}} \varphi\left(\frac{r_{ij}}{a_s}\right) \tag{2.27}$$

where a_s is the screening parameter, such that

$$a_s = \frac{0.88534 a_b}{Z_i^{0.23} + Z_j^{0.23}} \tag{2.28}$$

with $a_b = 0.529$ Å being the Bohr Radius and $e^2 = 14.400$ eVÅ, where e is the elementary charge. The term, φ is the screening function, wherein:

$$\varphi\left(\frac{r_{ij}}{a_s}\right) = \sum_{n=1}^{4} \Gamma_n \exp\left(\gamma_n \frac{r_{ij}}{a_s}\right) \tag{2.29}$$

where the values of the coefficients Γ_n and γ_n are given in table 2.4. Note that these values are not dependent on species, since the different element pairings are dealt with by the atomic number terms. For reference, these are 24 and 26 for chromium and iron respectively [73].

n	Γ_n	γ_n
1	0.1818	-3.2
2	0.5099	-0.9423
3	0.2802	-0.4029
4	0.02817	-0.2016

Table 2.4: Coefficients for the ZBL screening function [56].

It is tremendously important to maintain continuity of functions, not just in their value, but in the first and second derivatives too. Failing to do so violates conservation of energy. It should be immediately apparent that switching directly from any of the $V_{ij}(r_{ij})$ to the ZBL potential does not preserve continuity. Thus, we use a splining function to bridge the

gap. The splining function is continuous in value, and in first and second derivatives, with the ZBL potential at the beginning of its domain, and likewise continuous with the normal EAM pairwise term at its end, as per equations (2.32) to (2.37). We choose to use a splining function of the form:

$$V_{\text{spline}}(r_{ij}) = \exp\left(f_1 + f_2 r_{ij} + f_3 r_{ij}^2 + f_4 r_{ij}^3 + f_5 r_{ij}^4 + f_6 r_{ij}^5\right) \tag{2.30}$$

	Fe-Fe	Cr-Cr	Fe-Cr
f_1	42.9788764278213	1166.98925191865	-137.376654559008
f_2	-135.545441562262	-4895.55548921096	614.924657879205
f_3	197.285864629164	8163.66247905429	-1033.87004596957
f_4	-143.728683545253	-6724.10876287315	849.87004196916
f_5	50.7129169726354	2731.76870973902	-343.401136475178
f_6	-6.93601245159000	-438.094072278465	54.5679121517284
r_{s1}	1.0 Å	1.0 Å	1.0 Å
r_{s2}	2.0 Å	1.5 Å	1.5 Å

Table 2.5: The f coefficients for the splining functions, see equation (2.30), connecting each EAM potential's default pairwise term to the ZBL potential for the appropriate species pairing. The points, r_{s1} and r_{s2}, mark the transitions between functions, as per equation (2.31).

We generate our own values for the f coefficients of equation (2.30) , see table 2.5. Bonny *et al.* do not provide any reference to ZBL potentials, and thus, neither do they mention splining functions, whereas Ackland *et al.* use a splining function with only a third-order polynomial, where we would prefer a higher-order solution. Defining the two points at which functions meet as r_{s1} and r_{s2}, the pairwise terms for any r_{ij} is then:

$$V_{ij}(r_{ij}) = \begin{cases} \text{ZBL Potential} & \text{for} \quad r_{ij} \leq r_{s1} \\ \text{Splining Function} & \text{for} \quad r_{s1} < r_{ij} < r_{s2} \\ \text{Default EAM Pairwise Term} & \text{for} \quad r_{s2} \leq r_{ij} \end{cases} \tag{2.31}$$

$$V_{\mathrm{ZBL}}(r_{s1}) = V_{\mathrm{spline}}(r_{s1}) \tag{2.32}$$

$$\frac{\mathrm{d}}{\mathrm{d}r_{ij}} V_{\mathrm{ZBL}}(r_{s1}) = \frac{\mathrm{d}}{\mathrm{d}r_{ij}} V_{\mathrm{spline}}(r_{s1}) \tag{2.33}$$

$$\frac{\mathrm{d}^2}{\mathrm{d}{r_{ij}}^2} V_{\mathrm{ZBL}}(r_{s1}) = \frac{\mathrm{d}^2}{\mathrm{d}{r_{ij}}^2} V_{\mathrm{spline}}(r_{s1}) \tag{2.34}$$

$$V_{\mathrm{EAM}}(r_{s2}) = V_{\mathrm{spline}}(r_{s2}) \tag{2.35}$$

$$\frac{\mathrm{d}}{\mathrm{d}r_{ij}} V_{\mathrm{EAM}}(r_{s2}) = \frac{\mathrm{d}}{\mathrm{d}r_{ij}} V_{\mathrm{spline}}(r_{s2}) \tag{2.36}$$

$$\frac{\mathrm{d}^2}{\mathrm{d}{r_{ij}}^2} V_{\mathrm{EAM}}(r_{s2}) = \frac{\mathrm{d}^2}{\mathrm{d}{r_{ij}}^2} V_{\mathrm{spline}}(r_{s2}) \tag{2.37}$$

2.2.3.5 Gauge Transformations

One complication not yet discussed is the issue of *Effective Potential Gauge*. While EAM potentials are designed in such a way that the individual terms have real physical meaning in principle, the fact that they are formed in part by fitting to experimental data means that the energy contribution of each component of equation (2.11) is always somewhat arbitrary, even while the total energy remains physically grounded. The specific way that the energy is spread between the terms is known as the potential's effective gauge. With it not making any overall difference to the final result, it is of little consequence when working in a homogenous system. This changes entirely when one moves to a system involving a mix of atomic species. In particular, consider the electron band density contributions – the ρ terms will be a sum of density contributions from a mix of different atom types. These contributions will have been constructed with the intention of being used with a specific embedding function, calibrated to the developers' chosen means of representing the density mathematically.

Bonny *et al.* use Mendelev *et al.*'s iron potential as their starting point, and develop the chromium, and mixed interactions themselves. These will have been developed to be the best fit for the specific qualities of interest to the author. This being the focus of the development

process means that the new potentials will not necessarily share the effective gauge used by Mendelev; indeed, they do not. Thus, it is necessary to make a gauge transformation.

The gauge transformation is parameterised by the coefficients C and S, see table 2.6, and is performed in two stages. First, with each d-band density contribution, energy is moved from the pairwise term to the embedding function. Transformed terms are denoted by an overhead tilde.

$$\hat{\mathrm{T}}_1 \begin{cases} V_{ij} & \rightarrow \quad \widetilde{V}_{ij} = V_{ij} - 2C_j\phi_{jd} \\ F_{id} & \rightarrow \quad \widetilde{F}_{id} = F_{id}(\rho_{id}) + C_i\rho_{id} \end{cases} \tag{2.38}$$

The second acts on the density terms, and their usage in the embedding functions,

$$\hat{\mathrm{T}}_2 \begin{cases} \phi_{jd} & \rightarrow \quad \widetilde{\phi}_{jd} = S_j\phi_{jd} \\ F_{id} & \rightarrow \quad \widetilde{F}_{id} = F_{id}\left(\frac{\widetilde{\rho}_{id}}{S_i}\right) \end{cases} \tag{2.39}$$

where $\widetilde{\rho}_{id}$ is the sum of transformed density contributions. If not otherwise apparent, after both transformations are performed, the new embedding function is:

$$\widetilde{F}_{id} = F_{id}\left(\frac{\widetilde{\rho}_{id}}{S_i}\right) + \frac{C_i\widetilde{\rho}_{id}}{S_i} \tag{2.40}$$

Observe that if the transformations are applied to a pure species system, they have no net effect. In a mixed system they rescale the density terms and embedding function significantly, while at the same time leaving the total energy unaltered.

	Iron	Chromium
C	0.116093429	-0.0228765475
S	0.0380008812	0.632643294

Table 2.6: Transformation coefficients for use with equations (2.38) and (2.39) [67].

2.2.3.6 Verification

Having written a module for our MD software to implement the Bonny 2011 potential, it is important to be sure that it is functioning as expected. In Bonny *et al.* and Mendelev *et al.*'s papers, they provide a variety of reference values, allowing us to assess the veracity of the properties emerging from our own work; comparisons are made in table 2.7. Additionally, we have calculated the ideal lattice parameter as a function of a system's iron-chromium ratio, and the negative mixing enthalpy property is apparent, see figure 2.3.

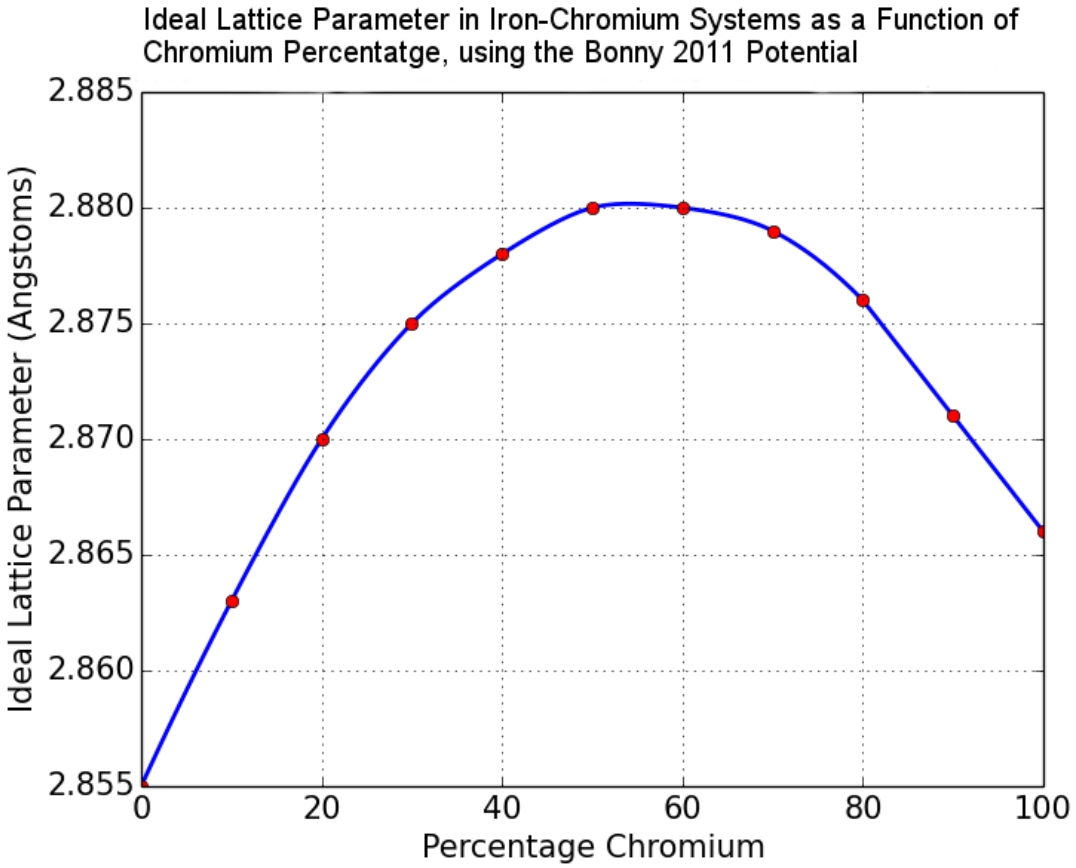

Figure 2.3: Ideal lattice parameters for varying atomic ratios of iron and chromium, as calculated using the Bonny 2011 EAM potential [67]. Observe the negative mixing enthalpy, that is, the lattice parameter is actually larger in some mixed systems than for either of the pure metals.

Property	Our Implementation	Reference Value [67,68]
BCC Pure Iron		
Ideal Lattice Parameter	2.8553 Å	2.8553 Å
Cohesive Energy	-4.122 eV/atom	-4.122 eV/Atom
$E_f\langle 100\rangle$	4.342 eV	4.34 eV
$E_f\langle 110\rangle$	3.528 eV	3.53 eV
$E_f\langle 111\rangle$	4.015 eV	4.02 eV
E_f Vacancy	1.712 eV	N/A: Misprint in source table
BCC Pure Chromium		
Ideal Lattice Parameter	2.866 Å	2.866 Å
Bulk Modulus	215.8 GPa	215 GPa
Cohesive Energy	-4.101 eV/atom	-4.10 eV/Atom
$E_f\langle 110\rangle$ - $E_f\langle 111\rangle$	-0.06832 eV	-0.07 eV
$E_f\langle 110\rangle$ - $E_f\langle 100\rangle$	-0.5769 eV	-0.58 eV
E_f Vacancy	2.519 eV	2.52 eV
BCC Iron Bulk with One Chromium Atom		
$E_f\langle 100\rangle$ FeCr in Fe	3.641 eV	3.64 eV
$E_f\langle 110\rangle$ FeCr in Fe	3.204 eV	3.20 eV
$E_f\langle 111\rangle$ FeCr in Fe	3.480 eV	3.48 eV
BCC Iron Bulk with Two Chromium Atoms		
$E_f\langle 100\rangle$ CrCr in Fe	3.949 eV	3.95 eV
$E_f\langle 110\rangle$ CrCr in Fe	3.264 eV	3.26 eV
$E_f\langle 111\rangle$ CrCr in Fe	3.454 eV	3.45 eV

Table 2.7: In this table, we compare a variety of properties from our implementation of the Bonny 2011 potential to the reference values given in the source papers [67,68]. E_f refers to defect formation energy, as defined in equation (1.1) and $\langle\cdots\rangle$ refers specificly to an SIA of the orientation given.

2.2.3.7 $\langle 110\rangle$ SIAs in an $FeCr_{10\ at.\%}$ Bulk

Bonny *et al.* only give defect formation energies with a monospecies bulk. Since we work predominantly with $FeCr_{10\ at.\%}$ systems, we would like to know something about the energies of SIAs in a mixed system. Specifically, we look at the $\langle 110\rangle$ dumbbell, since this orientation is typically the most stable, and thus most representative of SIAs found in our simulations. This is a less easy value to measure in relation to the previous examples. With our chromium

atoms placed at random in the system, the apparent defect formation energy of a single dumbbell will vary based on the local distribution of species. We find an average value by generating two hundred random $FeCr_{10\ at.\%}$ lattices with 3,456 atoms each, and in these, we calculate the defect formation energy of two hundred randomly placed $\langle 110 \rangle$ SIAs. This process is performed for FeFe, CrCr, and FeCr dumbbells, giving a total of 40,000 data points per pairing. Our average results are 3.45 eV for FeFe$\langle 110 \rangle$, 2.83 eV for CrCr$\langle 110 \rangle$, and 2.75 eV for FeCr$\langle 110 \rangle$. Histograms for the full set of results are shown in figure 2.4. Note that the standard error was significantly smaller than the number of significant figures quoted.

2.3 Minimisation Techniques

For the purposes of analysis, and for transferring to our long-timescale techniques, we often wish to take a molecular dynamics system, with all its atoms in motion, and relax them to stationary positions in a local energy basin. There are multiple methods available to achieve this.

2.3.1 Damped MD

Damped MD is the simplest scheme we can use. The velocity of every atom is set to zero, and a single molecular dynamics step is executed, based on the ordinary interatomic forces. After each step, the atoms' velocities are reset to zero again, and the process is repeated until no atom is subject to a force above a given tolerance. While this method has the advantage of being very unlikely to distort results, it is very computationally expensive compared to the others outlined in this section.

2.3.2 Conjugate Gradient

Originally developed as a numerical technique for solving sets of linear equations, the Conjugate Gradient (CG) method was first developed in 1952 by Hestenes and Stiefel [74]. Since

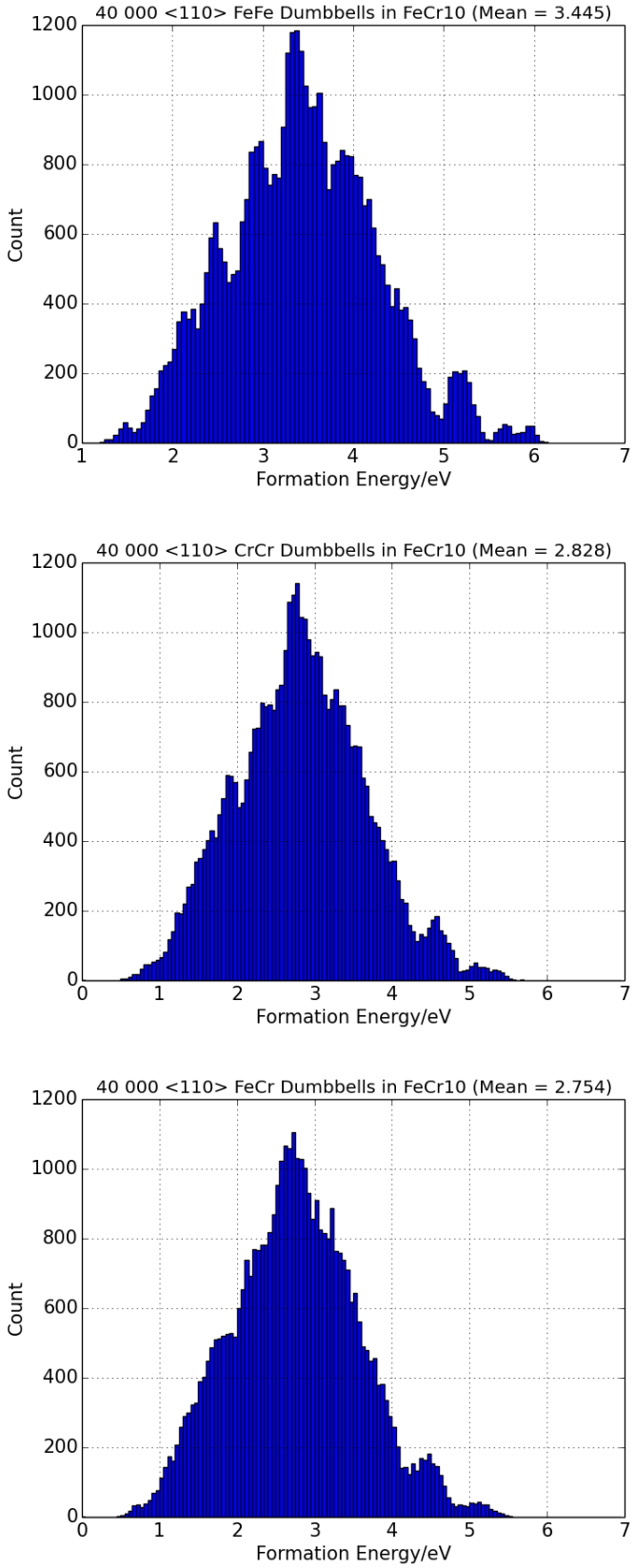

Figure 2.4: Histograms showing the spread of defect formation energies for ⟨110⟩ SIAs in a $FeCr_{10\ at.\%}$ bulk, using the Bonny 2011 EAM potential [67], with each histogram being drawn from 40 000 data points.

its inception, several variants have been produced – the formulation executed in our software is that of Polak and Ribiere [75]. Taking the system force as defined in equation (2.1), we define a gradient function, $\vec{g}(\vec{r}_n)$, as:

$$\vec{g}(\vec{r}_n) = -\nabla\vec{F}_n = \nabla^2 U(\vec{r}_n) \tag{2.41}$$

where subscripts are used to indicate the step index. This vector is then used to advance the system to the next step by,

$$\vec{r}_{n+1} = \vec{r}_n + \alpha_n \vec{d}_n \tag{2.42}$$

where $\vec{d}_n$ is the search direction and α is the linear search parameter, which minimises the equation of force along the search vectors, so as to satisfy equation (2.43).

$$\frac{\mathrm{d}}{\mathrm{d}\alpha}\vec{F}\left(\vec{r}_n + \alpha\vec{d}_n\right) = 0 \tag{2.43}$$

The initial search vector is equal to the gradient function (i.e. $\vec{d}_0 = \vec{g}_0$) , and for all subsequent steps, is given by,

$$\vec{d}_n = \vec{g}_n + \beta_n \vec{d}_{n-1} \tag{2.44}$$

where

$$\beta_n = \frac{\|\vec{g}_n\|^2 - \vec{g}_n \cdot \vec{g}_{n-1}}{\|\vec{g}_{n-1}\|^2} \tag{2.45}$$

One continues to iterate via equation (2.42) until the magnitude of $\vec{F}_n$ falls below the desired tolerance.

2.3.3 L-BFGS-B

The Limited-memory BFGS for Bound constrained optimisation (L-BFGS-B) algorithm is a computationally lightweight implementation of the Broyden-Fletcher-Goldfarb-Shanno (BFGS) method, which has been made publicly available in open source form through the

SciPy library for Python [76–78]. The method begins with an initial guess for the Hessian matrix, $\mathbf{H}_0$, and at each step, the direction is the vector, $\vec{d}_n$, that satisfies,

$$\mathbf{H}_n \cdot \vec{d}_n = \vec{g}_n \tag{2.46}$$

As per equation (2.42), the atoms' positions are updated and the new Hessian approximation becomes,

$$\mathbf{H}_{n+1} = \mathbf{H}_n + \frac{\left[\vec{g}\left(\vec{r}_{n+1}\right) - \vec{g}\left(\vec{r}_n\right)\right]\left[\vec{g}\left(\vec{r}_{n+1}\right) - \vec{g}\left(\vec{r}_n\right)\right]^T}{\left[\vec{g}\left(\vec{r}_{n+1}\right) - \vec{g}\left(\vec{r}_n\right)\right]^T \left(\alpha_n \vec{d}_n\right)} - \frac{\mathbf{H}_n \left(\alpha_n \vec{d}_n\right)\left(\alpha_n \vec{d}_n\right)^T \mathbf{H}_n}{\left(\alpha_n \vec{d}_n\right)^T \mathbf{H}_n \left(\alpha_n \vec{d}_n\right)} \tag{2.47}$$

Again, this process is iterated for as many steps as is necessary to reach a set of atom positions for which $\vec{F}\left(\vec{r}\right)$ has a sufficiently low magnitude to satisfy one's requirements.

Unless stated otherwise, in this work, the L-BFGS-B minimiser is used, falling back to the CG method if it should fail to converge.

2.4 Lattice Defect Analysis Methods

In this section we outline the methods we use to identify lattice defects for the purposes of visualisation, see section 1.3.1.3, and defining defect volumes, see section 3.2.3, in our AKMC software, see section 1.3.1.2.

2.4.1 Identifying Lattice Defects

To discover where lattice defects are present in a system of atoms, we compare it to a reference lattice, and this is depicted in figure 2.5. The comparison allows the identification of vacant sites, atoms sharing a lattice site, and atoms not on a lattice site. This requires that a tolerance must be specified for deviation from the reference lattice, and this is set at 0.9 Å.

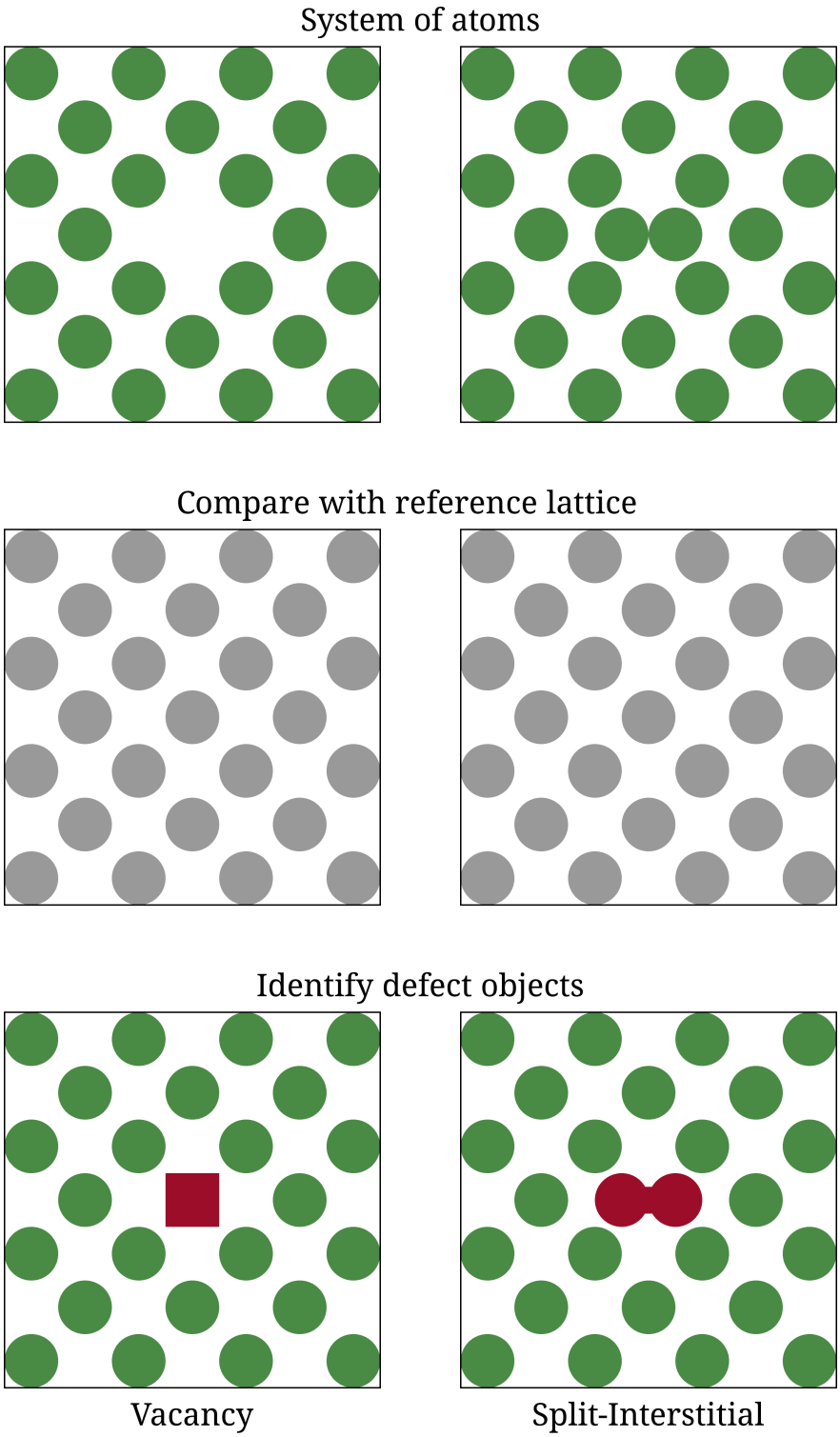

Figure 2.5: Atoman [55] identifies lattice defects in a system by comparing it with a reference lattice. Vacant sites, atoms which are further than a user-specified tolerance from a site in the reference lattice, and multiple atoms sharing a site, are highlighted as defect objects.

2.4.2 Adaptive Common Neighbour Analysis

To refine the analysis of a lattice, one can also consider local variations in its structure. If atoms have a configuration that differs from the general structure of the lattice, these deviations can be flagged using Adaptive Common Neighbour Analysis (ACNA) [79, 80]. One begins with the radial distribution function (RFD), $g(r)$, which describe the number of neighbours an atom has as a function of distance, r, and decomposes it into elements, j, k, and l, respectively denoting the number of shared nearest-neighbours, the number of bonds between shared neighbours, and the number of bonds in longest bond-chain formed by shared neighbours, such that,

$$g(r) = \sum_{jkl} g_{jkl}(r) \tag{2.48}$$

An atom can then be described by the number of neighbours they have in each combination of j, k, and l, denoted N_{jkl}, found by integrating the RDF.

$$N_{jkl} = \frac{4\pi N}{V} \int_0^{r_c} r^2 g_{jkl}(r) \mathrm{d}r \tag{2.49}$$

where $\frac{N}{V}$ is the number of neighbours per unit volume. One defines the cut off, r_c, by the anticipated structure, such that it encompassed all the neighbours considered bonded to an atom. For BCC lattices, one includes the eight first nearest neighbours and six second nearest neighbours. Therefore, one takes the atom's fourteen closest neighbours, and then, ranking them from nearest to farthest with labels $i = 1$ to $i = 14$, r_c is given by,

$$r_{c\,[BCC]} = \frac{1+\sqrt{2}}{2} \left(\frac{2}{\sqrt{3}} \cdot \frac{\sum_{i=1}^{i=8} \mid r_i \mid}{8} + \frac{\sum_{i=9}^{i=14} \mid r_i \mid}{6} \right) \tag{2.50}$$

where r_i is the separation between the atom and its i^{th} neighbour. If the resulting values of N_{jkl} do not match those for the anticipated structure, one can attempt different configurations, until either a match is found, or all possibilities to be considered are exhausted.

Ultimately, one finds a local structure classification for each atom in the lattice.

2.4.3 Defect Replacement Chains

Defect objects can be seen to migrate across an atomic lattice, without any of the atoms involved moving farther than a few lattice sites. It is therefore useful to be able to plot the path of these objects through the system, particularly in the multiple cascade event simulations found in chapter 5. As such, Atoman includes a feature which renders defect replacement chains (sometimes referred to as "spaghetti" in the literature) [81]. Defect replacement chains illustrate the lattice sites visited by defects; consequently, so long as one begins with a perfect lattice, every interstitial defects in the system will be connected to a vacancy by a defect replacement chain, see figure 2.6.

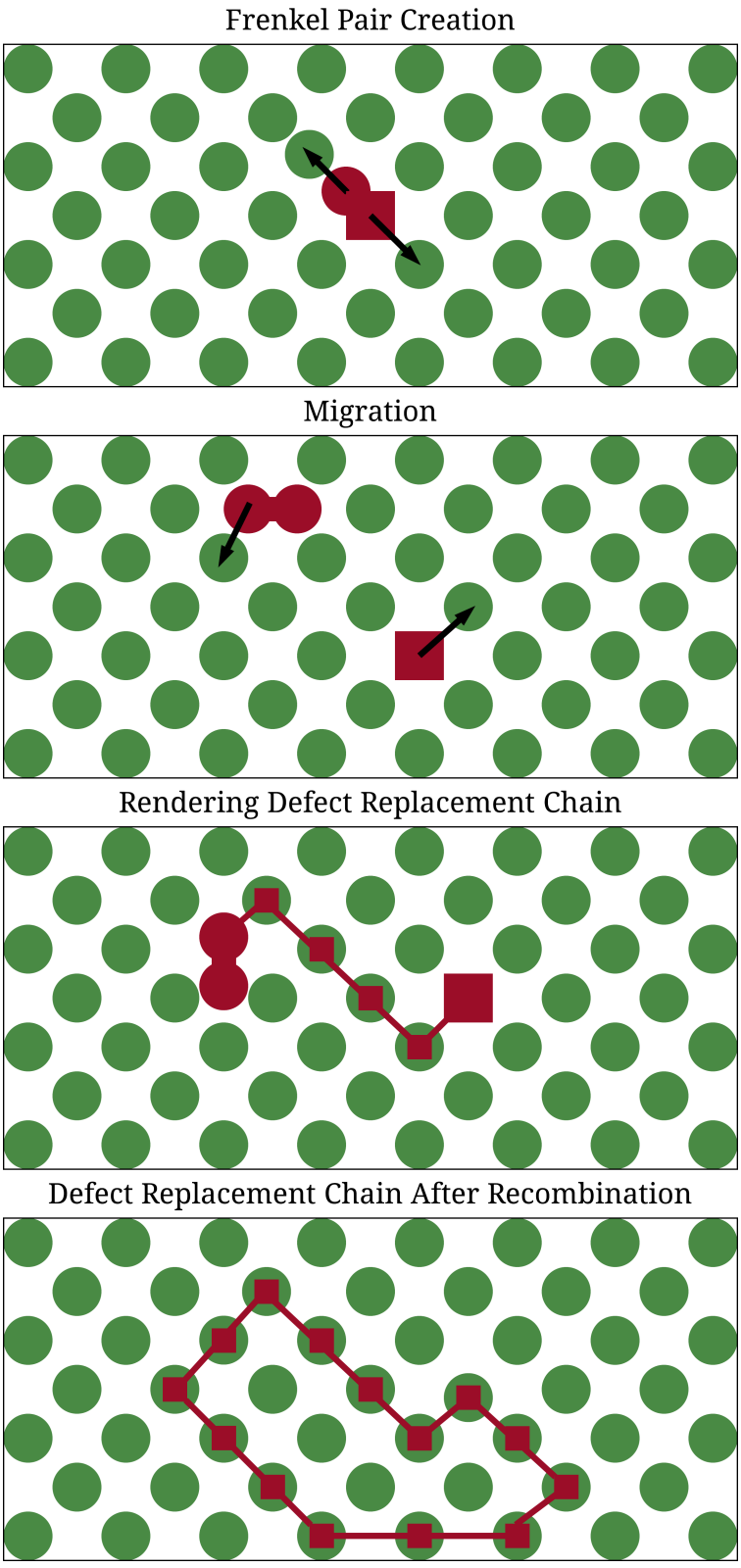

Figure 2.6: Schematic illustration of the rendering of defect replacement chains. When a Frenkel pair is created by the expulsion of an atom from its lattice site, the defect objects created can migrate through the system, hopping from site to site separate to the atoms involved. To mark their path, we can render defect replacement chains. When Frenkel pairs recombine, the chain is left behind – if the interstitial and vacancy that annihilate were created together, the chain will form a closed loop.

Chapter 3

Methodology 2: Adaptive Kinetic Monte Carlo & the Superbasin Method

By the end of our MD simulations, the rate of change, i.e. the migration and annealing of defects, has slowed dramatically relative to the first few picoseconds, and the ballistic phase is considered to have ended. To continue the evolution of the system through our molecular dynamics implementation would be a very poor use of computer resources. A different approach is needed in the recovery phase, one that can achieve long timescales.

3.1 Long Timescale Dynamics with Modified MD

There are a variety of long timescale techniques documented in the literature, and a brief summary of a selection of popular methods is given here. By contrast to the AKMC method presented in section 3.2, these techniques use modifications to the molecular dynamic method to access long timescales.

3.1.1 Parallel Replica Dynamics

Arguably the simplest method, Parallel Replica Dynamics (PRD) takes the system of atoms and creates a number of duplicates. This process exploits parallel processing by assigning

a copy to each processor. The configuration of each copy is slightly altered at random. Then each copy is evolved for a short period, such as to allow its energetics to return to a Boltzmann distribution. During this time, all versions are prohibited from transitioning between states; however, once this has elapsed, the evolution of the modified duplicates is unconstrained. Now, as soon as one copy transitions from one metastable state to another, the simulation is paused. The system clock is advanced by the total time accumulated by all the processors, i.e. if 30 processors each simulate systems for 10 fs, then the system clock is advanced by 300 fs. Then, the algorithm takes the transitioned duplicate and uses it as the basis for a new round of replicas.

The main downfall with this method is its efficiency scaling with respect to the number of processors applied and the average transition rate. Suppose we have a system that makes a state transition once every $\bar{t}$ arbitrary time units of processor time, and that to it, we apply parallel replica dynamics, using a total of p processors. Here, in the same arbitrary time units, we call the total computer time required to prepare the replica systems[1] t_{p}. Since after this process is complete, the average time before one processor sees a transition should be $\frac{\bar{t}}{p}$, the average total computer time per algorithm cycle comes to $t_{\mathrm{p}} + \frac{\bar{t}}{p}$, so the fractional time[2] saved by PRD, κ, is therefore:

$$\kappa = \frac{t_{\mathrm{p}} + \frac{\bar{t}}{p}}{\bar{t}} \tag{3.1}$$

What we see is that as the number of processors increases, one receives diminishing returns on fractional time saved, because although $\frac{\bar{t}}{p}$ tends to 0, one is always left with the duration of the preparation time, t_{p}, which can only be computed in serial. Likewise, if the preparation time is large in relation to the average transition time, then time savings become poor.

[1] i.e. that taken to create the duplicates, to randomise them, and to allow the return of Boltzmann statistics

[2] wherein a value of 1 is no time saved or lost, values less than one and greater than 0 equate to time saved, and any value greater than 1 means the PRD has actually made the computation take longer than before.

Indeed, if the condition,

$$\bar{t} < \frac{pt_p}{p-1} \tag{3.2}$$

is met, then one finds $\kappa > 1$ and PRD becomes a detriment to reduction of computer time. The efficiency scaling is visualised in Figure 3.1.

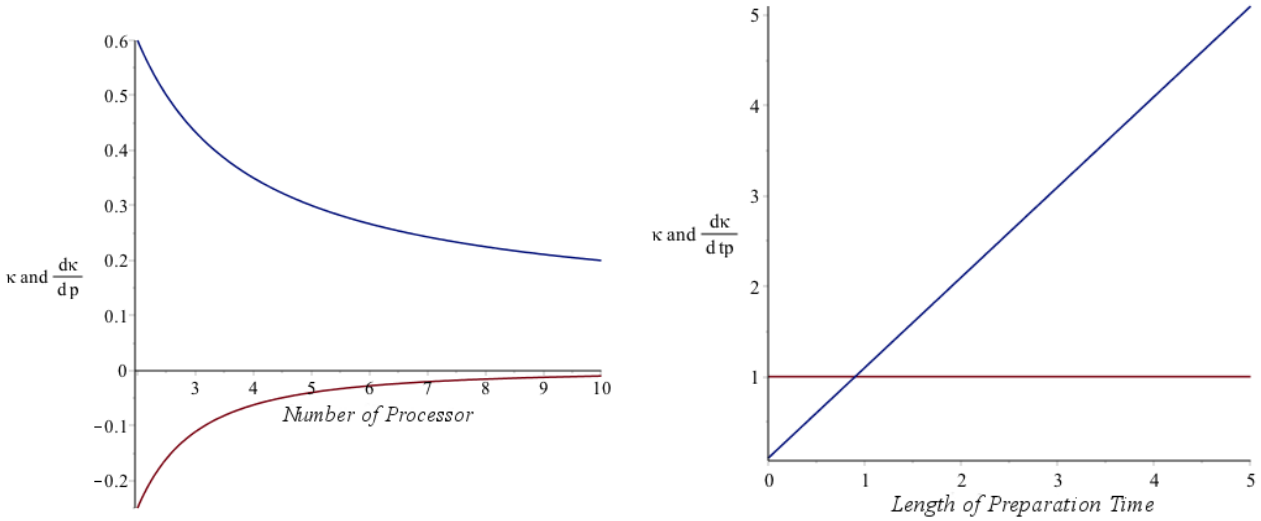

(a) κ with respect to the number of processors used. $\bar{t} = 1$, $t_{\mathrm{p=1}}$

(b) κ with respect to the length of the PRD preparation time. $\bar{t} = 1$, $p = 10$

Figure 3.1: These graphs depict the scaling of efficiency in parallel replica dynamics in terms of the number of processors and the length of the preparation time. The blue lines represent the value of κ as defined in equation (3.1), and red lines represent its first derivative with respect to the free variable.

3.1.2 Temperature Accelerated Dynamics

A small increase in temperature can have a dramatic effect on the rate of a chemical process, owing to the shift in the statistical likelihood of an atom or molecule having the necessary activation energy. The same principle applies here. By simulating the system at a higher temperature, we can achieve much larger state transition rates; however, this technique, known as Temperature Accelerated Dynamics (TAD), is not as simple as it might appear. Consider TAD in the context of the Arrhenius equation [82], which states that for a given temperature, T, and an attempt frequency, A, the rate of occurrence of an event with energy

barrier, E, is given by k, such that,

$$k = A \exp\left(\frac{-E}{k_B T}\right) \tag{3.3}$$

where k_B is Boltzmann's constant.

Due to the exponential term, a small change in the energy term has a dramatic impact on the relative sizes of rate constants. Specifically, there will be an over representation of rare transitions in relation to their otherwise more common counterparts, although by taking a transition state centric view, it is possible to apply corrections to the timesteps corresponding to transitions, yielding more normal behaviour. Unfortunately, it must also be noted that one may find that the potential energy model used becomes inappropriate for the simulated material, due to phase changes or melting. Due to shortcomings such as these, TAD is often considered better suited for preliminary studies of a system [83, 84].

3.1.3 Hyperdynamics

An arbitrary system in some state often has ample energy to cross its local energy barriers, but does not do so quickly because of the improbability of the energy from all its degrees of freedom alligning simultaneously, and this problem is exacerbated in high dimensionality systems. Hyperdynamics is the application of a bias potential within a state to increase the likelihood of a transition, see Figure 3.2. Provided that this bias energy does not exceed the barrier energy, and the technique is applied appropriately across all states, some very large accelerations can be achieved for the system's evolution, while keeping the nature of its dynamics unchanged. Indeed, in their 2001 paper Henkelman *et al.* found boost factors of up to 1400 [83, 84].

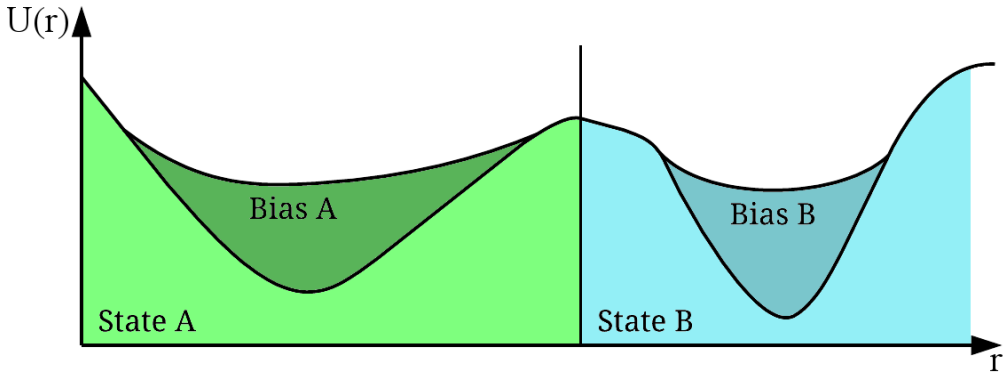

Figure 3.2: Diagram showing two states with bias potentials, serving as examples of the application of Hyperdyamics. Note that continuity to the second derivative (or further, if required) is preserved between the original and bias potentials.

3.2 Adaptive Kinetic Monte Carlo

The methods in the previous section allow the acceleration of the simulation of one's system by considering its dynamics's key driving phenomena, that is, transitions between local minima in the potential energy hypersurface. Adaptive Kinetic Monte Carlo, takes this idea one step further by abstracting the system to a stochastic sequence of jumps between these locations on the energy hypersurface, thus neglecting the explicit simulation of atomic vibrations in the lattice. This abstraction is achieved mathematically through Harmonic Transition State Theory [83]. Considering the system in 3N-dimensional state-space[3], where N is the number of atoms, we imagine the oscillation of the system within a local minima, and then the time it would take on average to climb up to the top of one of the surrounding rank-one saddle points[4], allowing it then to relax into an adjacent state [84, 85], see the schematic in figure 3.3.

Traditionally, to perform a KMC simulation, one would be required to provide a set of precalculated/predetermined moves that the system could make (for example: [86]), however our work uses adaptive methods to assess the state-space around the system's position *on-the-fly* at each step. Thus we do not run the risk of constraining the evolution of the system through lack of understanding of the physics, but it does mean that we must expend

[3] I.e. its potential energy hypersurface
[4] A point on the hypersurface that is a local maxima on one axis, and a minima in all others

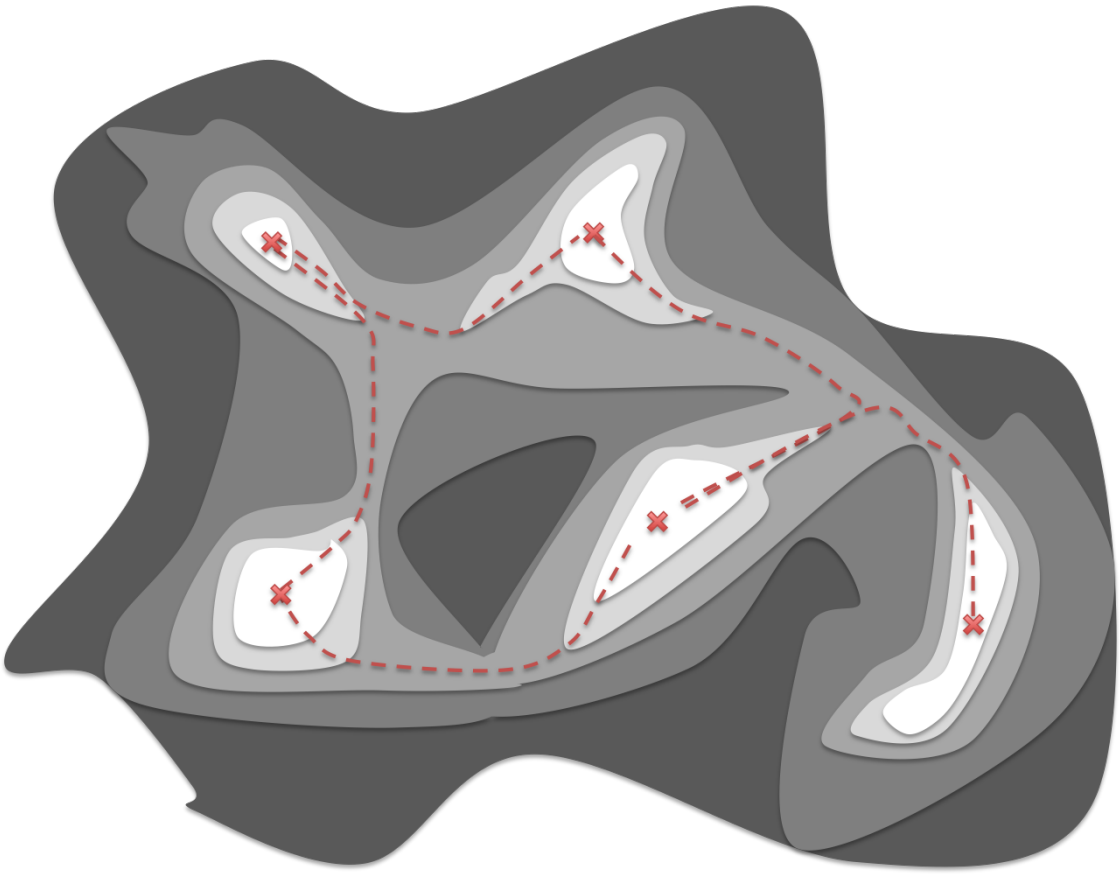

Figure 3.3: Schematic view of state transitions on a potential energy hypersurface. Consider the position of all the atoms represented by the x and y axes, and the potential energy shown as a contour sketch, with high energy levels being the darkest and low energy being the lightest. The system will reside within a local minima, marked by the red crosses. In one of these, we imagine it oscillating around the minima's immediate confines, until it makes a transition over a rank-one saddle into another state (via the red dashed lines representing the minimum energy path). Through Harmonic Transition State Theory, we can calculate an estimate for the average time spent in each state, and the relative probabilities for transitioning into each of the neighbouring states, without having to explicitly model the system trajectory.

computer time to calculate possible transitions, and furthermore, one can never be certain of having found an exhaustive list. To drive our Adaptive Kinetic Monte Carlo (AKMC) simulations, we must turn to the Vineyard equation [84,87], which is based on the Arrhenius equation (see equation 3.3). For a system in a given state, a, a rate, k_b is assigned to the transition to some state, b, such that:

$$k_b = \frac{\prod_i^{3N} \nu_{a\,i}}{\prod_i^{3N-1} \nu_{b\,i}} \exp\left(-\frac{E_b - E_a}{k_B T}\right) \tag{3.4}$$

where T is the system temperature and k_B is Boltzmann's constant. E_a and E_b represent

the potential energy of state a and the rank-one saddle point that must be crossed to reach state b. Similarly, $\nu_{a\,i}$ is the normal mode frequency of state a, and $\nu_{b\,i}$ is the normal mode frequency of the rank-one saddle point that must be crossed to reach state b (see section 3.2.1). Considering that the rate is a positive measure of probability, one sees that transitions with slightly higher energy barriers (i.e. $E_b - E_a$) are strongly penalised by comparison to their lower counterparts, due to the exponential term. Likewise, higher temperatures correspond to higher rates of activity.

Having found the rates for all of the known transitions, their probability of selection is linearly proportional to their rate. The clock advancement, Δt, is made in inverse proportion to the sum of all event rates, and includes a random factor in the interval, $0 < \mu < 1$, [62,84]:

$$\Delta t = -\frac{\ln \mu}{\sum_{i=1}^{i=n} k_i} \tag{3.5}$$

The upshot of this formula, is that the more events one has than can happen, and the more likely these events are, the less time one has to simulate for something to happen.

3.2.1 Pre-Factor Calculation

The normal mode frequencies in equation (3.4) take the form,

$$\nu = \frac{\sqrt{\lambda}}{2\pi} \tag{3.6}$$

where λ is the corresponding eigenvalue of the Hessian matrix. For the purposes of the pre-factor calculation, the Hessian matrix is given by equation (3.7), with each element given for atoms i and j as,

$$\mathbf{H}_{i,j} = \frac{1}{\sqrt{m_i m_j}} \left(\frac{\vec{F}_i^{j+} + \vec{F}_i^{j-} + \vec{F}_j^{i+} - \vec{F}_j^{i-}}{2\delta} \right) \tag{3.7}$$

where m_i and m_j are the atomic masses, and for a small displacement, $\delta = 0.001$, $\vec{F}_i^{j+}$ is the force acting on atom i when j is displaced by $+\delta$, and $\vec{F}_i^{j-}$ is the force action on atom i

when j is displcaed by $-\delta$, with the reverse being true of $\vec{F}_j^{i+}$ and $\vec{F}_j^{i-}$ [88].

The eigenvalues can then be found using the DSYEV function in the LAPACK (Linear Algebra PACKage) library [89, 90].

3.2.2 Transition Discovery Method

AKMC relies on an algorithm to search the local potential energy space for transitions to provide it with a list of possible events *on-the-fly*. The local state space around the current state of the system is explored by randomly displacing atoms. When another local energy minima is discovered the minimum energy path[5] (MEP) between the original and discovered states must be calculated. This means finding a trajectory connecting the states which runs through a rank-one saddle point. The increase in potential energy experienced by the system upon moving from the initial state to the saddle gives the transition's energy barrier, and thus the rate as seen in equation (3.4), with the difference between the final and saddle states being the reverse barrier. Robust calculation of the MEP and saddle is therefore essential for the AKMC method and descriptions of some of the available techniques can be found in sections 3.2.2.1 to 3.2.2.6.

3.2.2.1 Nudged Elastic Band Method

The principle behind the Nudged Elastic Band Method (NEB) is conceptually simple. One takes the position of two adjacent local energy minima in state space and lays a collection of images (on the order of 4 to 20) between them, equally spaced along a straight line. In conjunction with the forces from the potential function, each image is acted on by a force from each of its immediate neighbours, as if elastic bands attached the sequence of images in a chain. One should then be able to find the MEP between the two minima states and through the saddle-point [91, 92].

[5] The red lines on figure 3.3.

Formulation 1

Suppose that one takes an elastic band which is composed of $(N+1)$ images, at vector positions $\vec{R}_0$ through to $\vec{R}_N$. $\vec{R}_0$ and $\vec{R}_N$ themselves are fixed at the initial and final minima respectively, with the remaining images lain out between them. To compute the forces acting on the images one needs to approximate the tangent at each image. The tangent vector, $\vec{\tau}_i$ at some image, i, can be given by:

$$\vec{\tau}_i = \frac{\vec{R}_i - \vec{R}_{i-1}}{|\vec{R}_i - \vec{R}_{i-1}|} + \frac{\vec{R}_{i+1} - \vec{R}_i}{|\vec{R}_{i+1} - \vec{R}_i|} \tag{3.8}$$

which is then normalised to a unit vector, $\hat{\tau}_i$:

$$\hat{\tau}_i = \frac{\vec{\tau}_i}{|\vec{\tau}_i|} \tag{3.9}$$

For a potential $U(\vec{R}_i)$, the corresponding force on an image is $-\nabla U(\vec{R}_i)$. If the spring force acting on i is $\vec{F}_{s,i}$, then its component in parallel to the tangent, $\hat{\tau}_i$, is denoted as $\vec{F}^{\parallel}_{s,i}$. Using $\vec{F}^{\parallel}_{s,i}$, and the component of $-\nabla U(\vec{R}_i)$ perpendicular to $\hat{\tau}_i$, $-\left(\nabla U(\vec{R}_i)\right)^{\perp}$, the net force acting on an image, $\vec{F}_i$, is:

$$\vec{F}_i = \vec{F}^{\parallel}_{s,i} - \left(\nabla U(\vec{R}_i)\right)^{\perp} \tag{3.10}$$

where the right-hand terms are given by,

$$\vec{F}^{\parallel}_{s,i} = k\left(\vec{R}_{i+1} - 2\vec{R}_i + \vec{R}_{i-1}\right) \cdot \hat{\tau}\hat{\tau} \tag{3.11}$$

(for some spring-constant, k) and

$$\left(\nabla U(\vec{R}_i)\right)^{\perp} = \nabla U(\vec{R}_i) - \nabla U(\vec{R}_i) \cdot \hat{\tau} \tag{3.12}$$

Formulation 2

In the first form in which it is presented, NEB will quickly reach a fairly high level of convergence, but will not typically reach the actual MEP itself. Instead, the elastic band will become "kinked", with images either side of the optimal path. Often, this might only have a small impact on the saddle-point energy found. Including some of the perpendicular elastic spring forces can reduce the kinking but this can bring with it the side-effect of corner-cutting in regions of high curvature in the MEP. Thankfully, in their 2000 papers, Henkelman *et al.* have been able to develop some improvements to the NEB method. In one of these papers [91], they present a solution to the kinking problem. Specifically, they propose a new formulation for $\vec{\tau}_i$, this being:

$$\vec{\tau}_i = \begin{cases} \vec{\tau}_i^{+} & \text{for} \quad U(\vec{R}_i) > \vec{R}_i > \vec{R}_{i-1} \\ \vec{\tau}_i^{-} & \text{for} \quad U(\vec{R}_i) < \vec{R}_i < \vec{R}_{i-1} \end{cases} \tag{3.13}$$

wherein,

$$\begin{aligned} \vec{\tau}_i^{+} &= \vec{R}_{i+1} - \vec{R}_i \\ \vec{\tau}_i^{-} &= \vec{R}_i - \vec{R}_{i-1} \end{aligned} \tag{3.14}$$

If an image is at a minima or a maxima, however, a situation arises where neither condition in equation (3.13) is met. In this case, one uses equation (3.15), which smoothly switches between the two tangents when they become equal.

$$\vec{\tau}_i = \begin{cases} \vec{\tau}_i^{+}\Delta U(\vec{R}_i)^{\max} + \vec{\tau}_i^{-}\Delta U(\vec{R}_i)^{\min} & \text{for} \quad U(\vec{R}_i) > \vec{R}_i > \vec{R}_{i-1} \\ \vec{\tau}_i^{+}\Delta U(\vec{R}_i)^{\min} + \vec{\tau}_i^{-}\Delta U(\vec{R}_i)^{\max} & \text{for} \quad U(\vec{R}_i) < \vec{R}_i < \vec{R}_{i-1} \end{cases} \tag{3.15}$$

wherein,

$$\begin{aligned} \Delta U(\vec{R}_i)^{\max} &= \max\left(|U(\vec{R}_{i+1}) - U(\vec{R}_i)|\ ,\ |U(\vec{R}_{i-1}) - U(\vec{R}_i)|\right) \\ \Delta U(\vec{R}_i)^{\min} &= \min\left(|U(\vec{R}_{i+1}) - U(\vec{R}_i)|\ ,\ |U(\vec{R}_{i-1}) - U(\vec{R}_i)|\right) \end{aligned} \tag{3.16}$$

Additionally, the formula for $\vec{F}^{\parallel}_{s\,i}$ is slightly altered.

$$\vec{F}^{\parallel}_{s\,i} = k\left(|\hat{R}_{i+1} - \hat{R}_i| - |\hat{R}_i - \hat{R}_{i-1}|\right)\hat{\tau} \tag{3.17}$$

Note that equation (3.9) continues to hold, as do any other terms from the previous formulation not explicitly altered.

Variable Spring Constants

Henkelman *et al.*'s other proposal is variable spring constant across the band [92]. The force per unit image separation becomes a linear function of potential energy. One then finds a greater density of images around the saddle-point, giving higher resolution where it is needed. With k_i lying in the range $k_{\max} \leq k_i \leq k_{\max} - \Delta k$, it is now given by:

$$k_i = \begin{cases} k_{\max} - \Delta k\left(\frac{U(\vec{R}_{\max}) - U(\vec{R}_i)}{U(\vec{R}_{\max}) - U(\vec{R}_{\text{ref}})}\right) & \text{for} \quad U(\vec{R}_i) > U(\vec{R}_{\text{ref}}) \\ k_{\max} - \Delta k & \text{for} \quad U(\vec{R}_i) < U(\vec{R}_{\text{ref}}) \end{cases} \tag{3.18}$$

where,

$$U(\vec{R}_{\max}) = \max\left(U(\vec{R}_i)\ ,\ U(\vec{R}_{i-1})\right) \tag{3.19}$$

and $U(\vec{R}_{\text{ref}})$ is a reference value, which Henkelman *et al.* set to

$$U(\vec{R}_{\text{ref}}) = \max\left(U(\vec{R}_0)\ ,\ U(\vec{R}_N)\right) \tag{3.20}$$

recalling that $\vec{R}_0$ and $\vec{R}_R$ are the initial and final local minima states.

In spite of these improvements, Henkelman *et al.* still recommend that one only use the NEB Method for a few iterations, before switching to the Dimer method to complete the search.

3.2.2.2 Activation Relaxation Technique

First developed in 1996 by Barkema and Mousseau [93], the Activation Relaxation Technique (ART) method uses a modified force vector to move the system towards a saddle point, from which it may then relax to find the end of the transition. The unmodified force will push a system close to the saddle towards the minima, but if a small deviation from the MEP is made, the system will experience a restoring force because a rank-one saddle is a minima in all but one dimension. To begin the search, the system is displaced by a small random vector. Then modification is made by negating the force component parallel to the direction leading back to the minima, $\vec{F}_{\parallel}$. With the perpendicular component being $\vec{F}_{\perp}$, the modified force, $\vec{F}_{\text{mod}}$ is,

$$\vec{F}_{\text{mod}} = \vec{F}_{\parallel} - \alpha\vec{F}_{\perp} \tag{3.21}$$

where α is given in terms of the relative positions of the system, $\vec{R}$, and the minima, $\vec{R}_0$, such that,

$$\alpha = \frac{\beta}{\mid \vec{R} - \vec{R}_0 \mid_2} \tag{3.22}$$

The $|\ldots|_2$ notation refers to the ℓ^2-norm [94]. β is a positive number, used to control the speed of the motion to the saddle point and would typically take a value of 0.15 [95]. As remarked by L.J. Vernon [96], if the value of β is set too low, the system will follow an inefficient zig-zagged path, and when it is set too high, the estimation of the MEP becomes poor.

One then allows the force to act on the system for a small step, recalculating the modified force in the new position and repeating the process until its magnitude becomes vanishingly small.

3.2.2.3 Relaxation And Translation Method

The Relaxation And Translation (RAT) Method is based on the ART method, but its parallel and perpendicular components at each step are defined with reference to the system's location

at the previous step. The force is applied with a variable step size, based on the value of r_i, where,

$$r_i = \frac{\vec{F}_{\parallel i+1} - \vec{F}_{\parallel i}}{\vec{F}_{\perp i+1}} \tag{3.23}$$

with i marking the step. Then, if the step size at step i is s_i,

$$s_{i+1} = \begin{cases} \frac{6}{5}s_i & \text{for} \quad r_i < 1.2 \\ \frac{1}{2}s_i & \text{for} \quad r_i > 1.2 \end{cases} \tag{3.24}$$

The system's position before and after the application of the force are denoted $\vec{R'}_i$ and $\vec{R}_i$ respectively. After reaching $\vec{R}_i$, the system is is displaced by a unit vector, $\vec{N'}_{i+1}$ such that,

$$\vec{N'}_{i+1} = \frac{\vec{N}_i + \vec{N'}_i}{\mid \vec{N}_i + \vec{N'}_i \mid} \tag{3.25}$$

where $\vec{N}_{i+1}$ and $\vec{N'}_{i+1}$ are the displacement vectors leading from $\vec{R}_{i-1}$ to $\vec{R}_i$ and $\vec{R'}_i$ respectively. The process is iterated until equation (3.26) is satisfied [96,97].

$$\vec{F}_{\parallel} \cdot \vec{N'} > 0 \tag{3.26}$$

3.2.2.4 Dimer Method

In the Dimer Method [84,98], one takes the state of the system in configuration space, and creates two modified images of it. These images represent small shifts (something on the scale of 0.005 Å, for example [84]) in the state space which are equal in size and opposite in direction. That is, a Dimer image is created, centred on the real position of the system[6]. The Dimer is then rotated around the real image until the orientation yielding the lowest potential energy for the Dimer is found. The rotation for this energy minimisation is achieved by taking the difference between the forces acting on the two Dimer images in the direction

[6] One may use a slightly randomised version of real position, so that the algorithm can be used repeatedly to find multiple saddle-points around the local state space.

perpendicular to their separation vector. This is to say that, if $\hat{N}$ is a unit vector specifying the direction of separation between the images, and $\vec{F}_{\mathrm{A}}^{\perp}$ and $\vec{F}_{\mathrm{B}}^{\perp}$ are the forces perpendicular to it, acting on Dimer components, A and B, then these forces, along with net rotational force, $\vec{F}^{\perp}$ are:

$$\begin{aligned} \vec{F}_{\mathrm{A}}^{\perp} &= \vec{F}_{\mathrm{A}} - \left(\vec{F}_{\mathrm{A}} \cdot \hat{N}\right) \hat{N} \\ \vec{F}_{\mathrm{B}}^{\perp} &= \vec{F}_{\mathrm{B}} - \left(\vec{F}_{\mathrm{B}} \cdot \hat{N}\right) \hat{N} \\ \vec{F}^{\perp} &= \vec{F}_{\mathrm{A}}^{\perp} - \vec{F}_{\mathrm{B}}^{\perp} \end{aligned} \tag{3.27}$$

where $\vec{F}_{\mathrm{A}}$ and $\vec{F}_{\mathrm{B}}$ are the total forces on A and B. Rotating the Dimer by small angles iteratively, the forces are adjusted until the Dimer comes to rest. This should be the minimum energy configuration, and this being so means that the Dimer is aligned with the direction of the energy function's lowest curvature.

The next step is to translate the Dimer towards the saddle-point. Unaltered, the net forces acting on the Dimer, $\vec{F}$, would draw it towards a local minima, which is not desired. Instead, the force acting parallel to the Dimer axis, $\vec{F}^{\parallel}$ is inverted, which makes the effective force on the Dimer, $\vec{F}^{\dagger}$, equal to:

$$\vec{F}^{\dagger} = \vec{F} - 2\vec{F}^{\parallel} \tag{3.28}$$

The length of the translation resulting from this force is controlled by a timestep, over which $\vec{F}^{\dagger}$ is integrated. This timestep should be made as large as possible to save computer time, while also staying sufficiently small to allow the Dimer method to converge to the saddle-point.

One way to allow the timestep to remain large is to side-step the issue of eventual convergence by switching to a different, and finer, search scheme when the Dimer is close to a saddle-point; for example, the Minimum Mode Following Lanczos Algorithm, which are described in sections 3.2.2.5 and 3.2.2.6.

3.2.2.5 Minimum Mode Following Algorithm

Published in 1981 by Cerjan and Miller [99], the minimum mode following algorithm can optimise a system to a saddle state configuration using the eigenvectors of the Hessian matrix. Since the computational cost associated with calculating the Hessian grows quadratically with the number of degrees of freedom, using the full matrix is not practical. A 2011 work by Pedersen *et al.* presents a simplified version of the problem; they suggest using only the lowest eigenvalue (the minimum mode) of the Hessian matrix to find the rank-one saddle [100]. Since rank-one saddles are minima in one dimension only, by inverting the force on the system atoms, $\vec{F}$, in the axis along which is it is strongest, one can guide the system towards the saddle. The modified force, $\vec{F}_{\text{mod}}$, can be computed in terms of the eigenvector with the lowest eigenvalue, $\vec{v}_{\text{min}}$, ie.

$$\vec{F}_{\text{mod}} = \vec{F} - 2\left(\vec{F} \cdot \vec{v}_{\text{min}}\right) \cdot \vec{v}_{\text{min}} \tag{3.29}$$

With the modification to the force vector, the saddle point becomes a minima and can then be found using the Lanczos algorithm, as per section 3.2.2.6.

3.2.2.6 Lanczos Algorithm

Discovered in 1950 by Cornelius Lanczos [101], the Lanczos algorithm is an iterative method for finding the eigenvalues and eigenvectors of symmetric matrices. In our case, the matrix we wish to apply the algorithm to is the Hessian approximation, as described in section 2.3. We describe the method using the form suggested by C. C. Paige in 1972 [102], in which the Hessian, $\mathbf{H}$, of size m by m, is converted to a tridiagonal matrix, $\mathbf{T}$ with symmetry such

that $T_{i,j} = T_{j,i}$. The elements of $\mathbf{T}$ are,

$$\mathbf{T} = \begin{bmatrix} \alpha_1 & \beta_2 & & & & \\ \beta_2 & \alpha_2 & \beta_3 & & & \\ & \beta_3 & \alpha_3 & \ddots & & \\ & & \ddots & \ddots & \beta_{m-1} & \\ & & & \beta_{m-1} & \alpha_{m-1} & \beta_m \\ & & & & \beta_m & \alpha_m \end{bmatrix} \tag{3.30}$$

and are derived as follows:

First, set up the initial values

$$\begin{aligned} \beta_1 &= 0 \\ \boldsymbol{v}_0 &= 0 \\ \boldsymbol{v}_1 &= \text{random unit vector } (\mid \boldsymbol{v}_1 \mid = 1\ ) \end{aligned} \tag{3.31}$$

Then, looping over elements i in the range 1 to $m-1$:

$$\begin{aligned} \boldsymbol{w}_i &= \mathbf{H}\boldsymbol{v}_i \\ \alpha_i &= \boldsymbol{w}_i \cdot \boldsymbol{v}_i \\ \boldsymbol{w}_i &= \boldsymbol{w}_{i-1} - \alpha_i \boldsymbol{v}_i - \beta_i \boldsymbol{v}_{i-1} \\ \beta_{i+1} &= \|\boldsymbol{w}_i\| \\ \boldsymbol{v}_{i+1} &= \frac{\boldsymbol{w}_i}{\beta_{i+1}} \end{aligned} \tag{3.32}$$

For the m^{th} elements:

$$\begin{aligned} \boldsymbol{w}_m &= \mathbf{H}\boldsymbol{v}_m \\ \alpha_m &= \boldsymbol{w}_m \cdot \boldsymbol{v}_m \end{aligned} \tag{3.33}$$

The eigenvector with the lowest eigenvalue of the resulting matrix can then be estimated using the LAPACK library's implementation of QR factorisation [90, 103, 104], repeating the Lanczos method until a desired tolerance is met.

3.2.2.7 Saddle Search Method Chosen

In existing work with iron systems by T. Lazauskas in 2014 [88], a combination of methods, using Dimer techniques to estimate saddle positions, and the MMRA with Lanczos eigenvector calculations to refine it, was shown to be effective and efficient. Similarly, M. Yu [97] demonstrated that while the ART method was the fastest method, both it and the RAT methods were outperformed by Dimer/MMFA searches in practical terms, with the latter producing more unique transitions for real computing power expended when the number of failed searches was considered. As such, this is our choice of saddle search method also.

3.2.3 State Categorisation

Attempting to perform transition searches on the entire system is very inefficient when only a small fraction of atoms in the vicinity of defects have a non-negligible likelihood of moving. For this reason, our AKMC software divides the lattice into subsystems called defect volumes. The current state is compared to a reference lattice, and by their comparison, interstitial defects and vacancies are located, see section 2.4. A sphere is then drawn around each defect object; all atoms within this sphere are included in the defect volume, and if multiple defects fall within each other's sphere, they are treated as one defect volume. Using Brendan D. McKay's "nauty" (No AUTomorphisms, Yes? [*sic.*]) library, a hexadecimal code, referred to as a hashkey, is generated, based on the geometry of the defect volume [105, 106]. Transition searches are then performed on the atoms of each defect volume. Every unique transition found is stored in a file associated with that hashkey, meaning that if a defect volume is later encountered with isomorphic geometry, and therefore the same hashkey, those transitions can be reused, saving the computational expenditure of the search process for that AKMC

step.

3.3 The Super-Basin Method

3.3.1 Introduction

AKMC allows one to achieve long-timescale-dynamics, but there is an issue known as the low barrier flicker problem that can limit its efficiency, and this we wish to eliminate. Suppose, that one has a region with a high density of states connected by low energy transitions. Most likely, transitions between these states will not represent large reconfigurations of the atoms, yet they will have highly favourable rates, and thus will drive down time advancements. One is then left with our system flittering between these very similar states, occupying computer time, while not simulating any large steps forward in time. The solution is referred to as the Super-Basin Method. For a given threshold, we can combine states connected by low energy transitions into a low energy basin, that is, a super-state jointly representing them. For this basin, one can calculate an aggregate rate of escape via higher energy transitions, allowing one to integrate out the uninteresting activity, and more importantly, making larger advances of time accessible to the simulations [107, 108]. We attempt to depict this schematically in figure 3.4.

3.3.2 The Mean Rate Method

The mean rate method (MRM), derived by Puchala *et al.* in 2010 [107], is used to calculate the average time a system will spend trapped in the transient states of a low energy basin, before escaping to an absorbing state. Defining the mean time spent in the i^{th} transient state before the basin is escaped as τ_i, a matrix of transition probabilities, $\bar{\bar{\mathbf{T}}}$, can be constructed, whose elements the mean rate method gives as,

$$T_{i,j} = \tau_i^1 R_{i \to j} \tag{3.34}$$

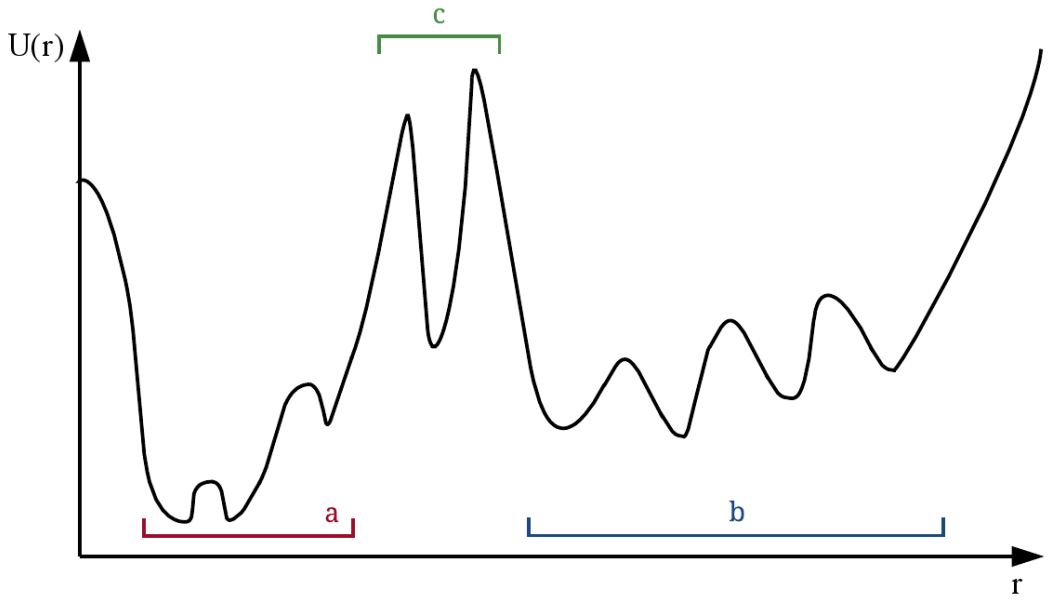

Figure 3.4: Schematic view of a section of state space containing two basins, **a** and **b**. Without the super-basin method, this system would dwell in one of those regions, consuming large durations of computer time, while advancing the system time little. By drawing a basin around **a** and **b**, we can integrate out the internal reconfigurations within these regions and calculate a general rate of escape to state **c**, making larger advances of system time [107].

where $T_{i,j}$ is the probability of transitioning from basin states i to j, with the sum over k representing all transient and absorbing states, and R is the rate for the transition between the states marked in superscript in the direction indicated by the arrow. τ_i^1 is the mean time spent in each basin state per single visit, such that,

$$\tau_i^1 = \left(\sum_k R_{i \to k} \right)^{-1} \tag{3.35}$$

The occupational probability vector $\bar{\mathbf{\Theta}}(m)$ is the probability of still being in a transient basin state, i, in the interval between some transition, m, and the next, given by,

$$\bar{\mathbf{\Theta}}(m) = \bar{\bar{\mathbf{T}}}^m \bar{\mathbf{\Theta}}(0) \tag{3.36}$$

where $\bar{\bar{\mathbf{T}}}^m$ is the subset of $\bar{\bar{\mathbf{T}}}$ for m's initial and final states, and $\bar{\mathbf{\Theta}}(0)$, the occupational probability vector for the transition in which the system enters the basin, is defined with elements such that for each state, i,

$$\bar{\Theta}_i(0) = \begin{cases} 1 & \text{when } i \text{ is the state by which the basin is entered} \\ 0 & \text{for all other states} \end{cases} \tag{3.37}$$

The occupational vector probabilities then sum to $\bar{\mathbf{\Theta}}^{\text{total}}$ (for the identity matrix $\mathbf{I}$),

$$\bar{\mathbf{\Theta}}^{\text{total}} = \sum_k^{\infty} \bar{\bar{\mathbf{T}}}^m \bar{\mathbf{\Theta}}_i(0) = \left(\mathbf{I} - \bar{\bar{\mathbf{T}}}\right)^{-1} \bar{\mathbf{\Theta}}(0) \tag{3.38}$$

for all possible moves, $m = 0 \rightarrow \infty$. This then relates the mean total time spent in basin state i to the mean time spent per visitation by,

$$\tau_i = \tau_i^1 \bar{\mathbf{\Theta}}_i^{\text{total}} \tag{3.39}$$

This means that the mean rate to escape the basin from transient state i to absorbing state j is,

$$\langle R_{i \rightarrow j} \rangle = \frac{\tau_i}{\sum_k \tau_k} R_{i \rightarrow j} \tag{3.40}$$

with k representing all the transient states.

The sum of the mean time spent in each transient state gives the mean total time that system will spend in the basin, before escaping to an absorbing state, that is,

$$\tau_{\text{basin}} = \sum_i \tau_i \tag{3.41}$$

and is used for AKMC timesteps. When a MRM based atomistic modelling technqiue was proposed by Béland *et al.* in 2011 [109], they envisioned it used for whole system lattices, and therefore that only one basin would exist at a time; however in our AMKC method, the

system is divided into defect volumes, upon whom transitions are discovered independently, and as such, allow for multiple basins[7] to be constructed *on-the-fly*.

3.3.3 Problems with Super-Basin Method Implementation

3.3.3.1 Duplicate Hashkey Problem

For the super-basin method to work we must have a well defined concept of individual states. The LAKMC code achieves this using the defect volumes' hashkey, centre of mass ($\vec{x}_{\mathrm{COM}}$), and moment. The centre of mass calculation does not use the real masses of the atoms, instead treating all atoms in the defect volume as equal point masses, such that for N atoms with positions $\vec{x}_0$, $\vec{x}_1$, ... , $\vec{x}_N$,

$$\vec{x}_{\mathrm{COM}} = \frac{1}{N}\sum_{i=1}^{N}\vec{x}_i \tag{3.42}$$

The moment, $\vec{x}_{\mathrm{mom}}$, is then given as a function of the separation of each atom from the centre of mass,

$$\vec{x}_{\mathrm{mom}} = \frac{1}{N}\sum_{i=1}^{N}\left(\vec{x}_i - \vec{x}_{\mathrm{COM}}\right)^2 \tag{3.43}$$

Most of the time, with a small tolerance for variation in COM and moment, these three attributes are enough to uniquely identify states within a super-basin, however there is a flaw in this system. When a defect volume has atoms very close to its spatial limits, changes in the broader system can effect slight changes in the exact position of these atoms, causing them to cross the defect volume boundary, be it inwards or outwards. Since nauty's algorithm is dependent on the number of atoms in the defect volume, the hashkey of the state changes. To prevent this from causing major problems with the housekeeping of the super-basin system we must permit multiple hashkeys to be associated with a single basin state, which we refer to as duplicates, calling the original version of the defect volume the primary.

Whether the duplicate hashkey problem is a major problem or a minor inconvenience depends on how frequently such states appear in the specific system studied. The original

[7] Such that, № basins $\leq$ № defect volumes.

implementation of the super-basin method was written by erstwhile colleague, Miao Yu, as part of his doctoral project simulating surface deposition growth of CdTe [97]. In his system, duplicates did not pose a large problem, and this implementation had only a partial solution.

3.3.3.2 Detailed Balance

Another issue known to exist with the original implementation of the super-basin method, as noted in section 8.2 of Miao Yu's thesis, is the lack of symmetry in the internal connections it produces. The method operates under the presumption of detailed balance, which is to say, every transition within the basin must have a partner, whose connection runs between the same two states in the reverse direction, with the corresponding energy barriers, see figure 3.5.

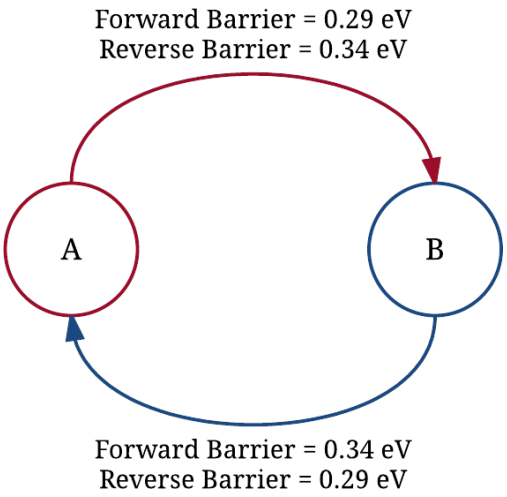

Figure 3.5: Illustration of the concept of detailed balance; if a transition from A to B is added (red) to a low energy basin, then so must a corresponding transition from B to A (blue), switching the forward and reverse barriers.

3.3.4 New Implementation

For some systems, duplicate hashkey states are very common, and correct detailed balance is vital for reliable results. To fix these two problems required a substantial overhaul of the super-basin method implementation in LAKMC – the methodology described in section 3.4

describes the software in its amended condition. Note that Miao Yu's implementation of the MRM is used unaltered [97].

3.4 Implementation

An overview of the operation of LAKMC is shown in flowchart form in figure 3.6, and is supplemented by figure 3.7, which shows the process for adding transitions to the basin structure. The method by which we detect duplicate hashkey states is shown in figure 3.8.

3.4.1 Low Barrier Criteria

When each transition is found, it must be examined to determine whether it qualifies as a low barrier transition. The user specifies a threshold energy and if *either* the forward or reverse barrier is below this value, the transition is marked as low barrier, regardless of how large the other is. This is because, if the system was to escape of over a high barrier, the low barrier would give a high probability to move back into the basin from which it came. Note that is is important not to set the low barrier threshold too high, lest the system does not find any escaping transitions. As will become apparent in section 3.4.2, a complete lack of transitions to absorbing states will have undesired effects.

3.4.2 Basin Exploration

To construct our basins *on-the-fly*, we begin with an ordinary search procedure on each defect volume in the system. If a low barrier transition is found, its initial and final states are added to a new basin structure and any non-low barrier transitions found from the initial are added as moves to absorbing states. The initial state is then considered "explored" and the defect volume may transition to either the other basin state, or one of the absorbing states (if any have been found). A defect volume whose hashkey has never been searched is considered "unexplored" and a basin state which has been discovered as the end defect

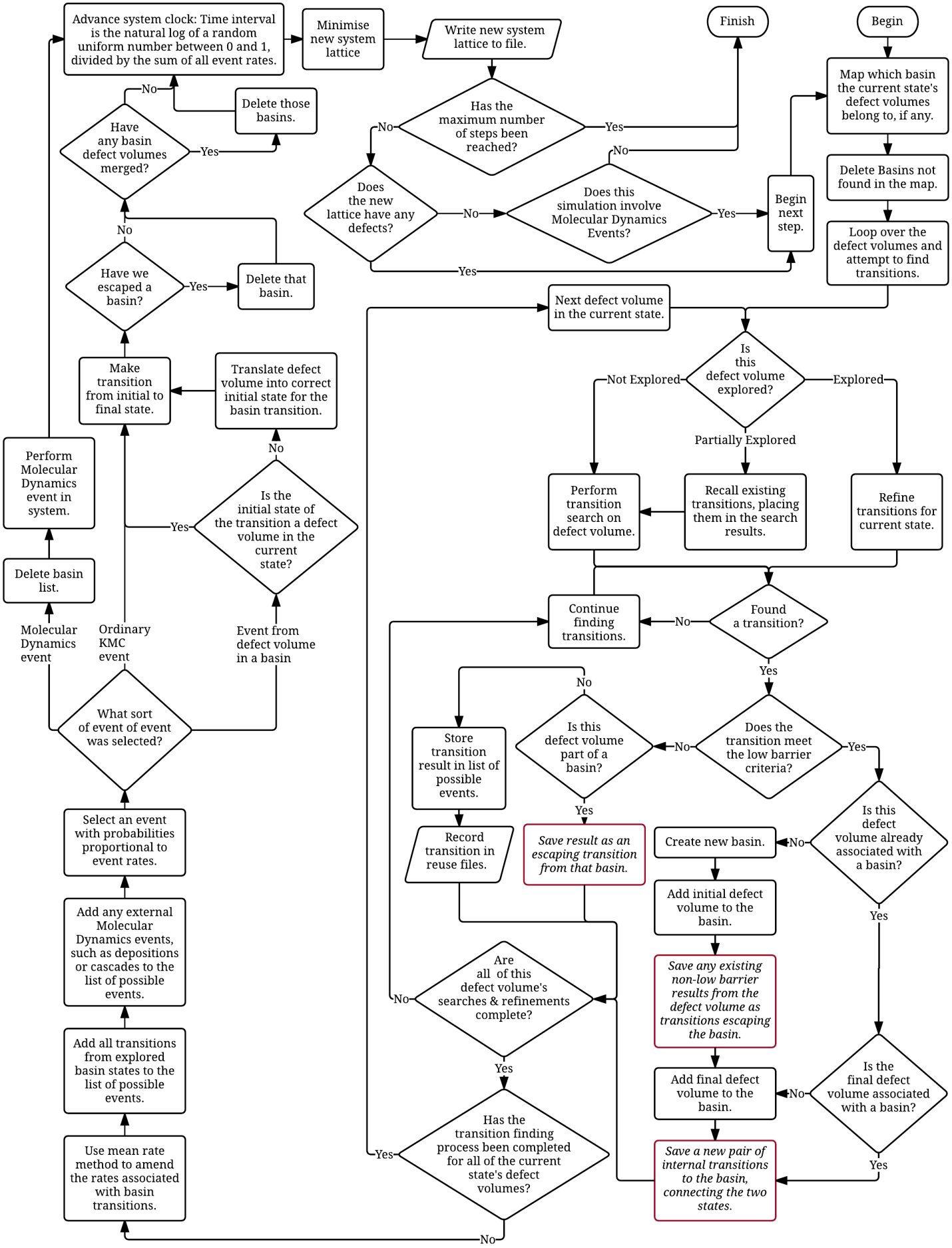

Figure 3.6: Overview of the algorithm used by the LAKMC software implementation. The process by which transitions are saved to the basin (the actions bordered in red with *italic* text) is described in figure 3.7.

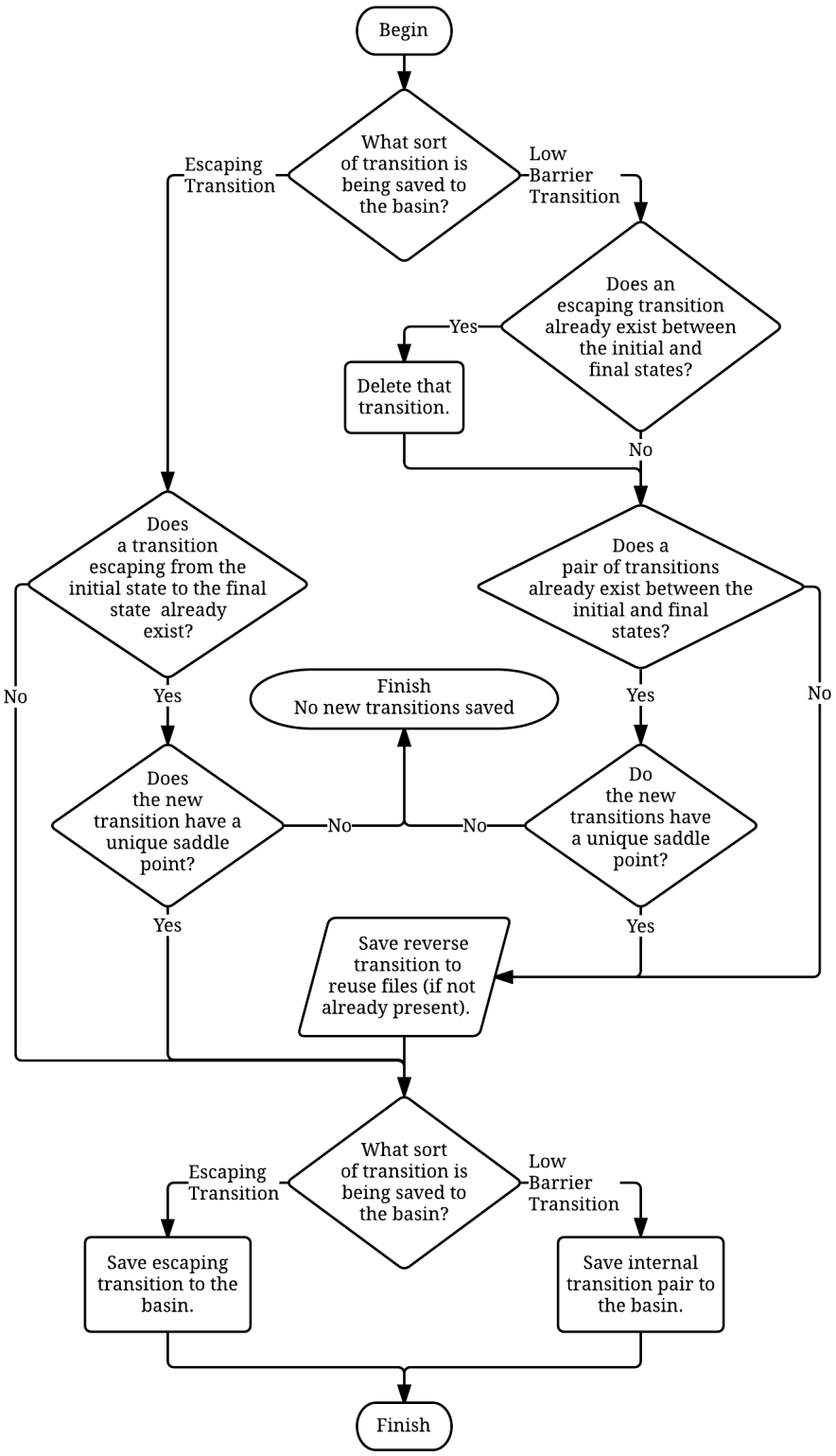

Figure 3.7: Procedure for saving transitions in a basin.

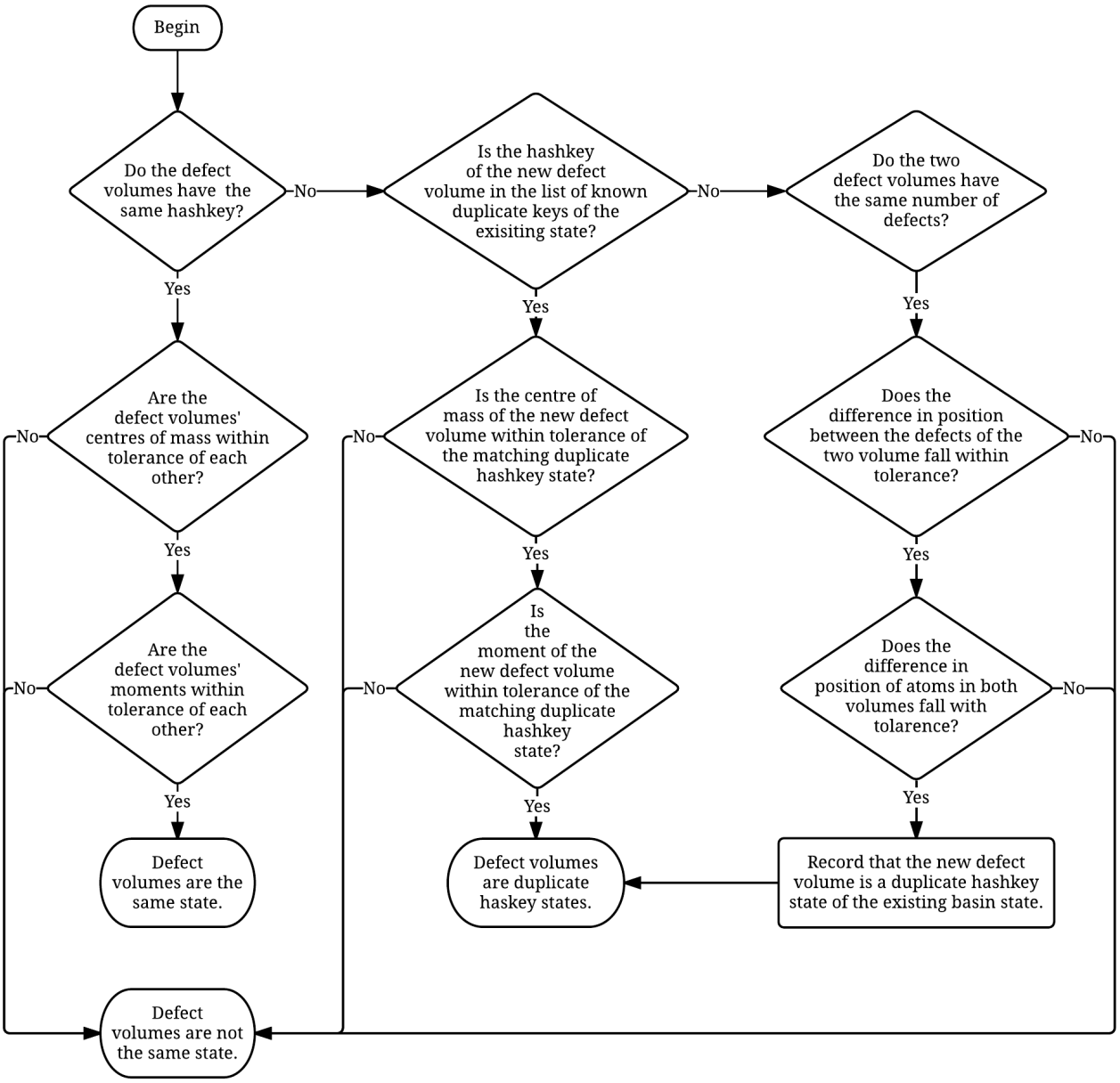

Figure 3.8: Procedure for identifying whether a defect volume is an existing basin state, and if so, whether it is the primary version or a duplicate hashkey state.

volume of a low barrier transition is considered "partially explored"; before being visited, the only transitions known to it will be the reversed versions of transitions going to it from other basin states. Each time a defect volume that is a basin makes a transition, it is permitted to move only to an unvisited basin state or to an absorbing transition, see figure 3.9. Therefore, when a basin is fully explored, the only option is exit the structure; as such, if no escaping transitions have been found, there will be no valid moves available to the defect volume in the basin and we would advise the user to reduce their low barrier threshold.

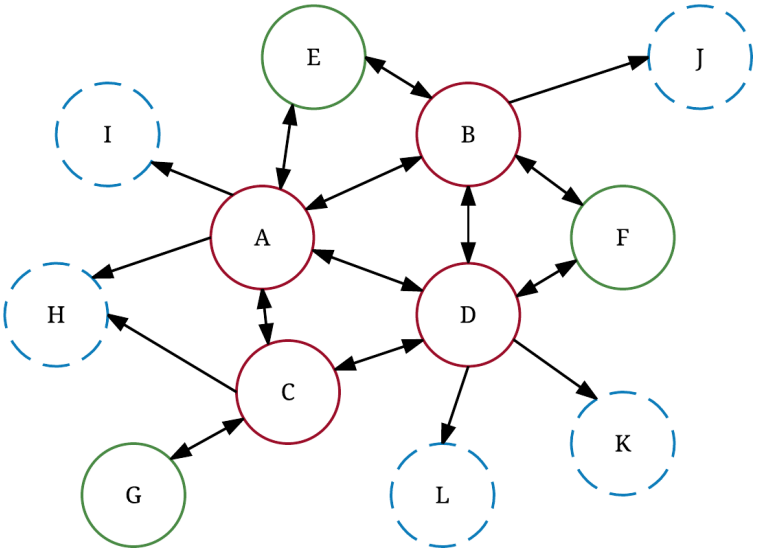

Figure 3.9: In the following basin structure, with explored states, [A, B, C, D], a move may be made only to one of the partially explored states, [E, F, G], which were discovered as the end points of transitions from the explored states, or to one of the absorbing states, [H, I, J, K, L]. Single headed arrows indicate non-low barrier transitions which escape to absorbing states, and double headed arrows indicate pairs of low barrier transitions, internal to the basin.

3.4.3 Escaping a Basin

When a defect volume escapes from a basin, the structure is deleted. Ideally, this should only ever happen if a move to an absorbing state is made; however, in a system of multiple defect volumes, such as a post-collision cascade lattice, two or more defects may migrate sufficiently close to each other to be considered part of one volume. Since the new state occupied will then have a completely different hashkey and number of defects from any of the previous configurations, it is not recognised as a state of any of the basins from which the defects

came. This process can happen in reverse too, when defect objects move sufficiently distant to be considered as in separate defect volumes. An additional example can occur when a transition is found to a state of relatively low stability – later, when the defect volume moves to that state, changes in the wider system may mean that the state is no longer stable. As such, during the post-transition minimisation, the defect volume may take on a completely different configuration, not found anywhere in its basin. In such cases as these, the affected basin(s) must be deleted, and we begin construction of new basin structures as appropriate.

Chapter 4

Collision Cascades and Displacement Threshold Energy

4.1 Collision Cascades

To begin our study of radiation degradation effects, we used our molecular dynamics software to study the main process by which damage is introduced into solid matter – collision cascades. These occur when an energetic particle sheds some of its momentum to an atom, causing it to recoil. The recoiling atom, which we refer to as the Primary Knock-On Atom (PKA), in turn, interacts with its neighbours, displacing them to create pairs of vacant lattice sites and interstitial atoms. To collect representative statistics, our sets of PKA vectors comprise of over a hundred points, evenly sampling the unit sphere [110]. It was once common for those studying collision cascades to use a single, highly off lattice orientation for the initial vector of their PKA, which would allow fewer simulations to be conducted, while avoiding introducing bias through effects such as channelling, and we discuss the impact of this method in section 4.4.

In section 4.1, we present a variety of computational experiments with single collision cascade events, discussing the recovery process in section 4.2. Aside from the total number of Frenkel pairs produced, we also consider the concentration of chromium among interstitial

atoms with respect to the bulk. A disparity could be an indication of the beginning of chromium segregation – those using FeCr materials to construct a reactor will be keen to avoid regions of chromium depletion, lest these begin to oxidise. For later comparison, the rate at which chromium would appear in defects if there were no species bias is shown in table 4.1.

Table 4.1: In this table, for a given bulk concentration of chromium, α, the hypothetical corresponding rate of occurrence of chromium in defects, if there were no species bias, is shown.

Cr in Bulk	Cr LIAs	CrFe SIs	CrCr SIs	Cr Defect Atoms
α	α	$2(\alpha - \alpha^2)$	α^2	α
1%	1%	1.98%	0.01%	1%
5%	5%	9.5%	0.25%	5%
10%	10%	18%	1%	10%

Descriptions of the results are found in sections 4.1.1 to 4.1.3, while a discussion of their implications may be found in 4.1.4.

4.1.1 PKA Energy

We began our investigation by considering the effect of PKA energy on collision cascades in $FeCr_{10\ at.\%}$, and in these experiments, we did not thermalise the lattices prior to the event, applying a Berendsen thermostat at 0 Kelvin during the simulation. Simulations with PKA energies of 1, 2, and 5 keV were conducted, and to contain each set of collision cascades, 54,000 atoms, 128,000 atoms and 500,094 atoms were used respectively. Three sets of 108 PKA directions, distributed over the unit sphere, were used in eighteen randomly generated systems of appropriate size[1].

To allow the cascade energy to dissipate, and to ensure that the end of the ballistic phase had been passed, the 1 and 2 keV simulations were run to 6 ps, with the 5 keV simulation running to 10 ps. The evolution of the number of Frenkel pairs produced by the cascades is

[1]This should mean that 5832 simulations were ran for each energy, but technical problems with the automation scripts lead to slightly fewer for the 1 keV and 5 keV sets.

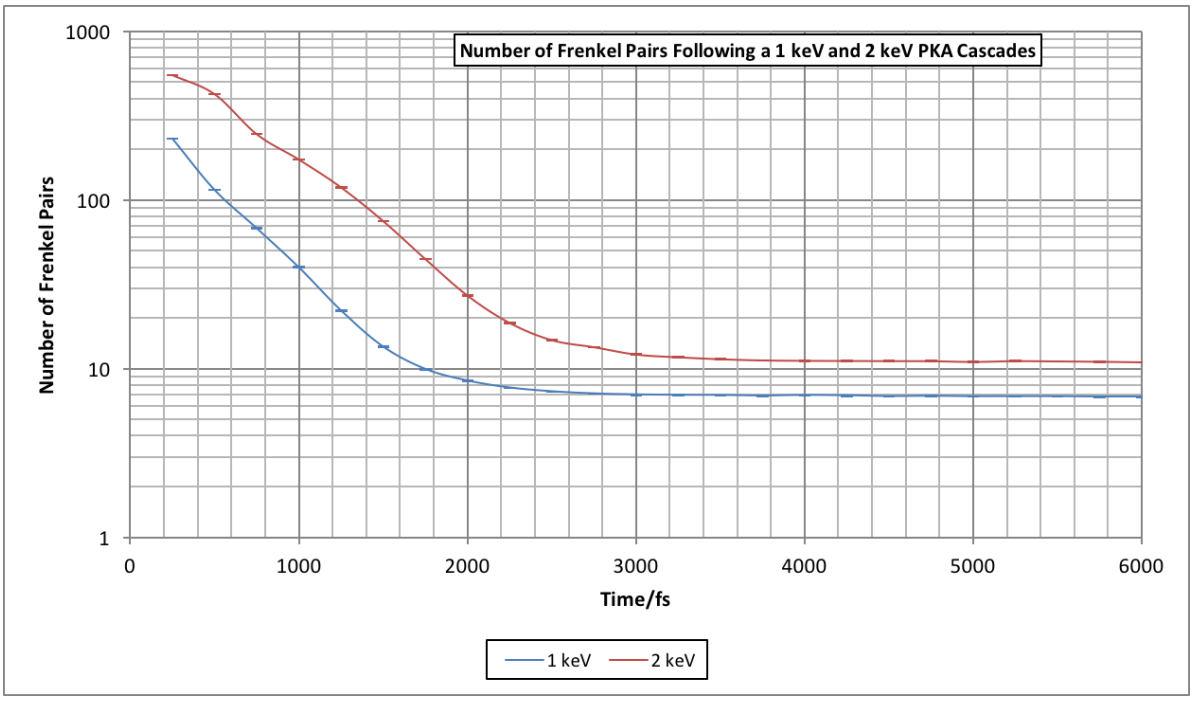

Figure 4.1: Evolution of the number of Frenkel pairs produced by collision cascades in $FeCr_{10\ at.\%}$ with PKAs of energies 1 keV (5553 simulations) and 2 keV (5832 simulations). Please note that the number of Frenkel pairs is presented on a logarithmic axis.

shown in figure 4.1[2]. Final defect statistics are shown in tables 4.2 and 4.3, which show the final state of the lattices before and after minimisation respectively.

There is no tangible difference between the defect atoms' chromium content, or the total number of Frenkel pairs in the two tables, but upon relaxation, lone interstitial atoms show a tendency to form split-interstitial defects. The relationship between the number of Frenkel pairs remaining at the end of the simulation is approximately linear, although this relationship must break down for low cascade energies, such as to intercept the y-axis at the origin in figure 4.2. chromium consistently appears in interstitial atoms at a lower rate than in the bulk for all PKA energies, and our error bars are not sufficiently small to establish a statistically significant correlation with respect to it, see figure 4.3. With regard to the specific types of interstitial defects, seen in figure 4.4, we consistently find across PKA energy, FeCr and CrCr split-interstitials are under-represented, with no significant change

[2]Given the very large file sizes associated with the 5 keV PKA simulations, only the final lattice at 10 ps was stored, hence it is absent from figure 4.1

seen after minimisation. Lone chromium interstitials are over-represented, and this tendency is inversely proportional to the overall chromium concentration. Additionally, after lattice minimisation, this over representation is greatly exaggerated, suggesting that lone chromium interstitials are more stable than their iron counterparts, and that it is the latter that are mostly responsible for the overall reduction of LIAs post-minimisations.

Table 4.2: Lattice defects found in $FeCr_{10\ at.\%}$ systems following collision cascade of varying energy, simulated at 0 Kelvin. 5553, 5832, and 5825 simulations were performed for the 1, 2 and 5 keV results respectively (no post-cascade lattice minimisation). The 1 keV and 2 keV simulations ran for 6 ps and the 5 keV simulations ran for 10 ps.

PKA Energy	Defect Atoms of which Cr (%)	Lone Interstitials	Split-Interstitials	Total Frenkel Pairs
1 keV	6.9 ± 0.3	0.406 ± 0.010	6.39 ± 0.02	6.80 ± 0.03
2 keV	7.4 ± 0.3	0.89 ± 0.15	10.02 ± 0.03	10.92 ± 0.04
5 keV	7.4 ± 0.3	2.08 ± 0.03	18.4 ± 0.06	20.50 ± 0.07
PKA Energy	LIAs of which Cr (%)	SIs of which FeFe (%)	SIs of which FeCr (%)	SIs of which CrCr (%)
1 keV	21.3±0.5	87.4±0.4	12.1±0.4	0.46±0.09
2 keV	15.5±0.5	86.4±0.4	13.1±0.4	0.49±0.09
5 keV	13.3±0.4	86.2±0.4	13.3±0.4	0.47±0.09

Table 4.3: Lattice defects found in $FeCr_{10\ at.\%}$ systems following collision cascade of varying energy, simulated at 0 Kelvin. 5553 and 5832 simulations were performed for the 1 and 2 respectively (with post-cascade lattice minimisation – given the high CPU hour cost associated with the L-BFGS-B/CG minimisation for larger systems, no minimised results appear for the 5 keV PKA simulations.). These simulations ran for 6 ps.

PKA Energy	Defect Atoms of which Cr (%)	Lone Interstitials	Split-Interstitials	Total Frenkel Pairs
1 keV	7.0±0.3	0.258±0.008	6.53±0.02	6.78±0.03
2 keV	7.3±0.3	0.616±0.014	10.29±0.03	10.91±0.04
PKA Energy	LIAs of which Cr (%)	SIs of which FeFe (%)	SIs of which FeCr (%)	SIs of which CrCr (%)
1 keV	64.9±0.3	86.5±0.5	13.0±0.5	0.49±0.09
2 keV	61.6±1.3	85.9±0.4	13.6±0.4	0.54±0.10

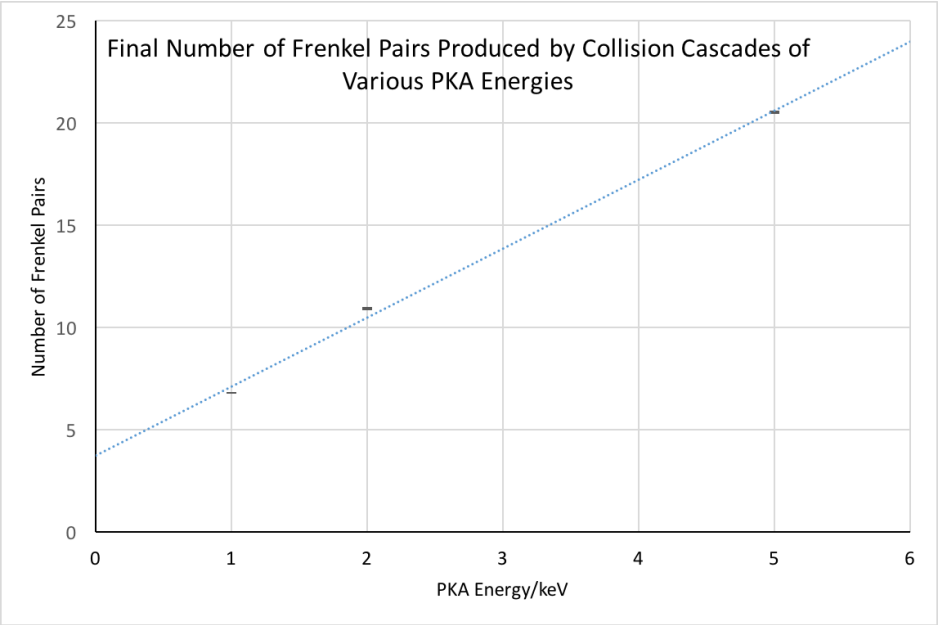

Figure 4.2: Final number of Frenkel pairs produced by collision cascades in $FeCr_{10\ at.\%}$ with PKAs of energies 1 keV (5553 simulations), 2 keV (5832 simulations), and 5 keV (5825 simulations) The equation of the line drawn, for PKA energy, E and Frenkel pair count, F, is $F = 3.3715E + 3.7492$. Data taken from table 4.2.

4.1.2 Temperature

We compared 1 keV cascades simulated at 500 Kelvin to those conducted at 0 Kelvin, and these data sets are shown in figure 4.5. For the latter, the final defect statistics may be found in tables 4.4 and 4.5 as part of section 4.1.3[3]. In the initial stages of the two sets of cascade data, the hotter systems average a greater number of Frenkel pairs, but after 2.75 ps, they fall below the low temperature systems. Additionally, while negligible difference is seen after minimising the 0 Kelvin results, a small, but statistically significant fall in Frenkel pairs is seen after the 500 Kelvin systems are relaxed. A much larger loss of lone interstitials to split-interstitials is seen, reducing the difference between the minimised 500 Kelvin and its 0 Kelvin counterpart. Likewise, unlike in the 0 Kelvin results, chromium is over-represented in defects at 500 Kelvin, but relaxing these systems results in its under-representation, more in-line with the 0 Kelvin data, see figures 4.3 and 4.7. Similarly, after minimisation, the relative rates of occurrence for FeCr and CrCr split-interstitials in the 500 Kelvin simulations resemble

[3]where a description of how this data was generated may also be found.

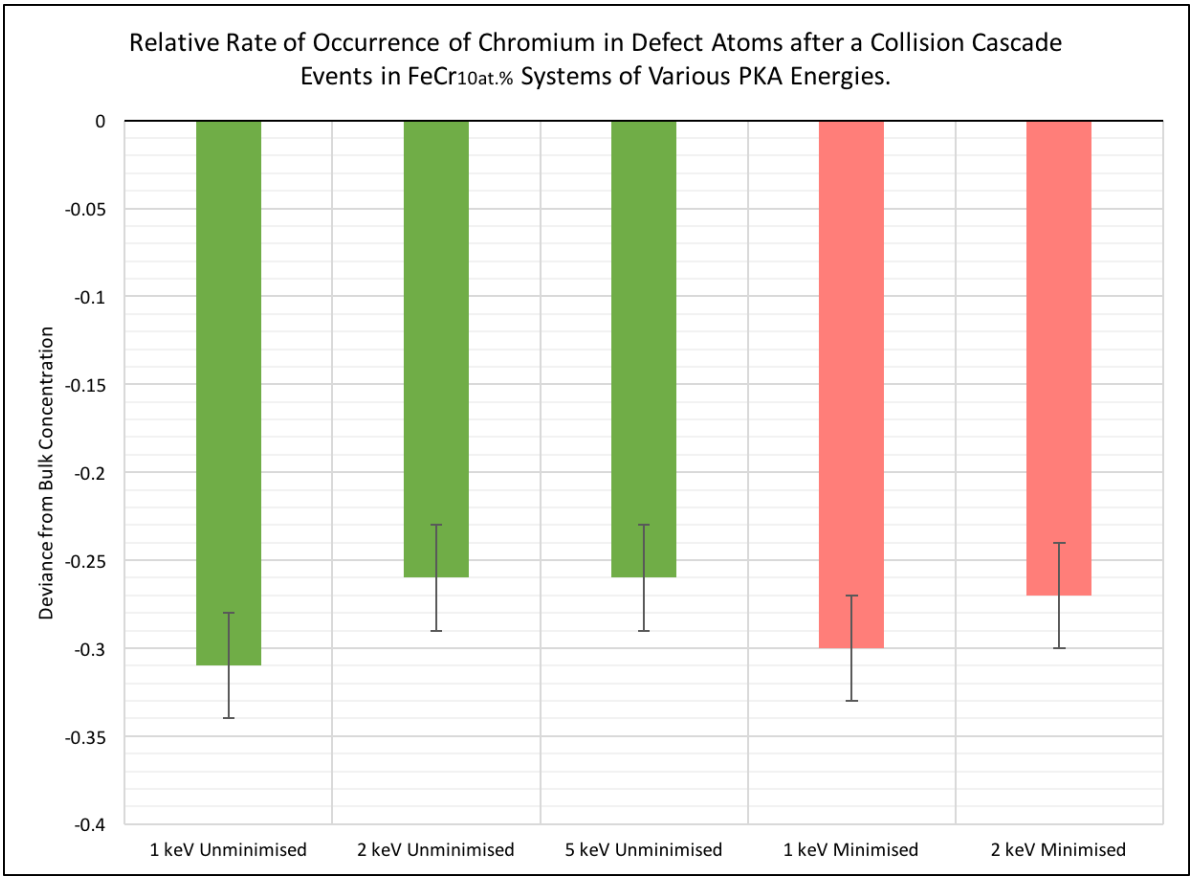

Figure 4.3: Relative rate of occurrence of chromium atoms in defects in $FeCr_{10\ at.\%}$ systems, following collision cascades of various PKA energies, calculated by dividing the percentage of defect atoms that were chromium by the bulk concentration (see tables 4.2 and 4.3), and then subtracting one from the result. Thus, positive values indicate a higher fraction of chromium in defect atoms than the bulk, and negative values indicate the converse. Given the high CPU hour cost associated with the L-BFGS-B/CG minimisation for larger systems, no minimised results appear for the 5 keV PKA simulations.

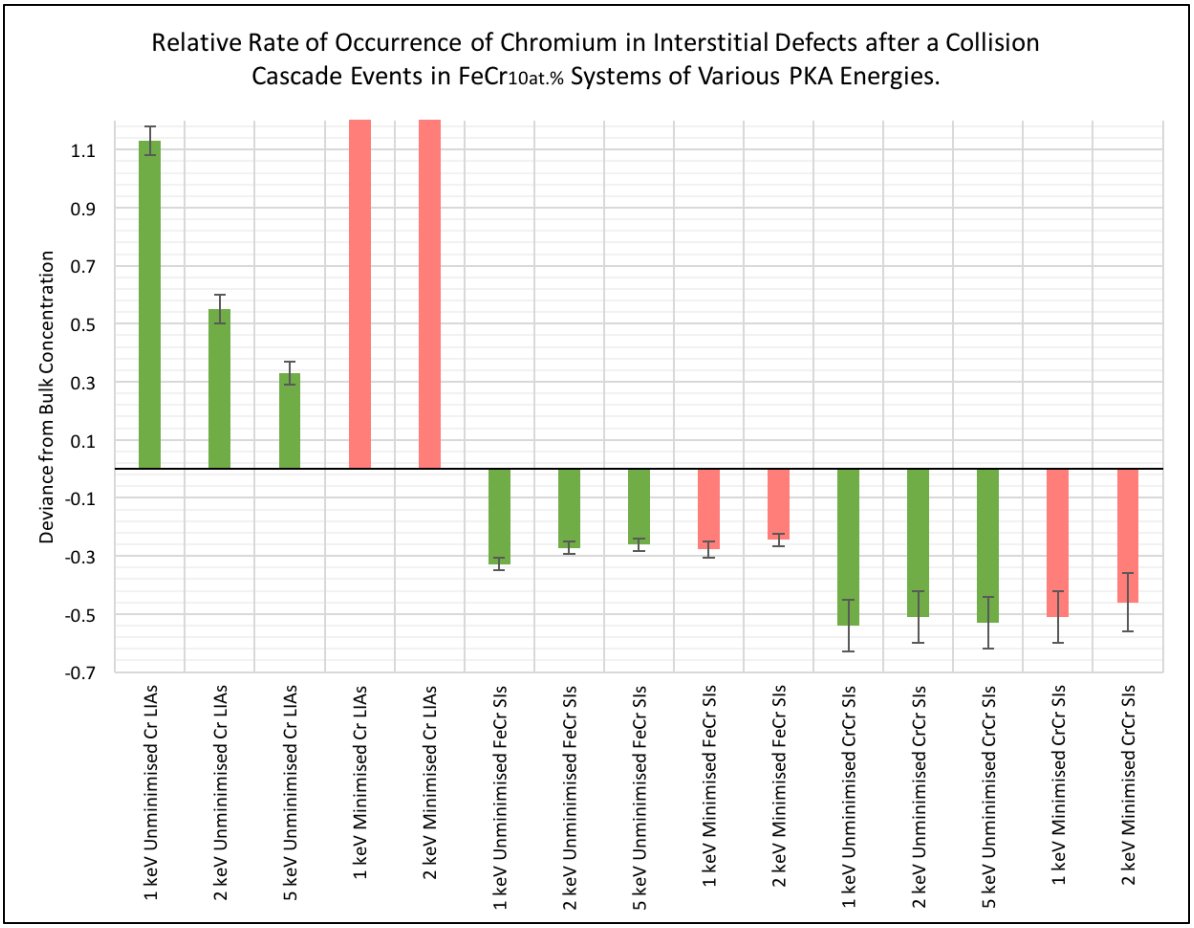

Figure 4.4: Relative rate of occurrence of chromium in interstitials in $FeCr_{10\ at.\%}$ systems, following collision cascades of various PKA energies, calculated by dividing the defect percentages found in tables 4.2 and 4.3 by the relevant reference value in table 4.1, and then subtracting one from the result. Thus, positive values indicate a higher fraction of chromium in defect atoms than the bulk, and negative values indicate the converse. The values of the Cr LIAs columns for the minimised 1 keV and 2 keV results are 5.49±0.03 and 5.16±0.13, and the y-axis is deliberately truncated to avoid them dwarfing the other results. Given the high CPU hour cost associated with the L-BFGS-B/CG minimisation for larger systems, no minimised results appear for the 5 keV PKA simulations.

their 0 Kelvin counterparts, see figures 4.4 and 4.8. Although lone chromium interstitials are over-represented in both sets of data, the effect is much more pronounced in the low temperature systems.

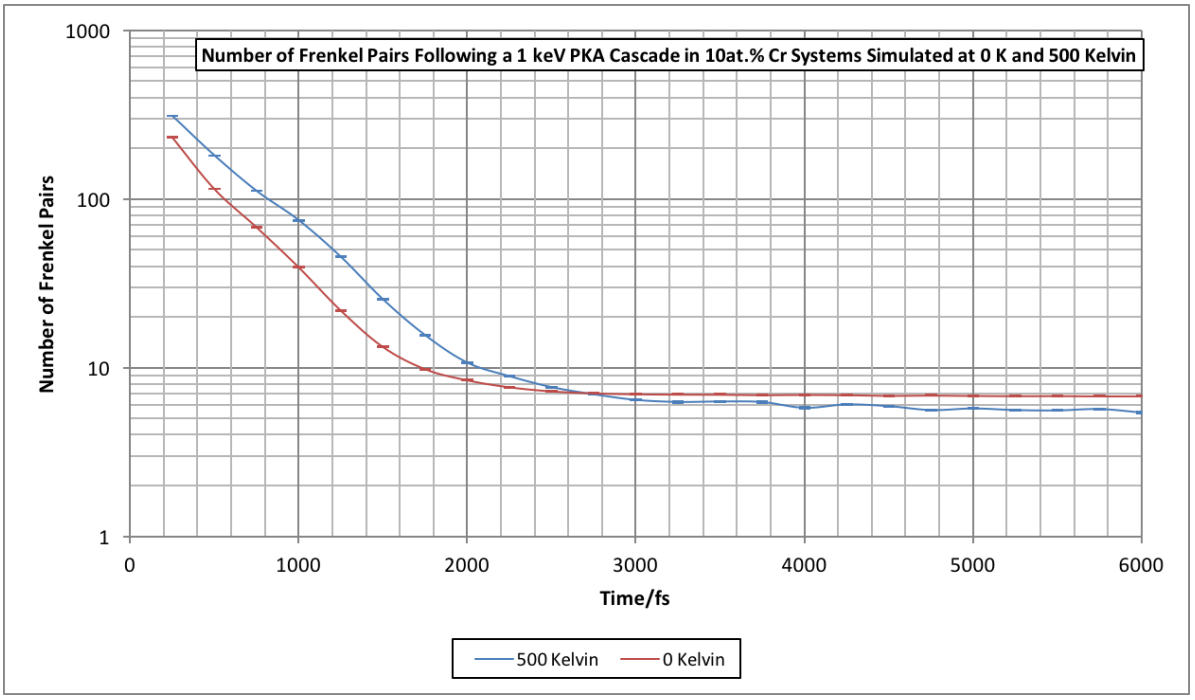

Figure 4.5: Comparison between the evolution of one 1 keV PKA cascades simulated in 54 thousand $FeCr_{10\ at.\%}$ atoms at 0 and 500 Kelvin (2160 and 4320 simulations, respectively). Please note that the number of Frenkel pairs is presented on a logarithmic axis.

4.1.3 Bulk Chromium Concentration

Our investigation into the effects of varying chromium concentration was conducted at 500 Kelvin with 1 keV cascades, thermalising the lattices prior to the cascade and maintaining a Berendsen thermostat throughout. Ten sets of 108 PKA vectors are used. For the three non-zero concentrations of chromium considered, $FeCr_{1\ at.\%}$, $FeCr_{5\ at.\%}$, and $FeCr_{10\ at.\%}$, 40, 20, and 40 unique lattices of 54,000 atoms were generated respectively. Each set of PKA vectors would be paired with a lattice on rotation, such that PKA vector set 1 would be used for lattices 1, 11, 21, 31, etc. In the pure iron simulations, one lattice was used with each of the PKA vector sets, as there was no alloying element to randomly distribute.

Thus, the total number of simulations performed in each system type, in ascending order of chromium concentration (including 0 at.%), were 1080, 4320, 2160, and 4320, with the lattice parameters of 2.855 Å, 2.856 Å, 2.858 Å, and 2.863 Å, respectively.

4.1.3.1 Unminimised and L-BFGS-B/CG Minimised Results

As is seen in figure 4.6, the evolution of the number of Frenkel pairs is essentially indistinguishable, and there is no statistically significant difference between the number of Frenkel pairs in the final lattices, shown in tables 4.4 and 4.5. A major difference that does exist, is the distribution of chromium in interstitial atoms, and the manner in which it differs after relaxation. In these results, there is a trend for chromium atoms to appear in interstitial defects at a higher rate than in the bulk, and this is increasingly evident at low concentration, see figure 4.7. Upon the minimisation of these systems however, this trend is lost – not only do the results no longer have any statistically significant trend, but they have also moved to an under-representation of chromium in defects. This is more similar to the results in section 4.1.1.

The error bars on the CrCr split-interstitials, see figure 4.8, are too large to draw any conclusions regarding whether they are under-represented in the same way as in section 4.1.1, except for the $FeCr_{10\ at.\%}$, where this does appear to be so. The FeCr split-interstitials follow the same trend as the overall relative rate of occurrence of chromium in defect atoms, in that they are over-represented in inverse proportion to bulk chromium concentration before minimisation, and under-represented with no apparent trend after minimisation. Lone chromium interstitials are also over-represented before minimisation in inverse proportion to bulk concentration. Minimising these lattices increases this over-representation, but the correlation is no longer seen – with the results for $FeCr_{5\ at.\%}$ being a clear outlier.

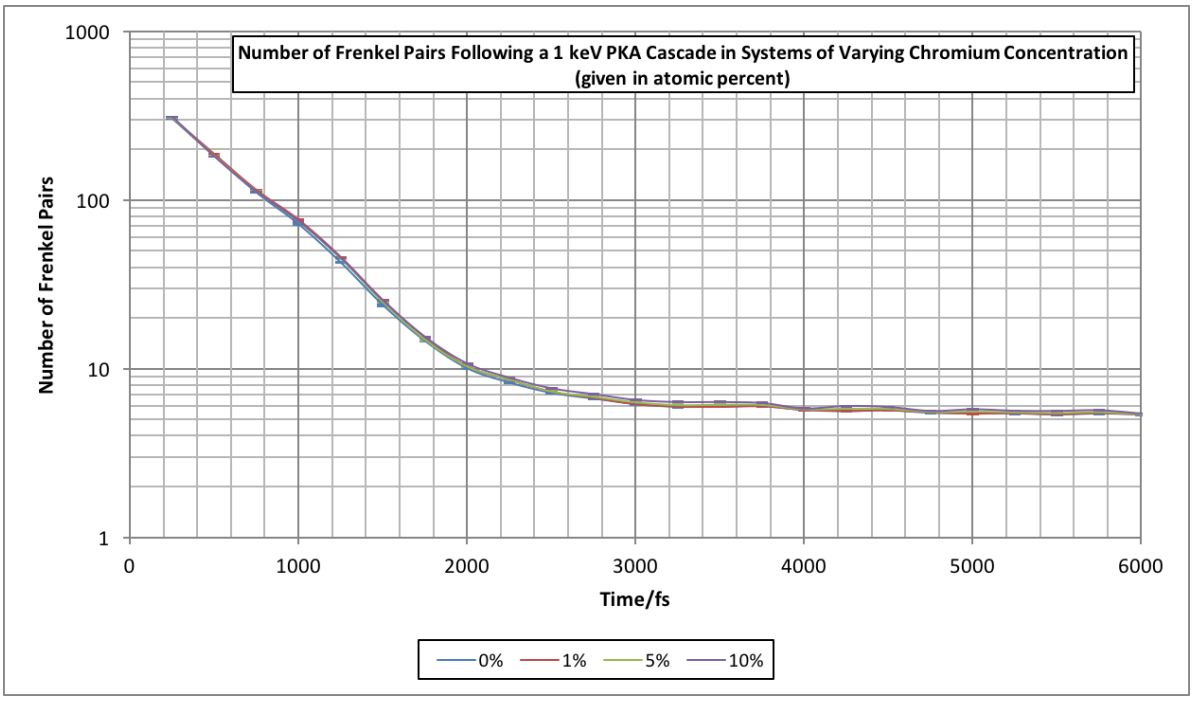

Figure 4.6: Defect evolution over 6 ps from 1 keV PKA cascades simulated at 500 Kelvin in systems of 54 thousand atoms at various ratios of iron and chromium. Please note that the number of Frenkel pairs is presented on a logarithmic axis.

Table 4.4: Defect statistics from 1 keV PKA cascades simulated for 6 ps at 500 Kelvin in systems of 54 thousand atoms at various ratios of iron and chromium (no post-cascade lattice minimisation).

Atomic Percentage Chromium	Defect atoms of which Cr (%)	Lone Interstitials	Split-Interstitials	Total Frenkel Pairs
0%	*N/A*	1.49±0.04	3.88±0.05	5.37±0.06
1%	1.55±0.18	1.48±0.02	3.87±0.03	5.35±0.03
5%	6.8±0.8	1.54±0.04	3.82±0.05	5.36±0.07
10%	10.7±0.5	1.65±0.02	3.79±0.03	5.42±0.04
Atomic Percentage Chromium	LIAs of which Cr (%)	SIs of which FeFe (%)	SIs of which FeCr (%)	SIs of which CrCr (%)
1%	2.0±0.2	97.1±0.3	2.9±0.3	None recorded
5%	8.2±0.6	87.7±0.7	12.1±0.7	0.21±0.10
10%	13.3±0.5	81.1±0.6	19.4±0.6	0.51±0.11

Table 4.5: Defect statistics from 1 keV PKA cascades simulated for 6 ps at 500 Kelvin in systems of 54 thousand atoms at various ratios of iron and chromium (with post-cascade L-BFGS-B/CG lattice minimisation).

Atomic Percentage Chromium	Defect atoms of which Cr (%)	Lone Interstitials	Split-Interstitials	Total Frenkel Pairs
0%	*N/A*	0.58±0.03	4.54±0.05	5.12±0.06
1%	0.80±0.14	0.613±0.014	4.47±0.03	5.08±0.03
5%	4.5±0.4	0.70±0.02	4.42±0.04	5.11±0.04
10%	8.1±0.4	0.835±0.016	4.32±0.03	5.15±0.03
Atomic Percentage Chromium	LIAs of which Cr (%)	SIs of which FeFe (%)	SIs of which FeCr (%)	SIs of which CrCr (%)
1%	2.1±0.2	98.4±0.19	1.61±0.19	0.005±0.011
5%	9.2±0.6	91.9±0.5	7.8±0.5	0.28±0.11
10%	14.5±0.5	85.7±0.5	13.6±0.5	0.69±0.13

4.1.3.2 Post-Damped MD Analysis

Being concerned about the extent to which the computationally fast relaxation of the lattices changes our apparent results, we elected to examine the systems after they were relaxed via damped MD (see section 2.3), and this data can be found in table 4.6. With damped MD being so much more computationally expensive, we set our force tolerance at 0.1 eV/Å, rather than the 0.01 eV/Å used during L-BFGS-B/CG minimisation.

Similar to the previous minimised results, we a see loss of lone interstitials to split-interstitials, with no statistically significant difference between those two sets. Likewise, the same small fall in the number of Frenkel pairs following minimisation is seen. The results following damped MD have an overall appearance rate of chromium in defects that is akin to the unminimised results (see figure 4.9), and as such, we do not observe the dramatic reconfiguration seen after L-BFGS-B/CG minimisation. Damped MD has not made a statistically significant difference to the over-representation of chromium seen in the $FeCr_{1\ at.\%}$ and $FeCr_{5\ at.\%}$ systems, but an increase is seen for the $FeCr_{10\ at.\%}$ systems.

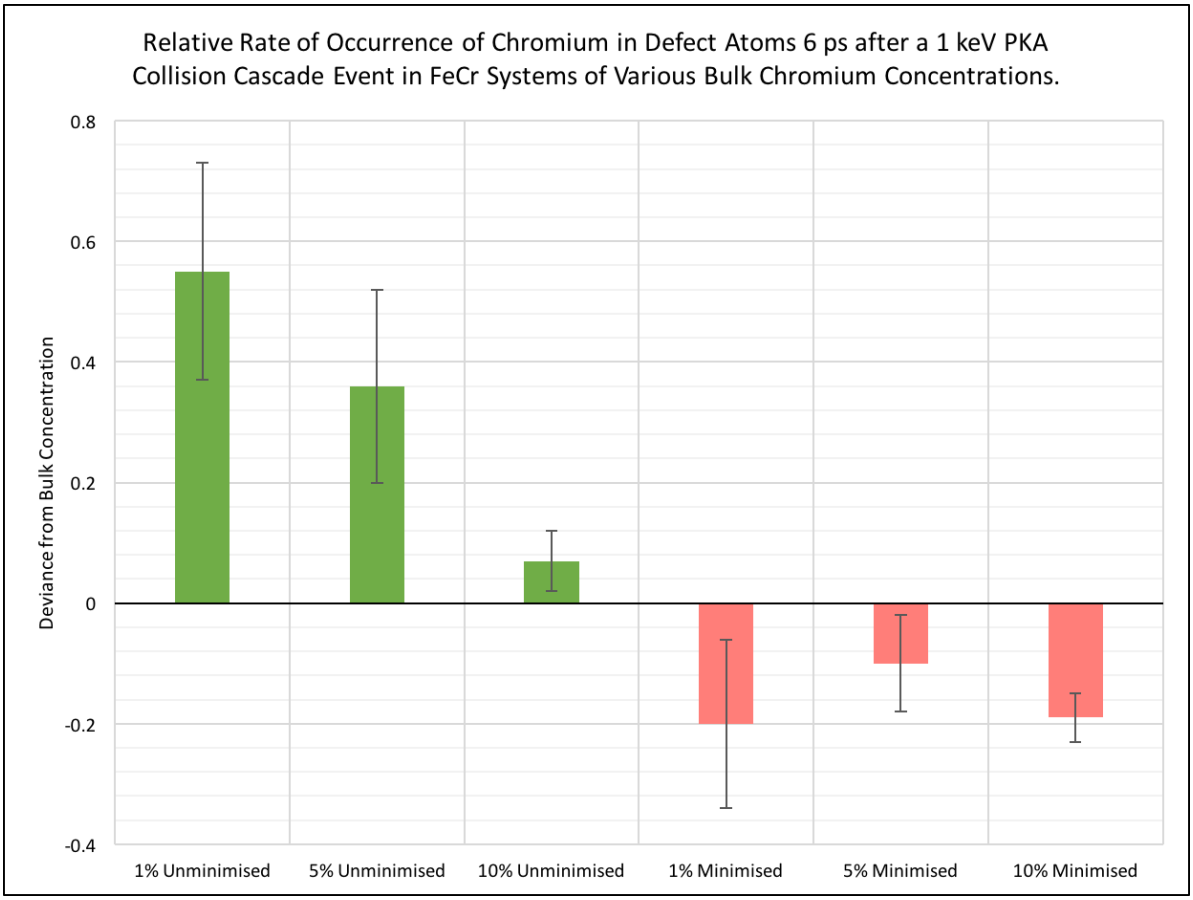

Figure 4.7: Relative rate of occurrence of chromium atoms in defects in systems of various bulk concentration, following 1 keV collision cascades, calculated by dividing the percentage of defect atoms that were chromium by the bulk concentration (see tables 4.4 and 4.5), and then subtracting one from the result. Thus, positive values indicate a higher fraction of chromium in defect atoms than the bulk, and negative values indicate the converse. Bulk concentrations are given in atomic percent. See table 4.1 for reference values.

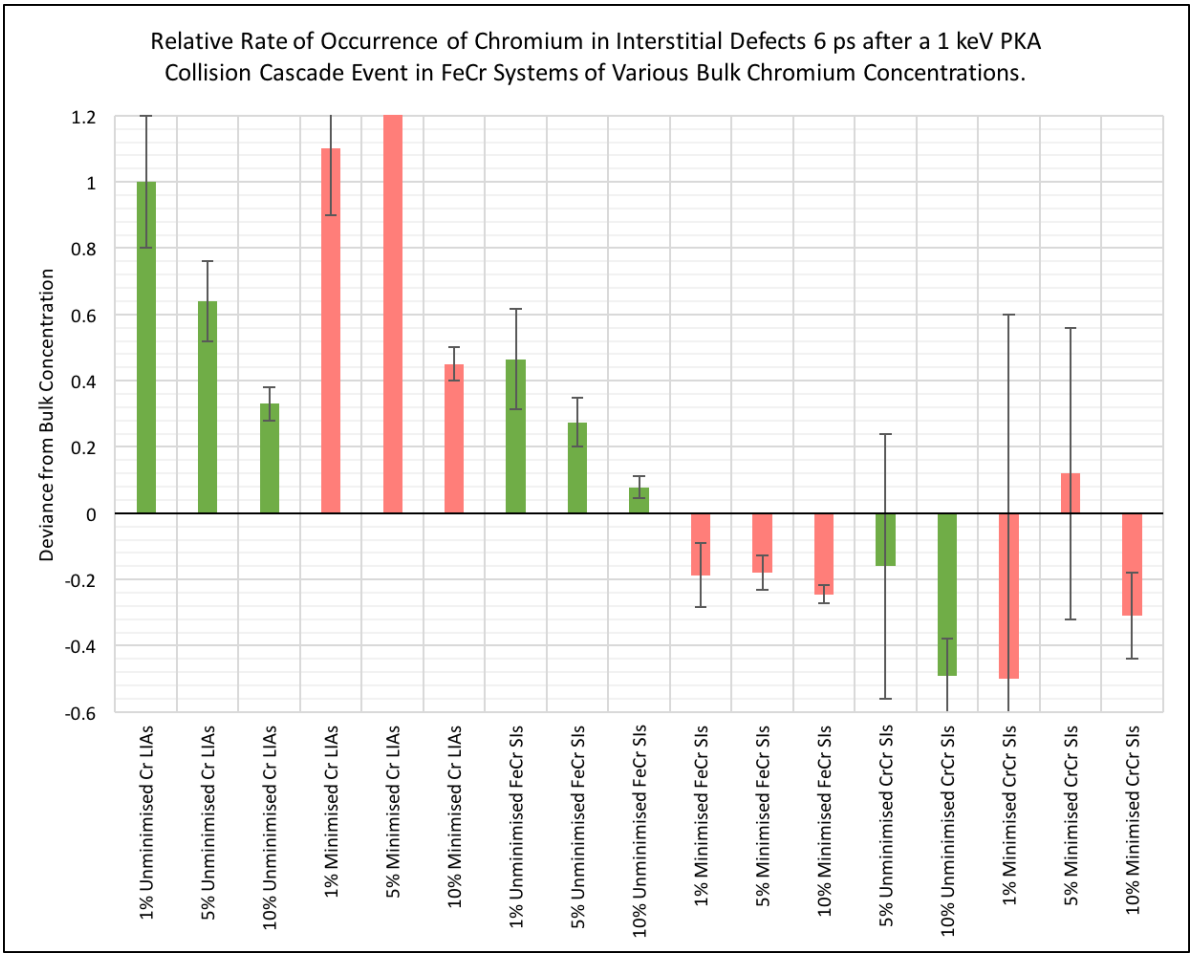

Figure 4.8: Relative rate of occurrence of chromium in interstitial atoms in systems of various bulk concentration, following 1 keV collision cascades, calculated by dividing the defect percentages from tables 4.4 and 4.5 by the relevant reference value in talbe 4.1, and then subtracting one from the result. Thus, positive values indicate a higher fraction of chromium in defect atoms than the bulk, and negative values indicate the converse. Bulk concentrations are given in atomic percent. See table 4.1 for reference values. Note that the y-axis is deliberately cut off at 1.2 such that the "5% Minimised Cr LIAs" column, 3.6 ± 0.3, does not dwarf the others.

Table 4.6: Defect statistics from 1 keV PKA cascades simulated for 6 ps at 500 Kelvin in systems of 54 thousand atoms at various ratios of iron and chromium (with damped MD post-cascade lattice minimisation).

Atomic Percentage Chromium	Defect atoms of which Cr (%)	Lone Interstitials	Split-Interstitials	Total Frenkel Pairs
0%	*N/A*	0.56±0.03	4.50±0.05	5.07±0.07
1%	1.61±0.19	0.603±0.013	4.42±0.03	5.02±0.03
5%	7.5±0.6	0.75±0.02	4.29±0.04	5.04±0.04
10%	12.0±0.5	0.934±0.016	4.13±0.03	5.06±0.03
Atomic Percentage Chromium	LIAs of which Cr (%)	SIs of which FeFe (%)	SIs of which FeCr (%)	SIs of which CrCr (%)
1%	5.0±0.3	97.3±0.2	2.7±0.2	0.011±0.016
5%	17.8±0.8	87.0±0.7	12.7±0.7	0.27±0.11
10%	23.4±0.6	79.3±0.6	20.1±0.6	0.64±0.12

Regarding surviving lone interstitial atoms, the very large chromium over-representations seen after L-BFGS-B/CG minimisation are not seen following damped MD, but the relative sizes of the three system types' results are in approximately the same proportions. As seen in figure 4.10, the switch from over-representation to under-representation of FeCr split-interstitials seen following L-BFGS-B/CG minimisation does not occur after damped MD and the difference between the latter and the results prior to minimisation is not statistically significant. CrCr split-interstitials in $FeCr_{10\ at.\%}$ are under-represented, as they were in the original minimisation, although we do not have sufficiently good statistics to comment on the other bulk concentrations – see figure 4.11.

4.1.4 Discussion

From the results of our simulations, we see that after the initial kinetic energy of the PKA, the most significant factor in the total number of defects introduced to a lattice is the system's temperature. While more defects are produced in the early stage of the cascades at 500 Kelvin in $FeCr_{10\ at.\%}$, a greater rate of recombination is seen in these systems during the ballistic

phase, leading to a lower final number of Frenkel pairs, consistent with the increased mobility of defect objects at higher temperature. Furthermore, temperature is seen to be relevant to the representation of chromium in defect atoms. The results conducted at 500 Kelvin in $FeCr_{10\ at.\%}$ are suggestive of a small over-representation of chromium before minimisation (although more simulations would have to be performed for statistical confidence), and while after minimisation an under-representation is seen instead, it is still lesser than that seen in the 0 Kelvin simulations.

The variation of bulk chromium concentration does not have an impact on the number of Frenkel pairs produced by 1 keV PKA cascades, but our results would seem to show that chromium atoms are more readily taken from their lattice sites than iron at 500 Kelvin, and while relaxing the lattices sees a general under-representation of chromium, lone chromium interstitials remain consistently over-represented. This over-representation is negatively correlated with both PKA energy and bulk chromium concentration. Given the desire to avoid chromium segregation in a nuclear reactor, we would therefore recommend against the use of low chromium concentration materials.

The results of our damped MD suggest that the under-representation of chromium that appears after minimisation is an artefact of the L-BFGS-B/CG method. Being more robust, the damped MD results should be more representative of a settled system.

With regard to cascade morphology, as is seen in figures 4.12 to 4.15, the region around the initial position of the PKA experiences a rapid displacement of the surrounding atoms. The centre of this region is left with many lattice vacancies, while at the greatest extent of the plume of transient damage, interstitials are left. Additionally, damage is transmitted outwards by replacement collision sequences, leaving interstitial defects further out from the central cascade region. In the highest PKA energy cascades, we also see evidence of cluster formation, for example in figure 4.14.

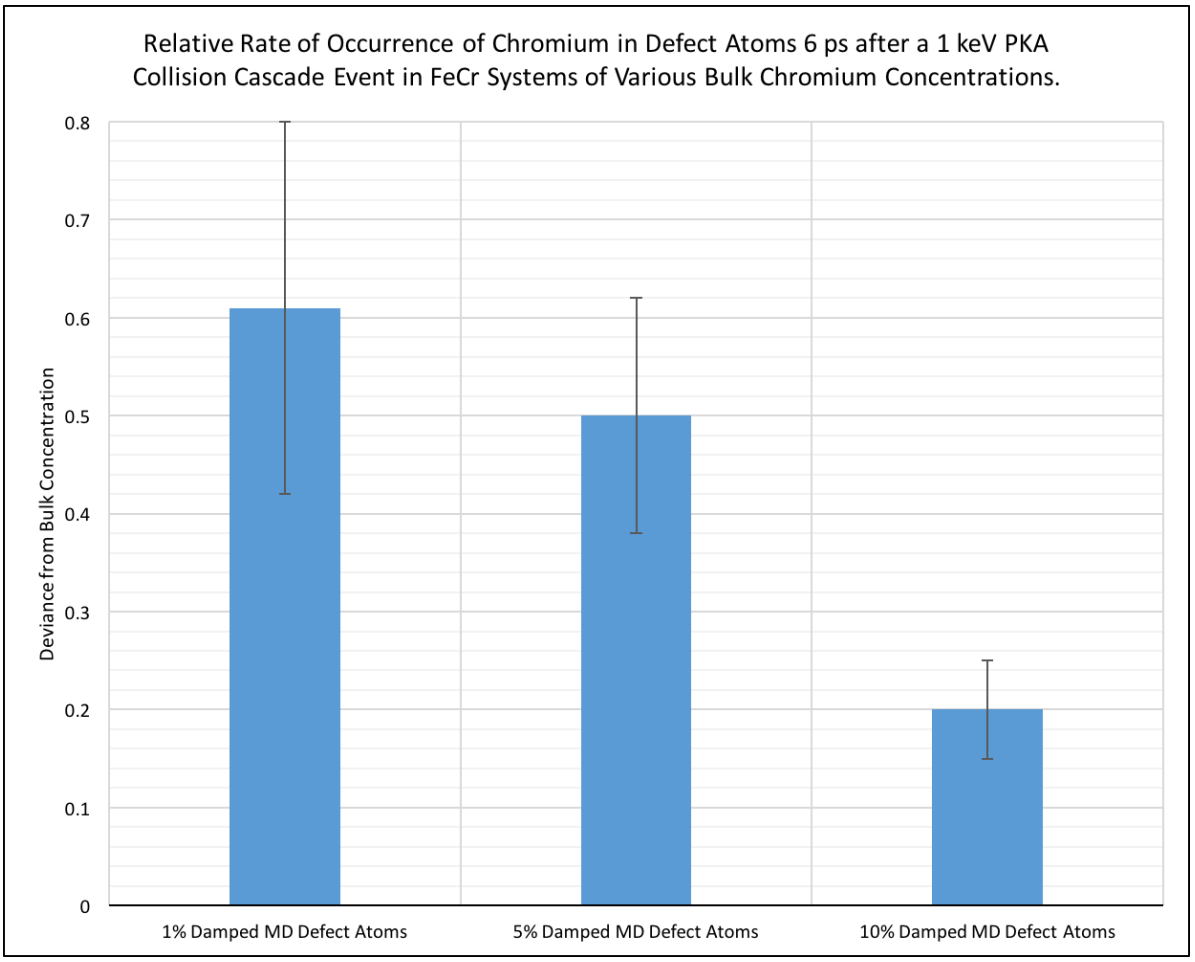

Figure 4.9: Relative rate of occurrence of chromium atoms in defects in systems of various bulk concentration, following 1 keV collision cascades, with damped MD applied afterwards, calculated by dividing the percentage of defect atoms that were chromium by the bulk concentration (see tables 4.4 and 4.5), and then subtracting one from the result. Thus, positive values indicate a higher fraction of chromium in defect atoms than the bulk, and negative values indicate the converse. Bulk concentrations are given in atomic percent. See table 4.1 for reference values.

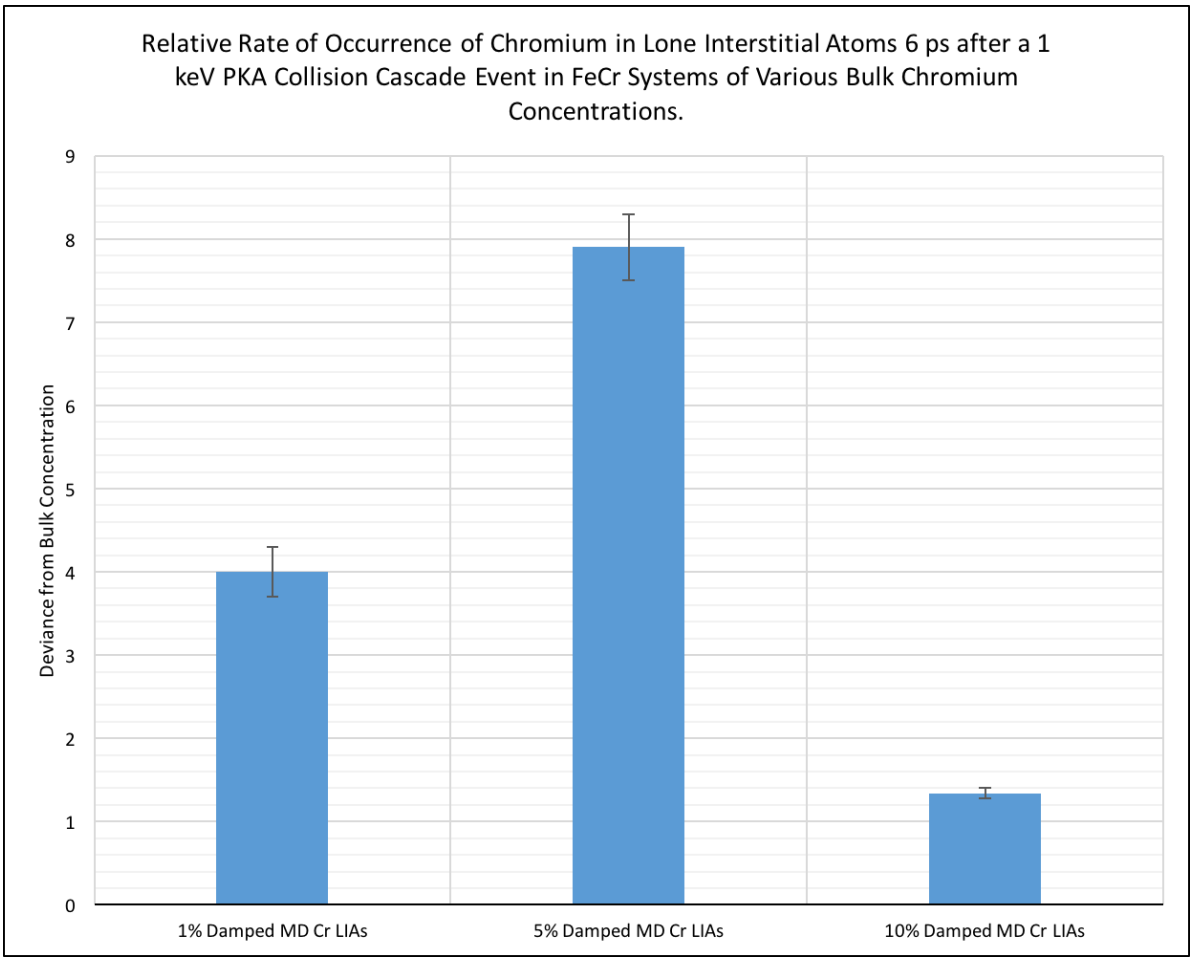

Figure 4.10: Relative rate of occurrence of chromium in lone interstitial atom in systems of various bulk concentration, following 1 keV collision cascades, with damped MD applied afterwards, calculated by dividing the percentage of defect atoms that were chromium by the bulk concentration (see tables 4.4 and 4.5), and then subtracting one from the result. Thus, positive values indicate a higher fraction of chromium in defect atoms than the bulk, and negative values indicate the converse. Bulk concentrations are given in atomic percent. See table 4.1 for reference values.

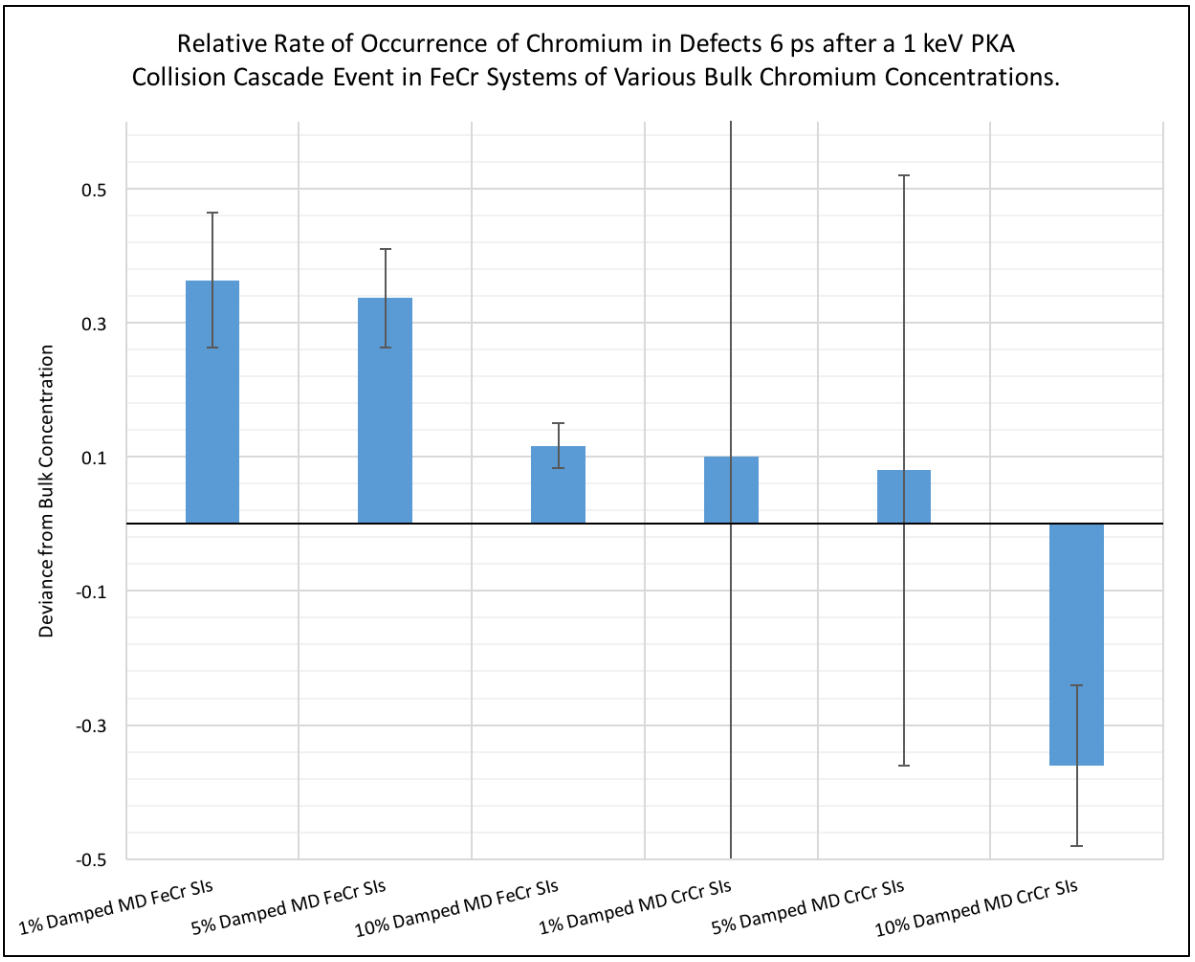

Figure 4.11: Relative rate of occurrence of FeCr and CrCr split interstitial atom in systems of various bulk concentration, following 1 keV collision cascades, with damped MD applied afterwards, calculated by dividing the percentage of defect atoms that were chromium by the bulk concentration (see tables 4.4 and 4.5), and then subtracting one from the result. Thus, positive values indicate a higher fraction of chromium in defect atoms than the bulk, and negative values indicate the converse. Bulk concentrations are given in atomic percent. See table 4.1 for reference values.

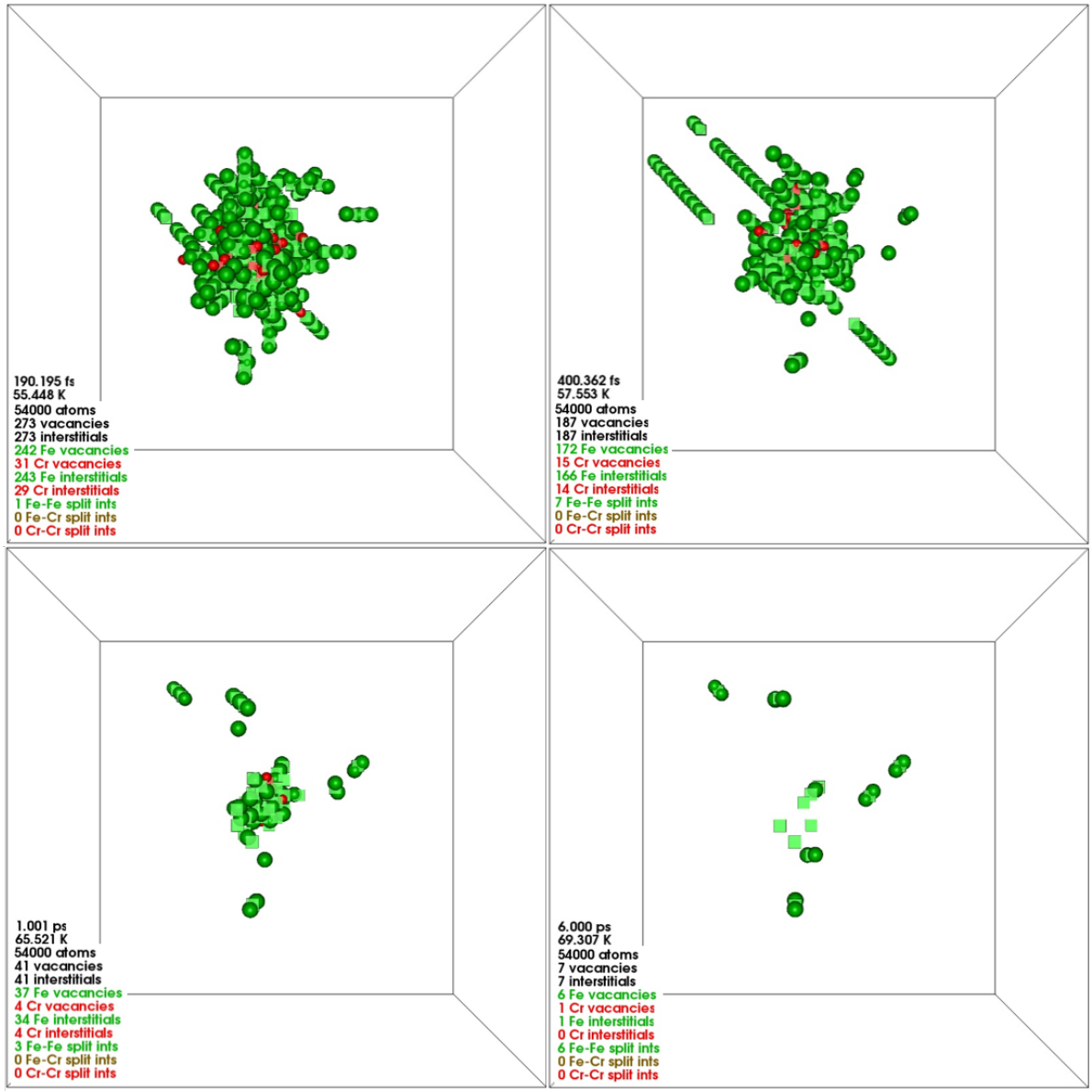

Figure 4.12: Snapshots from a 1 keV PKA collision cascade conducted at 0 Kelvin in $FeCr_{10\ at.\%}$. This example is typical of the results described in section 4.1.1. Interstitial atoms are visualised as spheres and vacant lattice sites are represented as cubes, with on-lattice atoms being hidden. The cascade event originates at the centre of the lattice and displaces many atoms in the surrounding volume. Most Frenkel pairs recombine within a few picoseconds, but some damage remains, with vacancies close to the centre of the event and interstitials found around the maximum extent of the damage plume.

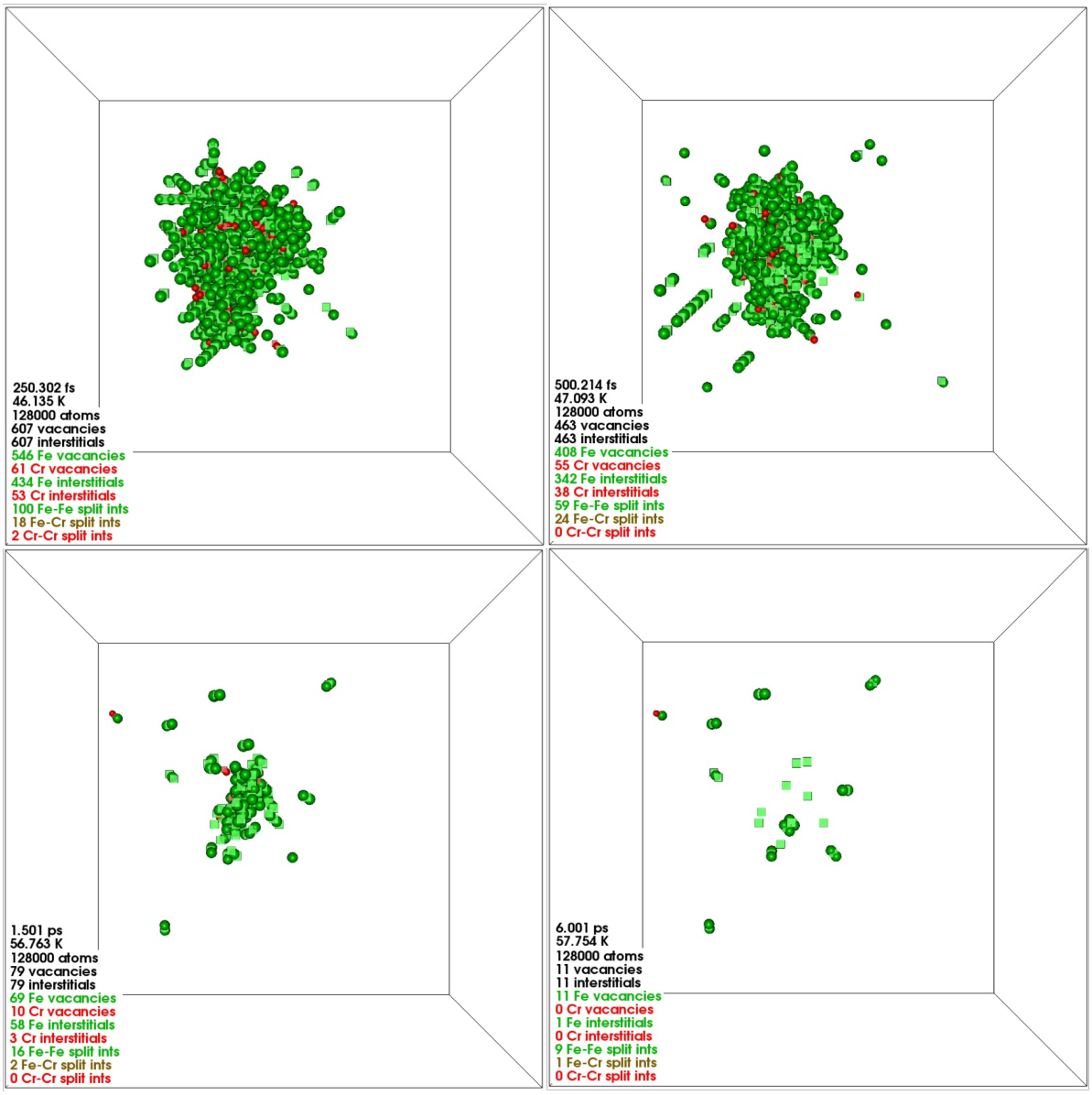

Figure 4.13: Snapshots from a 2 keV PKA collision cascade conducted at 0 Kelvin in $FeCr_{10\ at.\%}$. This example is typical of the results described in section 4.1.1. Interstitial atoms are visualised as spheres and vacant lattice sites are represented as cubes, with on-lattice atoms being hidden. The cascade event originates at the centre of the lattice and displaces many atoms in the surrounding volume. Most Frenkel pairs recombine within a few picoseconds, but some damage remains, with vacancies close to the centre of the event and interstitials found around the maximum extent of the damage plume.

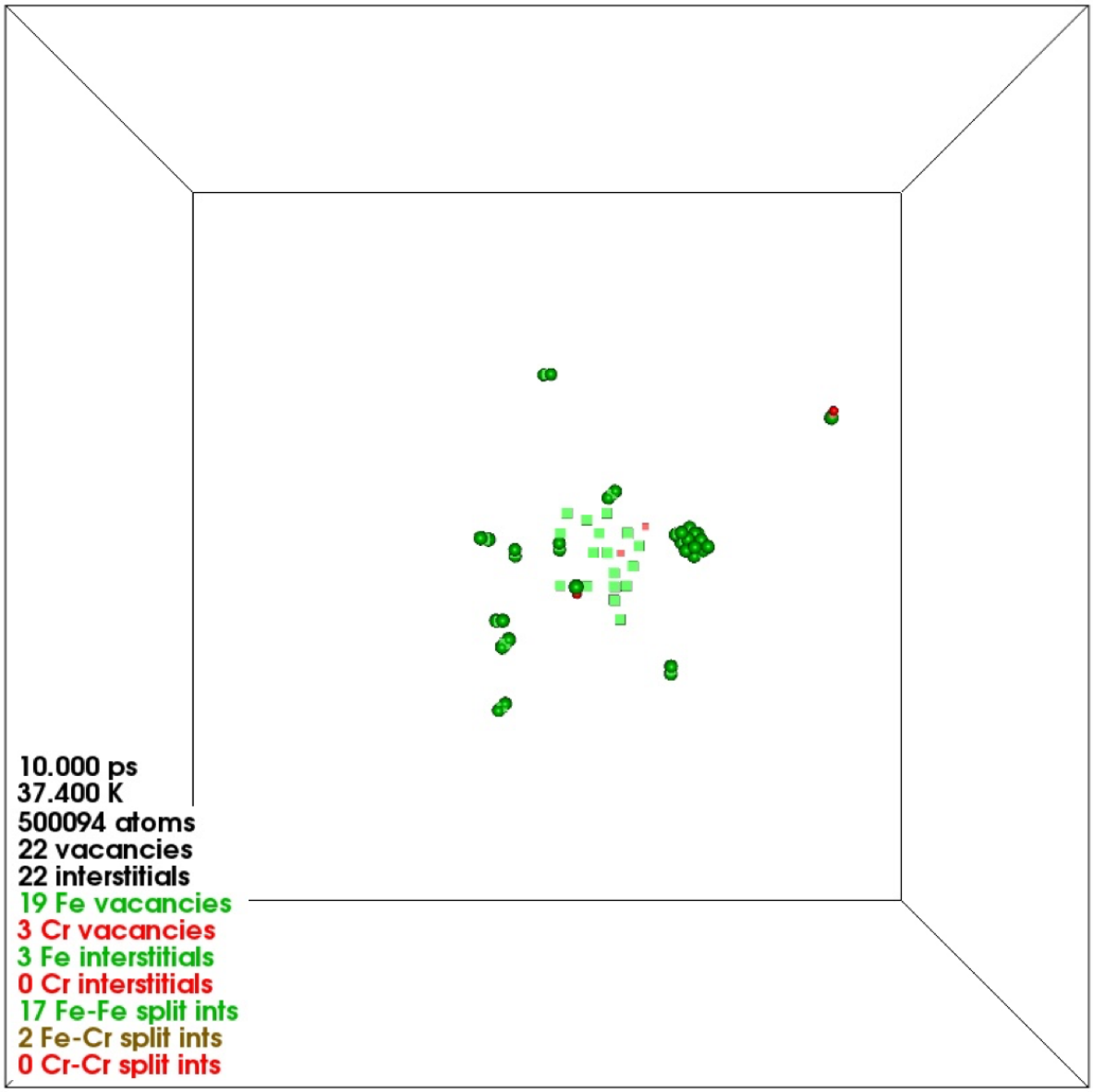

Figure 4.14: Final snapshot from a 5 keV PKA collision cascade conducted at 0 Kelvin in $FeCr_{10\ at.\%}$. This example is typical of the results described in section 4.1.1. Interstitial atoms are visualised as spheres and vacant lattice sites are represented as cubes, with on-lattice atoms being hidden. The cascade event originates at the centre of the lattice and displaces many atoms in the surrounding volume. Most Frenkel pairs recombine within a few picoseconds, but some damage remains, with vacancies close to the centre of the event and interstitials found around the maximum extent of the damage plume.

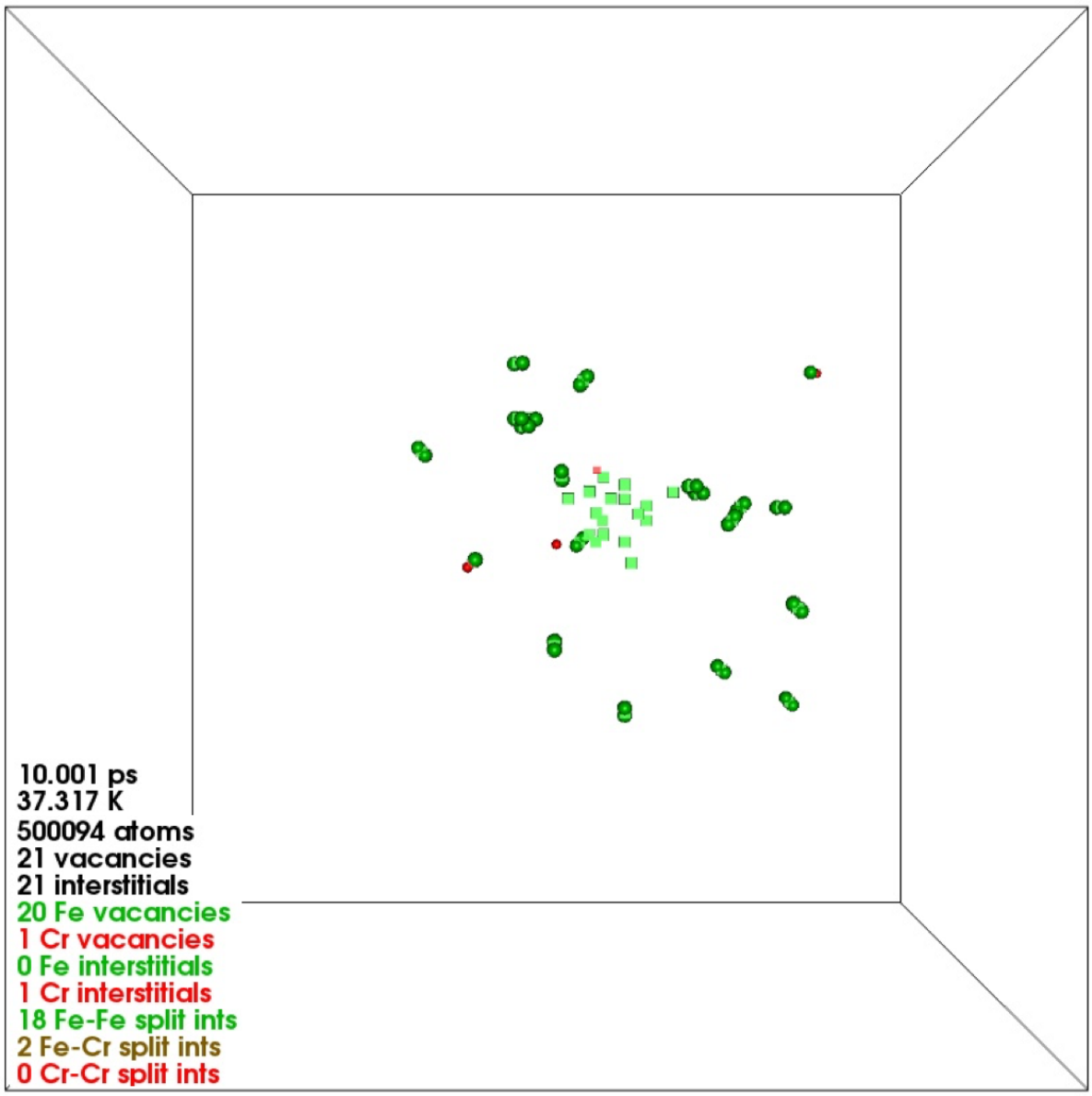

Figure 4.15: Final snapshot from a 5 keV PKA collision cascade conducted at 0 Kelvin in $FeCr_{10\ at.\%}$. This example is typical of the results described in section 4.1.1. Interstitial atoms are visualised as spheres and vacant lattice sites are represented as cubes, with on-lattice atoms being hidden. The cascade event originates at the centre of the lattice and displaces many atoms in the surrounding volume. Most Frenkel pairs recombine within a few picoseconds, but some damage remains, with vacancies close to the centre of the event and interstitials found around the maximum extent of the damage plume.

4.2 Long Timescale Dynamics

4.2.1 Defect Mobility

To consider how the presence of chromium in our systems affects the migration of defects, we conducted a series of barrier searches in 2000 atom systems of pure iron and of $FeCr_{10\ at.\%}$. In the pure iron system, we created two modified systems, one containing a single vacant lattice site, and the other containing a single SIA. For the $FeCr_{10\ at.\%}$ systems, we create five systems with a vacancy, five systems with an FeFe SIA, and five systems with an FeCr SIA. In each of these systems, we conducted 5000 barrier searches, as per section 3.2.2.7. A far smaller diversity of barrier height is seen in the pure iron systems, with no chromium atoms to break the homogeneity of the surrounding environment, although the number of transitions found per search is larger in pure iron. Calculating how this translates to rates, by way of $\exp\left(\frac{-E}{k_B T}\right)$, disregarding prefactors, we find that their averages are higher (comparing vacancies to vacancies and SIs to SIs) in the $FeCr_{10\ at.\%}$, see table 4.7, and indeed, the lowest energy barriers are found in the $FeCr_{10\ at.\%}$ systems, which is suggestive of a greater defect mobility.

With regards to the specific SIA in $FeCr_{10\ at.\%}$, the FeCr SIA has a higher average rate than the FeFe SIA, and this may be a reflection of the higher defect formation energy of the former, see figure 2.4.

4.2.2 Recovery

To observe the recovery from radiation damage beyond the ballistic phase, we took a selection of post-cascade lattices, and in these we performed AKMC simulations. These lattices were taken from the 1 keV cascades in $FeCr_{10\ at.\%}$ found in section 4.1.1. The average number of Frenkel pairs in these systems was 6.78 ± 0.03 and so the systems selected for AKMC have Frenkel pair counts in the range 6 to 8. The barrier height threshold set for the basin method in these simulations was 0.5 eV. A summary of the simulations is seen in table 4.8,

Table 4.7: The average values of $\exp\left(\frac{-E}{k_B T}\right)$ from barrier searches of various defect types in pure iron and $FeCr_{10\text{ at.}\%}$.

Pure Iron	
Defect Type	$\left\langle \exp\left(\frac{-E}{k_B T}\right) \right\rangle$
Vacancy	0.99966 ± 0.00006
Split-Interstitial	0.999911 ± 0.000006
$FeCr_{10\text{ at.}\%}$	
Defect Type	$\left\langle \exp\left(\frac{-E}{k_B T}\right) \right\rangle$
Vacancy	0.99975 ± 0.00003
FeFe Split-Interstitial	0.999923 ± 0.000003
FeCr Split-Interstitial	0.999953 ± 0.000004

and snapshots are shown in figures 4.17 to 4.23. Two AKMC simulations were conducted in the second lattice selected (which is also the system seen in figure 4.12), and these are denoted system 2a and system 2b.

Within the computing time allotted to these simulations, only one system, 2b, experienced the complete recombination of all of its Frenkel pairs, doing so in 5.92 μs. Of the remaining six, half experience a net fall in Frenkel pairs, with the other having no net change. All of the systems undergo a fall in potential energy, implying they have evolved to more stable states. Moreover, the drop in potential energy is positively correlated with the number of Frenkel pairs recombined. As is seen in figure 4.16, there is a tenuous positive relationship between number of AKMC steps taken, number of Frenkel pairs recombined, and simulated time.

Aside from the annealing of defects, interstitial atoms also show a tendency to form clusters, although they are less mobile than unclustered split-interstitials, these structures do, in some cases, break up. Examples of interstitial atom cluster coalesion are seen in systems 2a, 2b, 3, 5, and 6. Additionally, in system 1, a cluster of vacancies, i.e. a small void, forms. In systems 2b and 6, vacancies are seen to align themselves in a straight line along adjacent lattice sites.

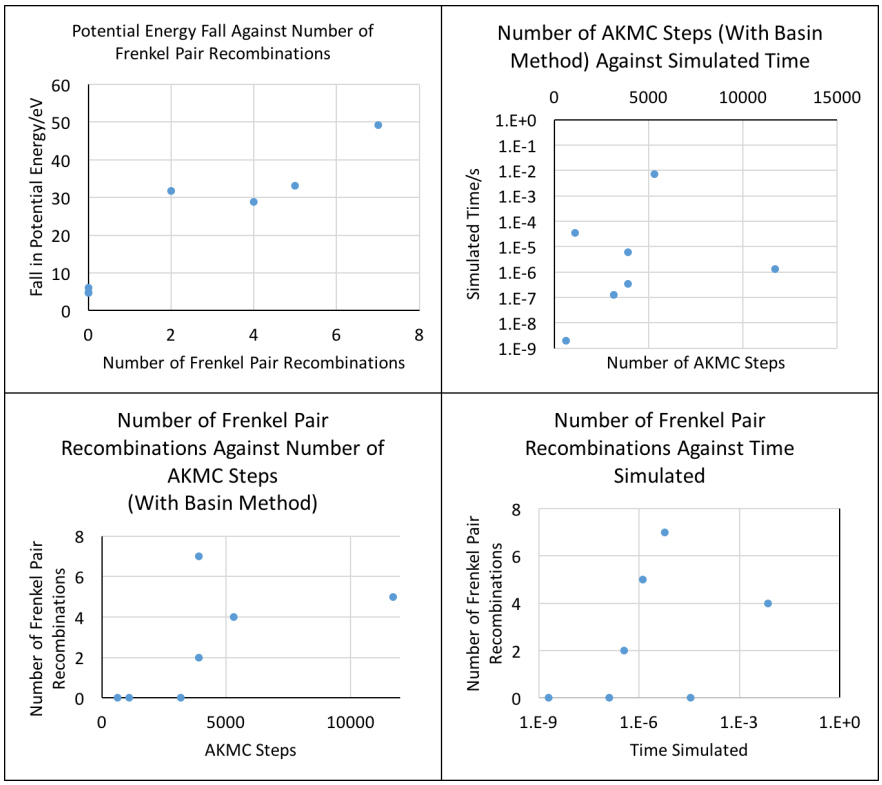

Figure 4.16: Relationship between changes in potential energy and number of Frenkel pairs to steps taken, and time simulated in seven AKMC simulations, see table 4.8.

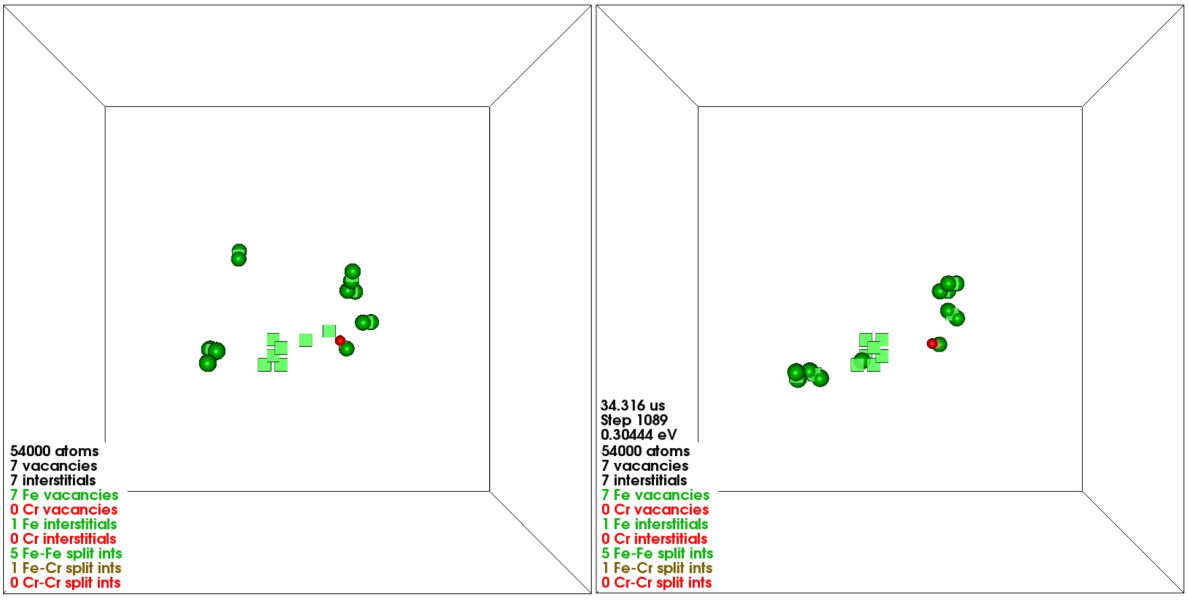

Figure 4.17: Visualisation of an AKMC simulation conducted in a BCC $FeCr_{10\ at.\%}$ system which has experienced a 1 keV PKA collision cascade (system 1). The initial lattice is shown on the right and the image on the left shows the system after 34.3 µs. In this system, the lattice vacancies are seen to cluster. One of the split-interstitials has recombined with a vacant site, but a split-vacancy has also formed, leaving the total Frenkel pair count at seven. Off lattice atoms are visualised as spheres, green for iron, red for chromium, and cubes represent vacancies.

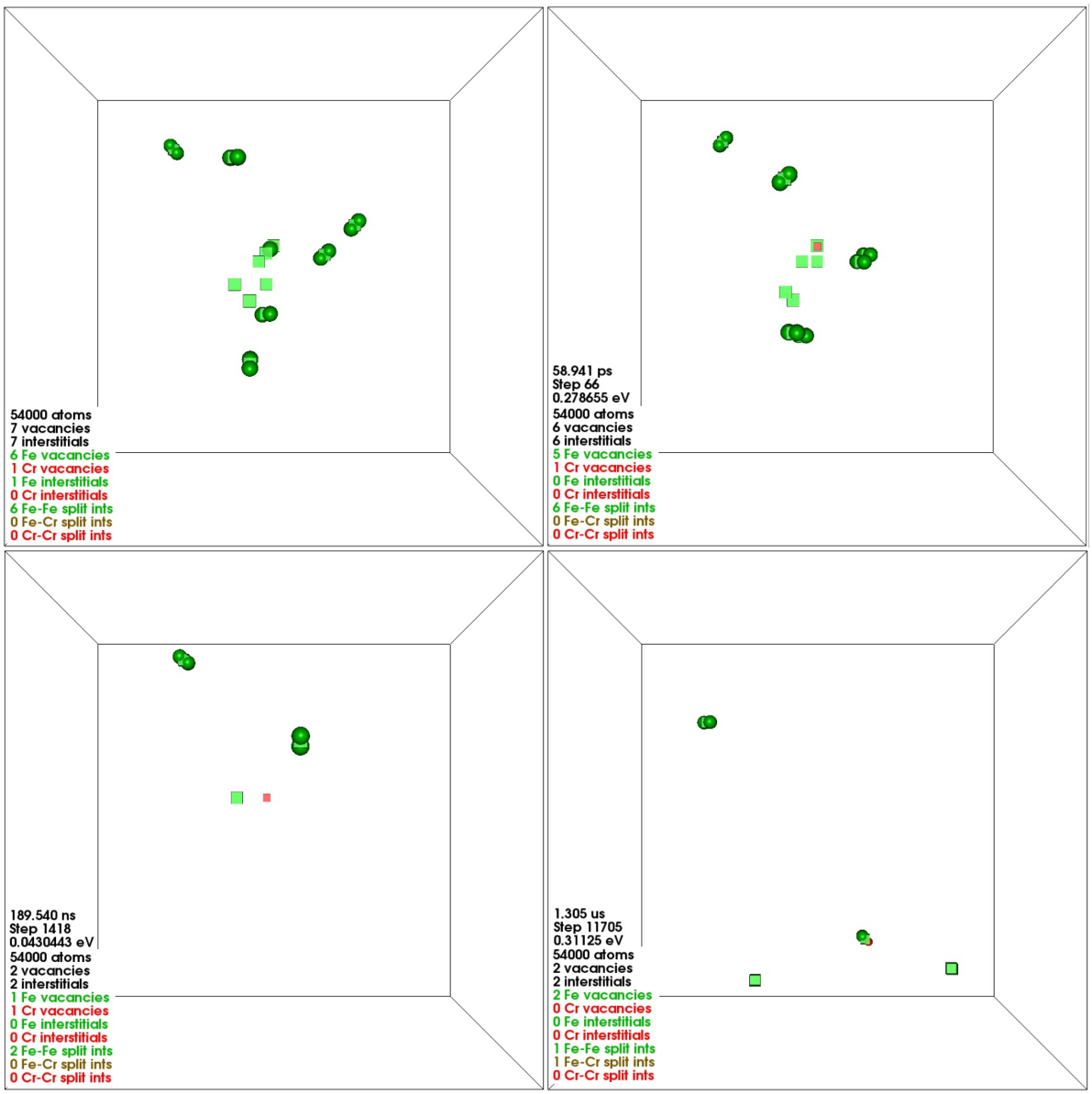

Figure 4.18: Visualisation of an AKMC simulation conducted in a BCC $FeCr_{10\ at.\%}$ system which has experienced a 1 keV PKA collision cascade (system 2a). The initial lattice is shown in the top-right image and snapshots of the simulation at 58.9 ps, 190 ns, and 1.31 µs are shown in the other images. Two examples of the clustering of interstitial defects are seen at 58.9 ps, but ultimately, these clusters break apart, and recombination with vacant sites occurs, leaving the system with five fewer Frenkel pairs by 190 ns. Between 190 ns and the 1.31 µs, no further recombination has occurred. Off lattice atoms are visualised as spheres, green for iron, red for chromium, and cubes represent vacancies.

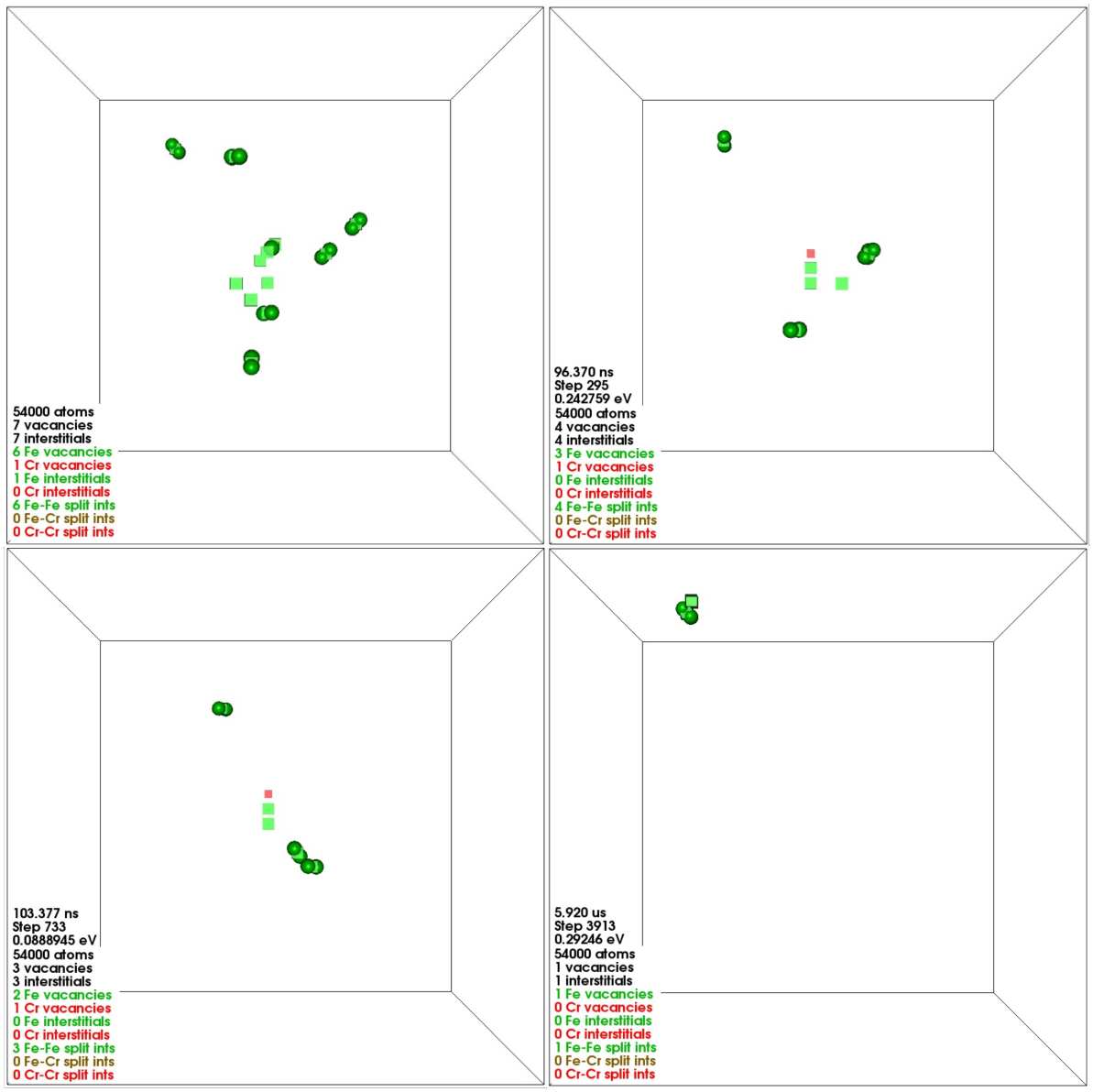

Figure 4.19: Visualisation of an AKMC simulation conducted in a BCC $FeCr_{10\ at.\%}$ system which has experienced a 1 keV PKA collision cascade (system 2b). The initial lattice is shown in the top-right image and snapshots of the simulation at 96.4 ns, 103 ns, and 5.92 µs are shown in the other images. By the second snapshot, three Frenkel pairs have annealed and three of the remaining vacancies have aligned themselves in a straight line along adjacent lattice sites. At 103 ns, one of the interstitial defects that is part of a cluster is breaking away, and in the next step, it recombines with a vacancy. In the step following the last shown here, 5.92 µs, the last Frenkel pair recombines, leave a defect free lattice. Off lattice atoms are visualised as spheres, green for iron, red for chromium, and cubes represent vacancies.

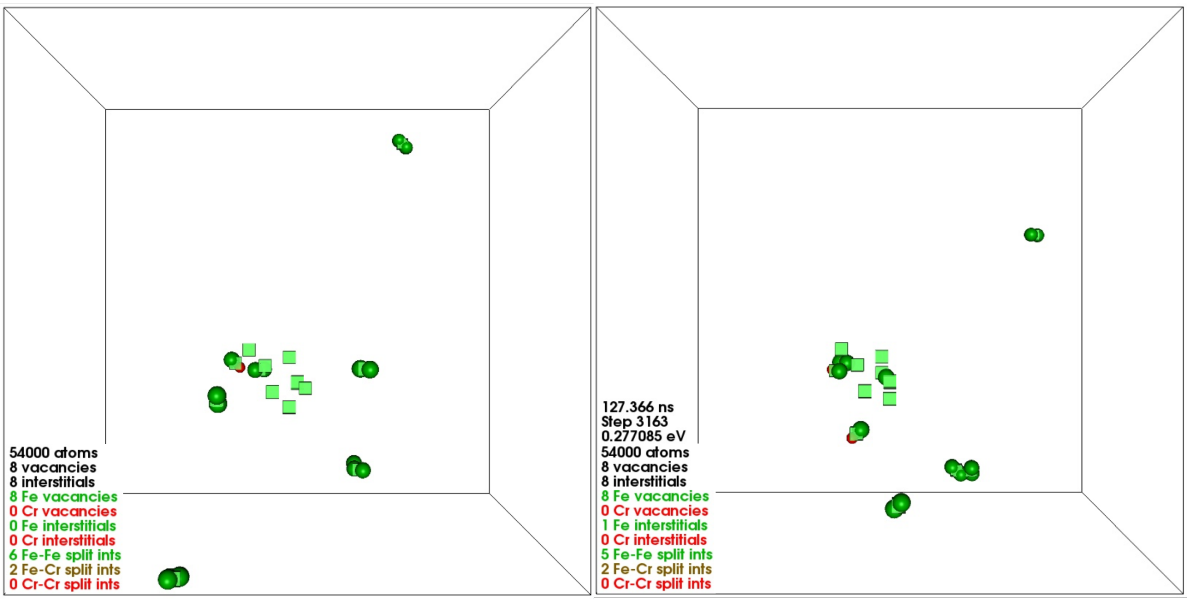

Figure 4.20: Visualisation of an AKMC simulation conducted in a BCC $FeCr_{10\ at.\%}$ system which has experienced a 1 keV PKA collision cascade (system 3). The initial lattice is shown on the right and the image on the left shows the system after 127 ns, during which time, there has been no net change in Frenkel pair count, although a split-interstitial has been lost and a split-vacancy has developed between two empty sites. Off lattice atoms are visualised as spheres, green for iron, red for chromium, and cubes represent vacancies.

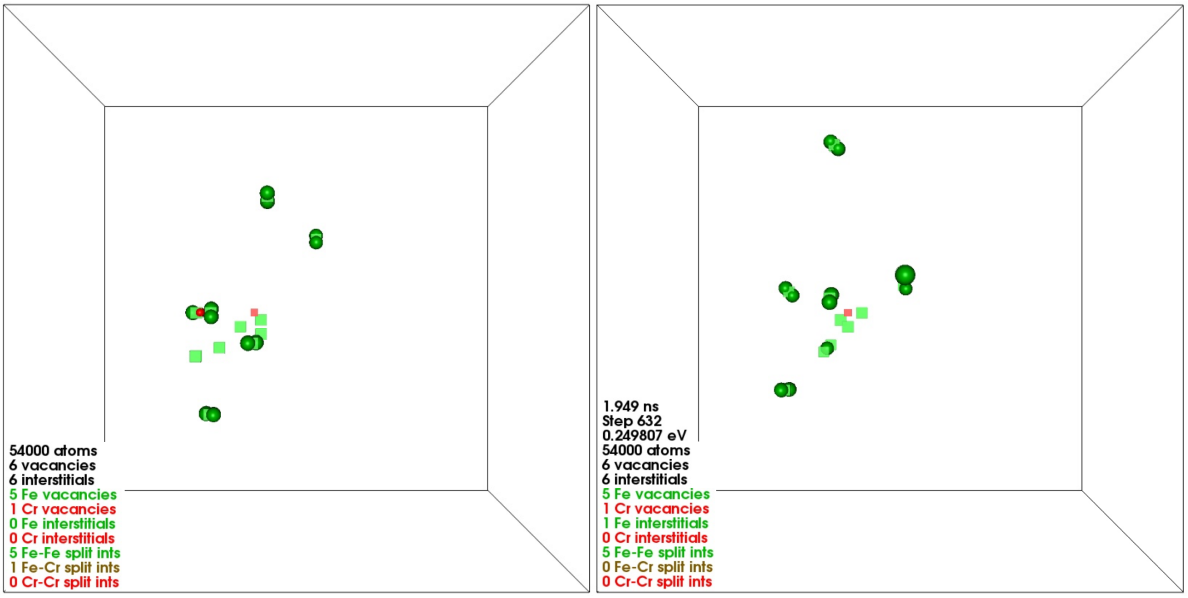

Figure 4.21: Visualisation of an AKMC simulation conducted in a BCC $FeCr_{10\ at.\%}$ system which has experienced a 1 keV PKA collision cascade (system 4). The initial lattice is shown on the right and the image on the left shows the system after 1.95 ns. During this time, no Frenkel pairs anneal, however the cluster of interstitials seen at the beginning of the AKMC simulation has separated. Off lattice atoms are visualised as spheres, green for iron, red for chromium, and cubes represent vacancies.

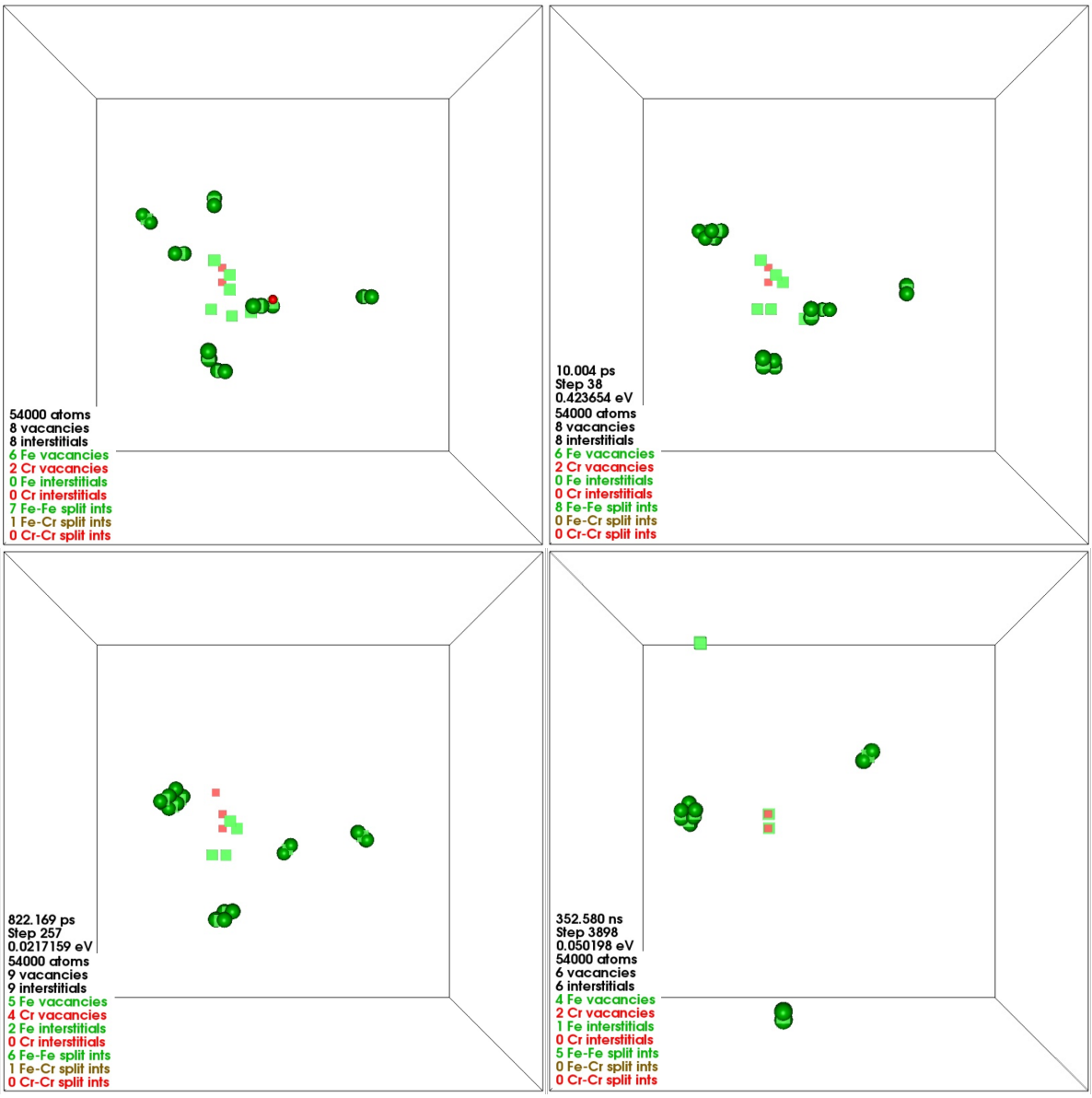

Figure 4.22: Visualisation of an AKMC simulation conducted in a BCC $FeCr_{10\ at.\%}$ system which has experienced a 1 keV PKA collision cascade (system 5). The initial lattice is shown in the top-right image and snapshots of the simulation at 10.0 ps, 822 ps, and 353 ns are shown in the other images. During this simulation, a cluster of six interstitial atoms coalesces, but this structure still has some mobility. A net loss of two Frenkel pairs is seen. Off lattice atoms are visualised as spheres, green for iron, red for chromium, and cubes represent vacancies.

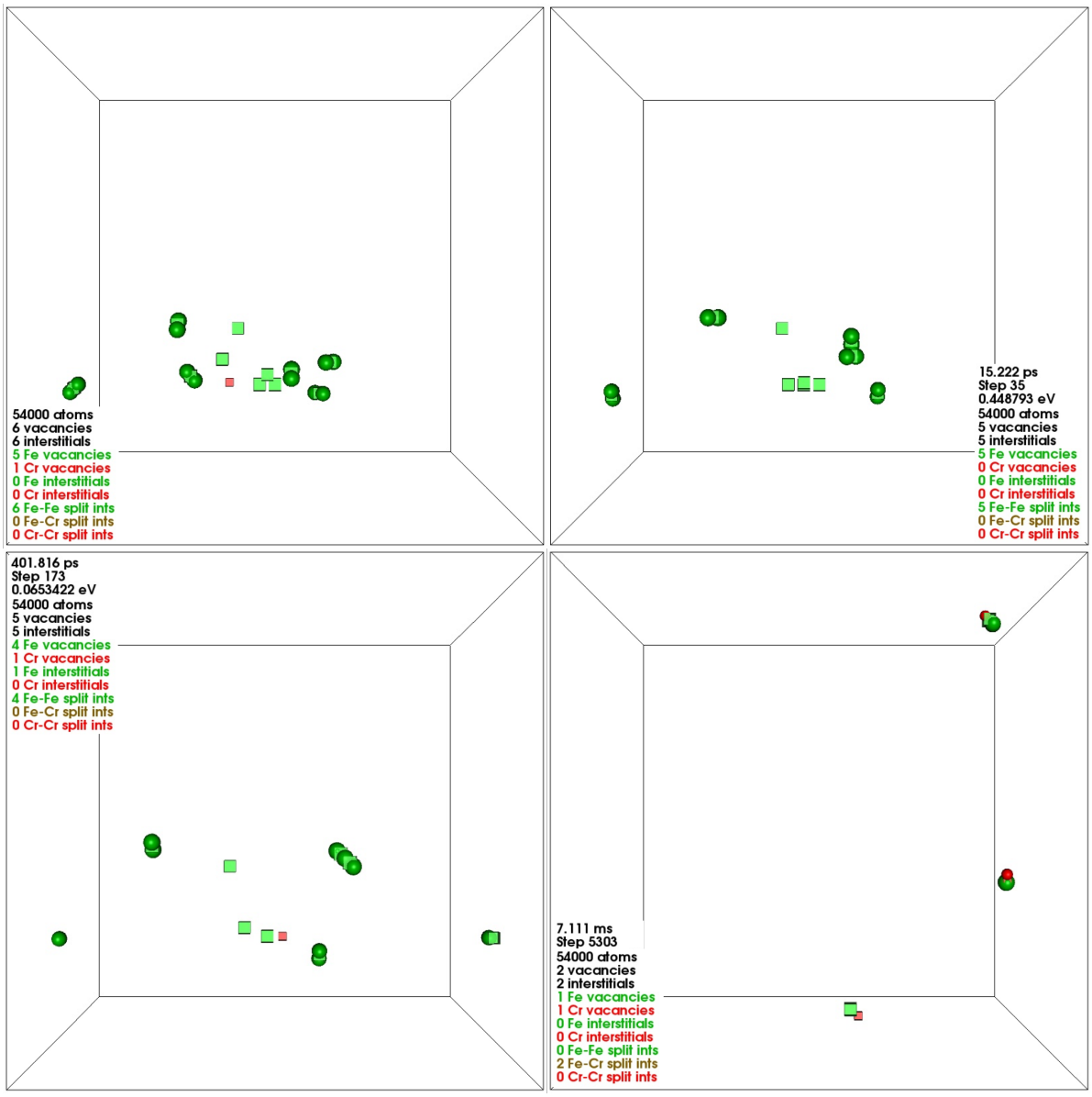

Figure 4.23: Visualisation of an AKMC simulation conducted in a BCC $FeCr_{10\ at.\%}$ system which has experienced a 1 keV PKA collision cascade (system 6). The initial lattice is shown in the top-right image and snapshots of the simulation at 15.2 ps, 402 ps, and 7.11 ms are shown in the other images. During this simulation, the formation and loss of interstitial clusters is seen, as well as another example of vacancies aligning themselves in straight line of adjacent sites, with a forth vacancy directly behind the middle site. Four of the initial six Frenkel pairs recombine, but despite reaching the greatest clock time of all the AKMC simulations, two defects remain. Off lattice atoms are visualised as spheres, green for iron, red for chromium, and cubes represent vacancies.

System	Initial Frenkel Pairs	Final Frenkel Pairs	AKMC Time Simulated	AKMC Steps Taken	Potential Energy Change	Visualisation
1	7	7	34.3 μs	1089	-4.67 eV	Figure 4.17
2a	7	2	1.31 μs	11705	-33.1 eV	Figure 4.18
2b	7	0	5.92 μs	3914	-49.2 eV	Figure 4.19
3	8	8	127 ns	3163	-4.94 eV	Figure 4.20
4	6	6	1.95 ns	632	-5.99 eV	Figure 4.21
5	8	6	353 ns	3898	-31.8 eV	Figure 4.22
6	6	2	7.11 ms	5303	-28.8 eV	Figure 4.23

Table 4.8: Summary of AKMC cascades conducted in post-1 keV PKA collision cascades in $FeCr_{10\ at.\%}$. System 2b sees the complete recombination of its Frenkel pairs, and also experiences the greatest fall in potential energy during the simulation. The AKMC temperature was set at 500 Kelvin, with the application of a low energy basin method with a barrier threshold of 0.5 eV. The Bonny 2011 potential was used to govern interatomic energetics [67, 68].

4.3 Displacement Threshold Energy

In the simulation work, such as ours, that utilises an interatomic potential, properties such as defect formation or migration energies are not directly specified, but emerge from the potential. By contrast, there exist other approaches, such as Objective KMC, where defects are the only objects that explicitly exist in the simulation[4] and the energy barriers to their motion are specified *a priori* as parameters to the simulation [86]. Similarly, the widely used and popular software, SRIM (Stopping and Range of Ions in Matter), requires an explicit specification of the energy required to displace an atom from its lattice site [56]. This operates using a concept known as Displacement Threshold Energy, which is the idea that for some atom in a lattice, there is a single value of kinetic energy that is sufficient to move the atom off-lattice to form a Frenkel pair, and any displacement below this energy will have no "permanent" effect. What constitutes permanence, however, is somewhat arbitrary. Little energy is required to remove an atom from its lattice site, but as one sees from section 4.1, damage can be very short lived. Furthermore, while AKMC shows that defects can anneal

[4] As opposed to deviving the presence of defects from the atom positions and a reference lattice (see section 2.4).

on timescales much longer that we use in MD, these processes are still very transient from a human perspective. Here, we explore if anything resembling a hard threshold exists for $FeCr_{10\ at.\%}$.

Inspired by the work of Robinson *et al.* with TiO_2 in 2012 [110], we approach the problem from a probabilistic perspective. Rather than attempting to quantify a hard threshold, we calculate the probability of defect production in the system as a function of displacement energy. Similar to our work with collision cascades, using Molecular Dynamics, we take a large number of randomly generated $FeCr_{10\ at.\%}$ systems, and in each, we simulate the displacement of a single atom using a range of kinetic energies, with a large spread of displacement vector orientations – three sets of 108 evenly spread points on the unit sphere. We choose to run our simulations to 10 ps; this allows any low stability defects to anneal, while anything remaining by the end of the simulation maybe considered "true" damage – "permanent" on the timescale of MD, if not AKMC.

We simulated displacement energies up to 240 eV for iron and 140 eV for chromium atoms. 100 randomly generated lattices, sized appropriately for the displacement energy, were used for each probability calculation, each thermalised to 500 K before the simulation start, with a Berendsen thermostat to maintain this temperature during the simulation. This brings the total number of data points per displacement energy to 32,400. Our results are shown in figure 4.24.

The results show a sharp initial increase in the success rate of producing defects with respect to displacement energy up to around 40 eV, after which, it becomes steadily more difficult to increase the percentage of systems with surviving defects. For iron, the curve had become almost completely flat in the 200 to 240 eV range, likely because as the displacement energy grows, more atoms (i.e first, second, third nearest neighbours of the displacement atom etc.) become involved in the resisting and restoring forces absorbing the energy. Given the diminishing returns from increasing the displacement energy, and the high computing cost of generating good statistics, it was decided not to continue these calculations any

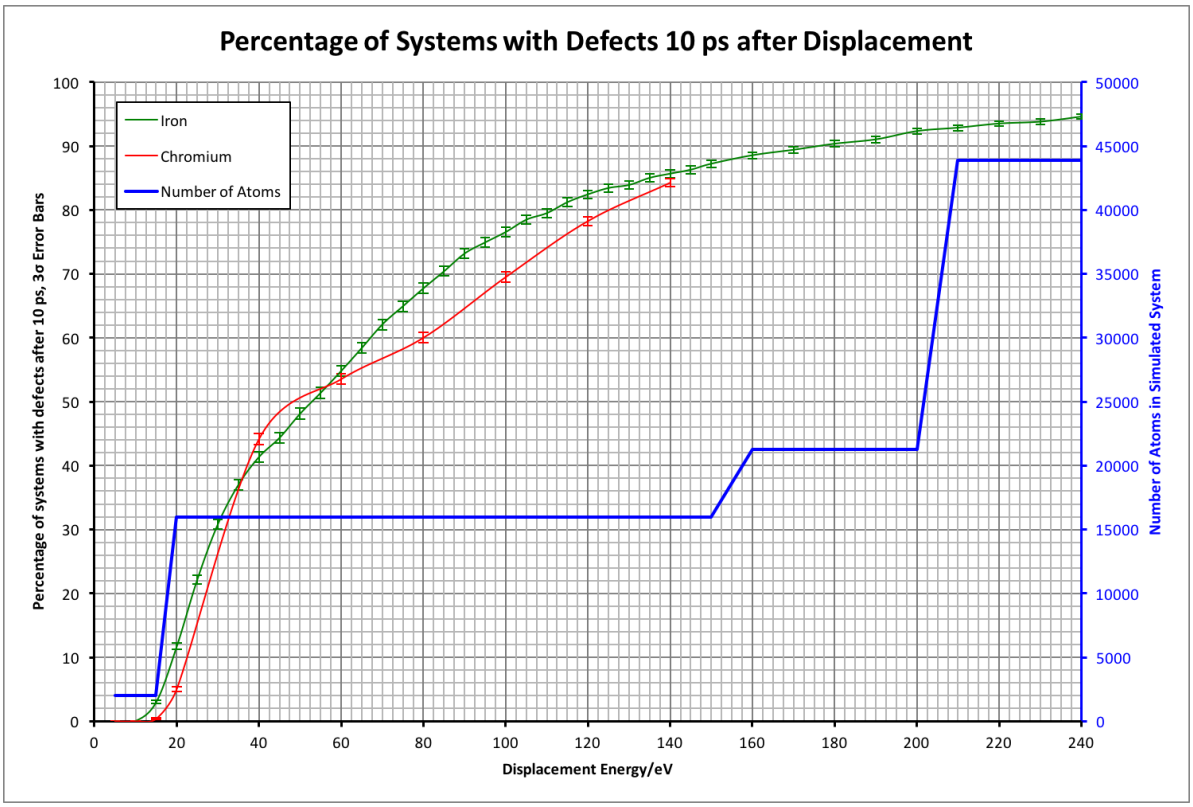

Figure 4.24: Using the Bonny 2011 potential [67] we have calculated the probability of an $FeCr_{10\ at.\%}$ system containing defects, 10 ps after a small displacement energy is introduced to either an iron or a chromium atom. A Berendsen was used to maintain a system temperature of 500 K. The results for the displacement of iron and chromium atoms are shown in green and red, respectively, with the number of atoms used to contain the event illustrated in blue. 32,400 data points are used for each energy and our standard error is low; as such we mark our error bars on this graph at 3σ, corresponding to 99.73% confidence.

further. Displacing an iron atom with 240 eV achieves a surviving defect creation success rate close to 95%. With the exception of the one data point at 40 eV, displacing a chromium is less likely to produce surviving defects in the system.

4.4 PKA Orientation

When greater limits on available computing power constrained computational work, it was common for one to sample only one PKA vector, allowing fewer simulations to be run. To avoid the results from being biased by channelling effects, a high-index orientation would be selected [51], for example, $\langle 1\ 3\ 5 \rangle$.

In this section we examine how the simulations are effected when the PKA vectors are

limited to the ⟨1 3 5⟩ orientation, since this technique still sees some use. For example, in 2005, Terentyev *et al.* conducted work in BCC $FeCr_{10\ at.\%}$ at 300 Kelvin where only ⟨1 3 5⟩ vectors were employed [39]. We have simulated fifty systems with the eight possible ⟨1 3 5⟩ vectors to compare with five systems where an even spread of 108 vectors were used, with these simulations conducted at 300 Kelvin. The evolution of these systems may be seen in figure 4.25, with a summary of the final state of the systems to be found in table 4.9.

The intermediate and final number of Frenkel pairs are not significantly different; however, there is a large disparity between the distribution of chromium in the two sets, see figure 4.26. There is a much larger occurrence of chromium in lone and split-interstitials (and therefore in overall defect atoms). Comparing these results to Terentyev *et al.* 2005 [39], we notice that their 1 keV cascades exhibit a similar trend, see figure 6 (inset image) of the paper, although their choice of interatomic potential differs from ours, being taken from a 2002 work by Chakarova *et al.* [111, 112]. Similarly, Wallenius *et al.* 2004 [47] also use ⟨1 3 5⟩ PKA vectors only. In their cascade simulations performed at 100 Kelvin using a potential described in the same paper, they find that in $FeCr_{5\ at.\%}$, 19% of their interstitial atoms are chromium – far more than seen in our results where an even spread of PKA vectors was used, and similar to our ⟨1 3 5⟩ results.

On this basis, while using only ⟨1 3 5⟩ orientated PKA vectors should be acceptable for estimates of Frenkel pair production, we would caution against its use when one is

Table 4.9: Lattice defects remaining 6 ps after a 1 keV PKA was introduced to 54,000 atom $FeCr_{10\ at.\%}$ systems at 300 Kelvin, comparing a set of PKA orientations that samples the entire unit sphere to only PKA vectors in the ⟨1 3 5⟩ orientation (No post-cascade minimisation).

PKA Vector Set	Defect Atoms of which Cr (%)	Lone Interstitials	Split-Interstitials	Total Frenkel Pairs
⟨1 3 5⟩	22 ± 2	1.71±0.07	4.32±0.09	6.03±0.11
Spread	9.0±1.2	1.16±0.04	4.60±0.08	5.76±0.08
PKA Vector Set	LIAs of which Cr (%)	SIs of which FeFe (%)	SIs of which FeCr (%)	SIs of which CrCr (%)
⟨1 3 5⟩	37±2	68±2	27±2	4.8±1.1
Spread	14.4±1.5	83.9±1.6	15.7±1.6	0.4±0.2

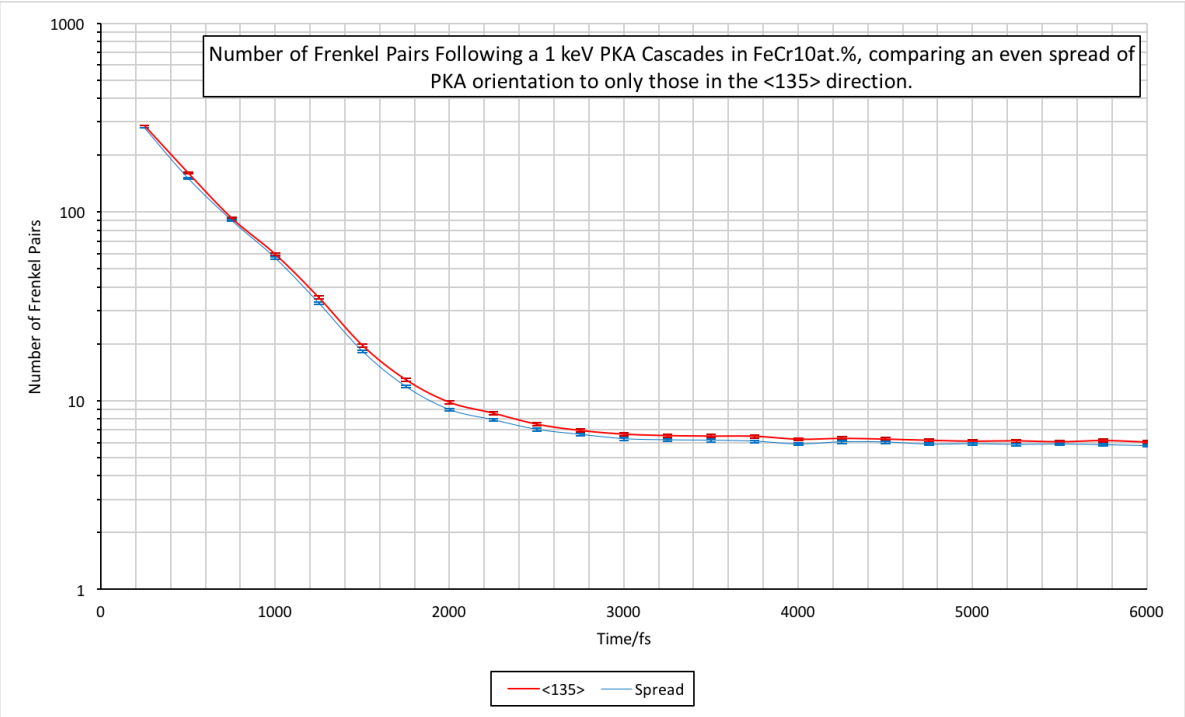

Figure 4.25: Evolution of the number of Frenkel pairs in two sets of 1 keV collision cascades in $FeCr_{10\ at.\%}$ – with one set using PKA vectors in the $\langle 1\ 3\ 5 \rangle$ orientation only, and the other employing an even sample of the unit sphere. Please note that the number of Frenkel pairs is presented on a logarithmic axis.

investigating species dependent behaviour, and encourage evenly sampling the unit sphere.

4.5 Chapter Conclusions

From the results presented in this chapter, we find that varying the concentration of chromium in the atomic lattices does not have any apparent effect on the production of Frenkel pairs during the collision cascades simulated. We do find that simulating our systems at a temperature of 500 Kelvin produces fewer final Frenkel pairs by comparison to those conducted at 0 Kelvin, and that at the elevated temperature, chromium atoms are found in defect objects at a higher rate than would be commensurate with their bulk concentration, while the opposite is observed for the low temperature systems. In the simulations conducted at 500 Kelvin, the over-representation of chromium phenomena was most pronounced at the lowest bulk concentration. With the simulations conducted at 0 Kelvin, while a linear relationship between a cascade's PKA energy and the final Frenkel pair count was seen, its linearity must

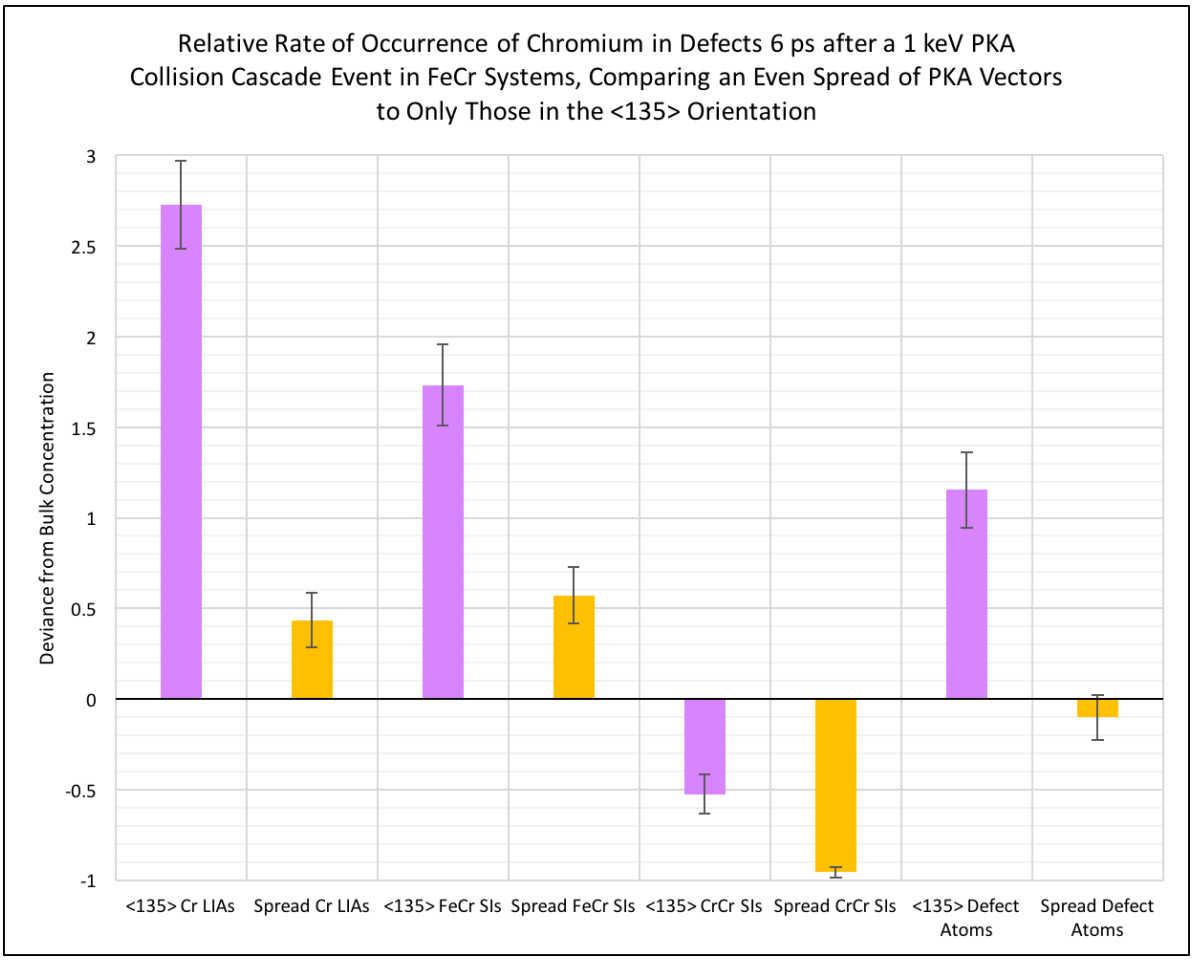

Figure 4.26: Relative rate of occurrence of chromium atoms in defects in systems 6 ps after a 1 keV collision cascade has occurred in $FeCr_{10\ at.\%}$, with one set of data using PKA vectors in the $\langle 1\ 3\ 5 \rangle$ orientation only, and the other employing an even sample of the unit sphere (No post-cascade minimisation). Values calculated by dividing the percentage rate of occurrence of defect as by the relevant reference figure in 4.1, and then subtracting one from the result. Thus, positive values indicate a higher fraction of chromium in defect atoms than the bulk, and negative values indicate the converse.

break down at lower energies, such that zero cascade energy produces no damage. Furthermore, PKA energy was not observed to affect the chromium defect representation.

We also found that the use of L-BFGS-B/CG minimisation on the 500 Kelvin post-cascade lattices causes distortions in the results, and as such made use of the much more computationally costly method of damped-MD. With the low temperature systems, L-BFGS-B/CG minimisation could be used without issue. Minimising via either method results in a reduction of lone interstitial atoms in favour of split-interstitials, and a small overall fall in total Frenkel pairs.

In our study of displacement threshold energy, while in places, the rate of increase in successful defect production rises rapidly with increasing displacement energy, there is no definitively sharp transition from low success rate to high success rate that could be regarded as a "threshold energy". For both iron and chromium in $FeCr_{10\ at.\%}$ lattice systems, the displacement energy for which the defect production success rate was 50%, was approximately 55 eV.

Comparing the use of the representative vector, $\langle 1\ 3\ 5 \rangle$, to an even sampling of the unit sphere, we found that in 1 keV cascades conducted at 300 Kelvin, the number of Frenkel pairs produced was not significantly altered, but in the former set of cascade simulations, the over-representation of chromium was increased significantly, and this behaviour is also evident in publications that employ the $\langle 1\ 3\ 5 \rangle$ vector to save on computational expenditure [39, 47].

Barrier searches conducted on the potential energy hypersurfaces of $FeCr_{10\ at.\%}$ and pure iron lattices suggest greater defect mobility in the former. Using the AKMC method, we simulation the damage recovery process of six $FeCr_{10\ at.\%}$ systems after a 1 keV PKA cascade. In the computer time allotted to this task, only one system fully annealed, taking 6 μs to do so. During the AKMC simulations, clusters of interstitial defects are seen to coalesce and then disperse, while the generally less mobile vacancies are observed aligning themselves along adjacent lattice sites.

Chapter 5

Modelling Experimental Work

5.1 Experimental Context

There are very few experimental facilities with the capacity to replicate nuclear reactor like-conditions, and even where these exist, the procedure is expensive and time consuming. In addition, neutron induced activation leaves materials unsafe to interact with for extensive periods. For this reason, many experimentalists choose to use alternatives which can achieve high DPA rates over short periods, and whose low activation makes irradiated samples comparatively easy to handle. In lieu of neutrons, one may bombard materials with highly energetic protons, electrons, or heavy ions, which, being charged, are much less likely to be absorbed by target nuclei.

We were interested in using our atomistic modelling software to simulate a sequence of cascade events that reflected the conditions experienced by a nuclear pressure vessel in a nuclear reactor. However, the relevant information proved difficult to obtain, so we instead turned to attempting to replicate experimental analogues. In our example procedure, steel rods at room temperature are exposed to protons with a kinetic energy of 3 MeV, at a flux of 3×10^{17} $s^{-1}\cdot cm^{-2}$, and these figures serve as the basis of our model [113].

5.2 Creating a Physically Representative Model

5.2.1 SRIM: The Stopping & Range of Ions in Matter

To convert the given description to figures that we can apply in our models, we utilised the third-party software package, SRIM (The Stopping & Range of Ions in Matter), which is freely available online [56,57]. SRIM uses the binary collision approximation [114] to compute the path of moving ions as they interact with, and deposit energy into, a given material. A Monte Carlo algorithm is used to calculate distances travelled by ions between interactions with atoms, based on the density of the material. Electronic stopping is considered in free space, with interactions between ions and the system's atomic nuclei abstracted to direct "collisions", wherein the classical scattering integral is solved, see figure 5.1.

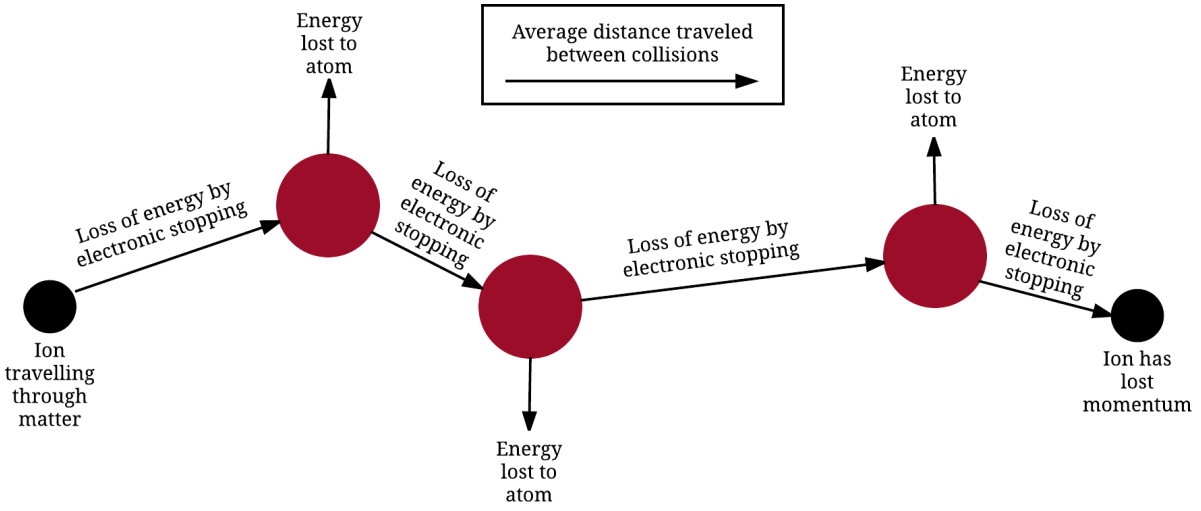

Figure 5.1: Illustration of the Binary Collision Approximation, as applied by SRIM. An ion travelling through matter travels between collisions for a random distance, whose average is based on the density of the material. Each interaction between the ion and an atom is considered in terms of those two bodies only, where the classical scattering integral is solved, and during transit between atoms, the atom losses momentum by electronic stopping forces [56].

5.2.1.1 Two-Body Scattering of Ions by Atoms

Suppose one takes an interaction between an atom and a light ion, moving in the laboratory frame of reference, such as is seen in figure 5.2. Letting the mass of the atom and of the

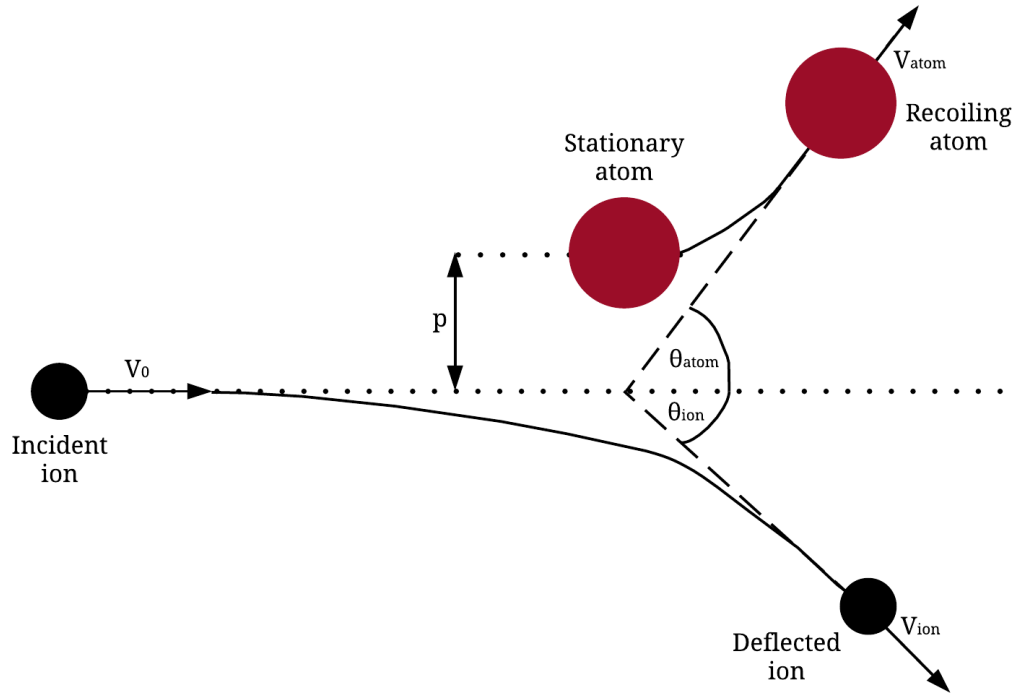

Figure 5.2: Diagram of two body interaction between a light ion and an atom, depicted in the laboratory frame of reference. The ion has incident velocity $\vec{V}_0$ and after interaction, the atom and ion have velocities, $\vec{V}_{\text{atom}}$ and $\vec{V}_{\text{ion}}$, at angles θ_{atom} and θ_{ion} from the initial trajectory of the ion. The perpendicular separation between the objects is given by p.

ion be M_{atom} and M_{ion} respectively, and defining $\vec{V}_0$ as the incident velocity of the ion, the energy lost by the ion to an atom through a collision, T is given by [56],

$$T = \frac{2}{M_{\text{atom}}} \left(\frac{|\,\vec{V}_0\,|\, M_{\text{atom}} M_{\text{ion}} \cos\theta_{\text{atom}}}{M_{\text{atom}} + M_{\text{ion}}} \right)^2 \tag{5.1}$$

where θ_{atom} is the angle at which the atom recoils relative to the original trajectory of the ion, and is given by equation 5.2.

$$\theta_{\text{atom}} = \frac{1}{2} \int_{-\infty}^{\infty} \left(\frac{p}{r^2} \left[1 - \frac{V(r)}{E} - \frac{p^2}{r^2} \right]^{-1/2} \right) \mathrm{d}r \tag{5.2}$$

where p is the initial perpendicular separation between the ion and the atom, see figure 5.2, $V(r)$ is the ZBL potential [56], see equation 2.27, and E is the kinetic energy of the system's

centre of mass, such that,

$$E = \frac{1}{2}\frac{M_{\text{atom}}M_{\text{ion}}}{M_{\text{atom}} + M_{\text{ion}}} \mid \vec{V}_0 \mid^2 \tag{5.3}$$

The angle of defection of the ion is then given by [56],

$$\theta_{\text{ion}} = \arctan\left(\frac{M_{\text{atom}} \sin 2\theta_{\text{atom}}}{M_{\text{ion}} - M_{\text{atom}} \cos 2\theta_{\text{atom}}}\right) \tag{5.4}$$

5.2.1.2 Electronic Stopping Power

SRIM calculates the energy loss to electronic stopping using empirical data. The electronic stopping power that SRIM provides for protons in $FeCr_{10\ \text{at.}\%}$ is shown in figure 5.3.

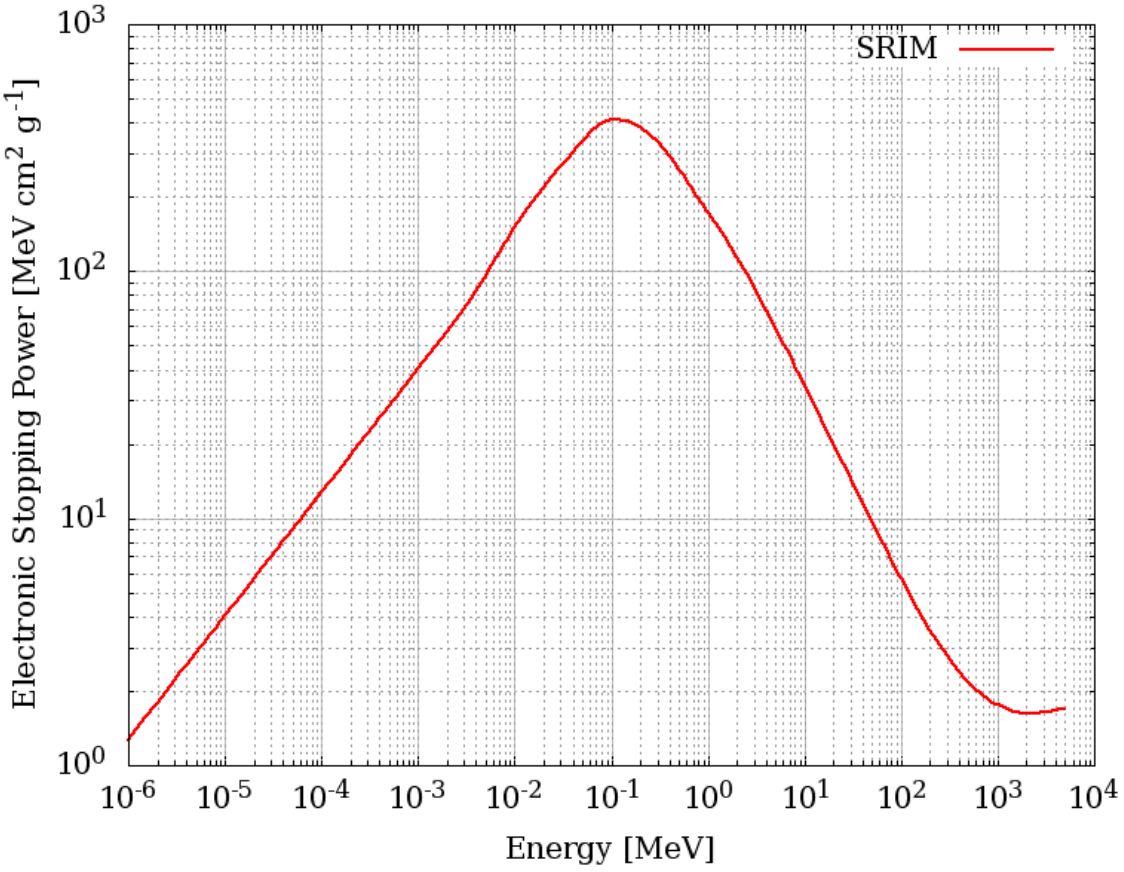

Figure 5.3: Electronic stopping in $FeCr_{10\ \text{at.}\%}$, as calculated by SRIM [56, 57] for protons with kinetic energies below 10^4 MeV. Image generated by [115].

5.2.1.3 SRIM Calculations

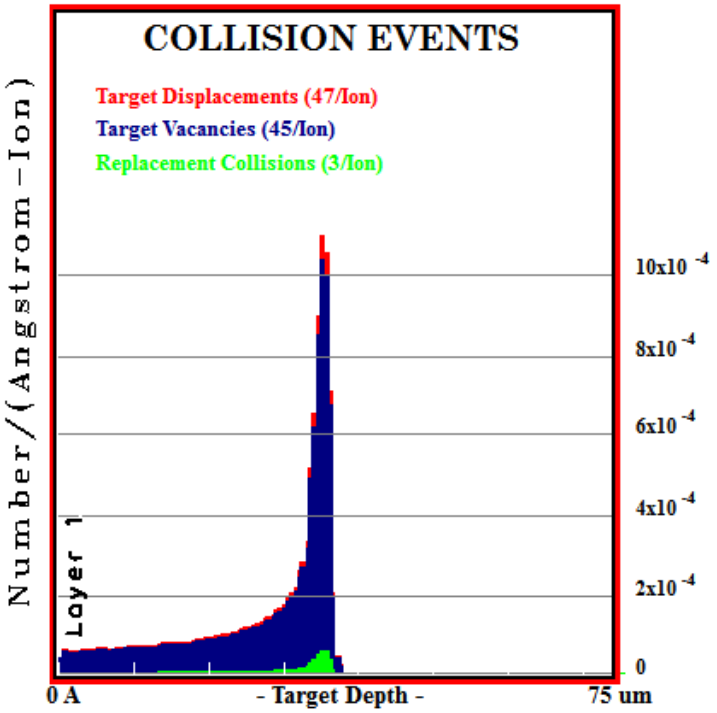

Figure 5.4: Collision events as a function of depth from one million full-cascade SRIM calculations of 3 MeV protons in $FeCr_{10at.\%}$ of density 7.849 g·cm^{-3}.

We performed one million of SRIM's "full cascade" TRIM[1] calculations with 3 MeV protons in a material of iron and chromium atoms at a ratio of 9:1 and a density[2] of 7.849 g·cm^{-3}. The collision events resulting from these calculations are displayed in figure 5.4, where it is seen that the protons are halted between 35 to 40 μm. We opted to sample the region 10 to 15 μm, as the number of events as a function of depth is comparatively flat over this domain. Within these 5 μm, 3,843,201 events occurred (including secondary displacements) and the distribution of their energies is shown in figure 5.5. For the largest PKA energy that we permit in our model, 5 keV, we require 432,000 atoms to contain the cascade. These are arranged in a cube of sides 17.2 nm. If our simulation cell is placed in the sample depth, its size, the experimental proton flux, and the data produced by SRIM equates to a rate of 0.370 cascade events per second, see figure 5.6. This figure accounts for the inclusive upper

[1] **TR**ansport of **I**ons in **M**atter

[2] Based on the density of atoms at the ideal lattice parameter predicted by the Bonny 2011, i.e. 2.863 Å.

and lower bounds we set for the event energies, 60 eV to 5000 eV; events below 60 eV do not produce damage that survives the ballistic phase[3], see figure 4.24, and events in excess of 5000 eV are sufficiently rare as to be neglected.

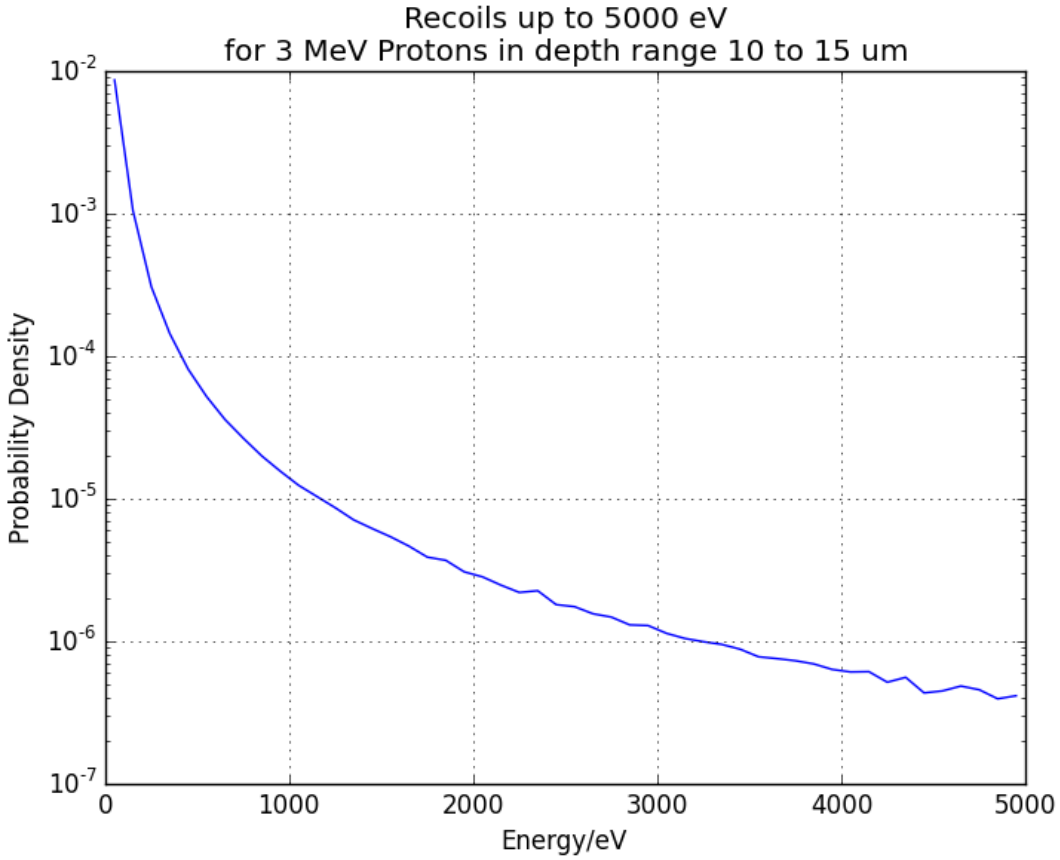

Figure 5.5: Distribution of event energies for one million full-cascade SRIM calculations of 3 MeV protons in $FeCr_{10\ at.\%}$ of density 7.849 g·cm^{-3}. The 50th, 90th, and 99th percentiles are 41.7 eV, 155 eV, and 1040 eV respectively, with 99.85% of events below 5 keV.

5.2.1.4 Cascade Procedure

To simulate the conditions described by the experimental team, we conducted multiple MD simulations of collision cascades, with AKMC simulation between cascades. The first cascade in each system was placed in the centre of the lattice, with all subsequent PKAs being selected at random. We generated ten $FeCr_{10\ at.\%}$ systems of 432,000 atoms, and because the PKAs are randomly selected (and therefore could be anywhere in the system), no thermostat is

[3]or otherwise, would produce Frenkel pairs sufficiently localised as to recombine in a single AKMC step

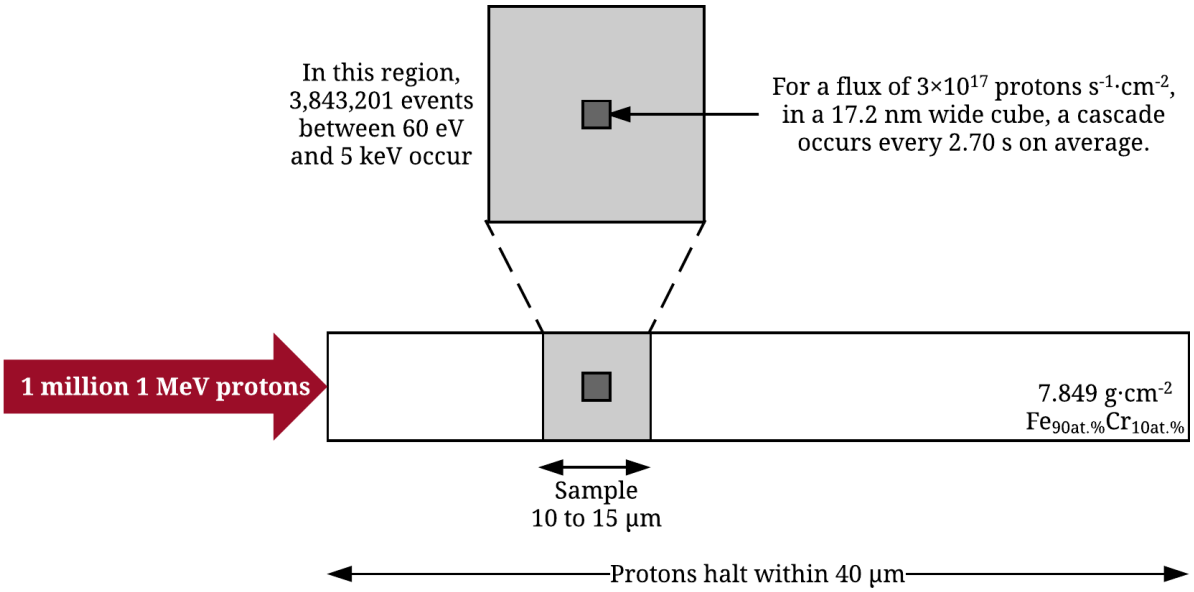

Figure 5.6: Schematic of depicting the sampling of data produced by SRIM calculations for one million 1 MeV protons in $FeCr_{10\ at.\%}$ to arrive at an average occurrence rate for collision cascades in a given volume.

applied during the simulation, meaning that the number of atoms could be reduced from the 500,094 used for 5 keV cascades in section 4.1.1. Before each collision cascade, the lattices were thermalised to 300 Kelvin, and each MD simulation would last 10 ps. If Frenkel pairs survived to the end of the ballistic phase, AKMC at 300 Kelvin would be used to simulate lattice recovery until either all Frenkel pairs had recombined, or the time scheduled for the next event was reached. Then, the lattices would be thermalised again, prior to the next cascade. The interval between individual events in a system was assigned via equation 3.5, for $n = 1$ and $k_1 = 0.370\ \mathrm{s}^{-1}$.

5.2.2 Simulation Results

Table 5.1 shows the progression of the ten simulations, the events selected, the interval between the events, and the defect annealing recovery times. As apparent from figure 5.5, low energy cascades dominate the events, with ten of the nineteen events falling below 150 eV. This has two main consequences:

- The number of Frenkel pairs present at the end of the MD phase is typically small. Of nineteen total events, six produce only one Frenkel pair surviving to 10 ps, and in four

Table 5.1: Summary of multiple collision cascades in $FeCr_{10\ at.\%}$ with AKMC recovery between events. Recovery times are measured from the end of the last MD phase of the simulation. *In system 10, the single vacancy-interstitial pair produced by the first event is left well separated after a large number of AKMC steps. For this reason, we proceeded to the next event at 5.40 ms.

System	Event 1			
	Event Start/s	PKA Energy/eV	Frenkel Pairs 10 ps After Event	Recovery Time/s
1	0	95	1	5.06×10^{-10}
2	0	75	0	-
3	0	75	1	-
4	0	125	1	1.10×10^{-11}
5	0	70	0	-
6	0	210	3	4 Frenkel pairs remaining at 823 ms
7	0	220	2	2 Frenkel pairs remaining at 0 s
8	0	160	0	-
9	0	180	2	2 Frenkel pairs remaining at 124 μs
10	0	55	1	5.40×10^{-3} *
System	Event 2			
	Event Start/s	PKA Energy/eV	Frenkel Pairs 10 ps After Event	Recovery Time/s
1	3.01	60	1	1 Frenkel pairs remaining at 1.65 μs
2	1.70	130	1	1.24×10^{-3}
3	4.10	60	0	-
4	0.863	470	5	2 Frenkel pairs remaining at 68.8 μs
5	1.16	180	2	1 Frenkel pairs remaining at 24.7 μs
8	2.11	160	3	2 Frenkel pairs remaining at 1.09 μs
10	0.776	80	3	2 Frenkel pairs remaining at 99.7 μs
System	Event 3			
	Event Start/s	PKA Energy/eV	Frenkel Pairs 10 ps After Event	Recovery Time/s
2	12.9	450	3	3 Frenkel pairs remaining at 0 s
3	8.05	960	7	7 Frenkel pairs remaining at 35.7 ms

cases none survive at all.

- Correspondingly, the volume in which damage (transient or otherwise) caused by a cascade occurs is small. Thus, the likelihood of it intersecting with either a region in which a previous event occurred, or any surviving damage, is sufficiently low that we have no example of this happening.

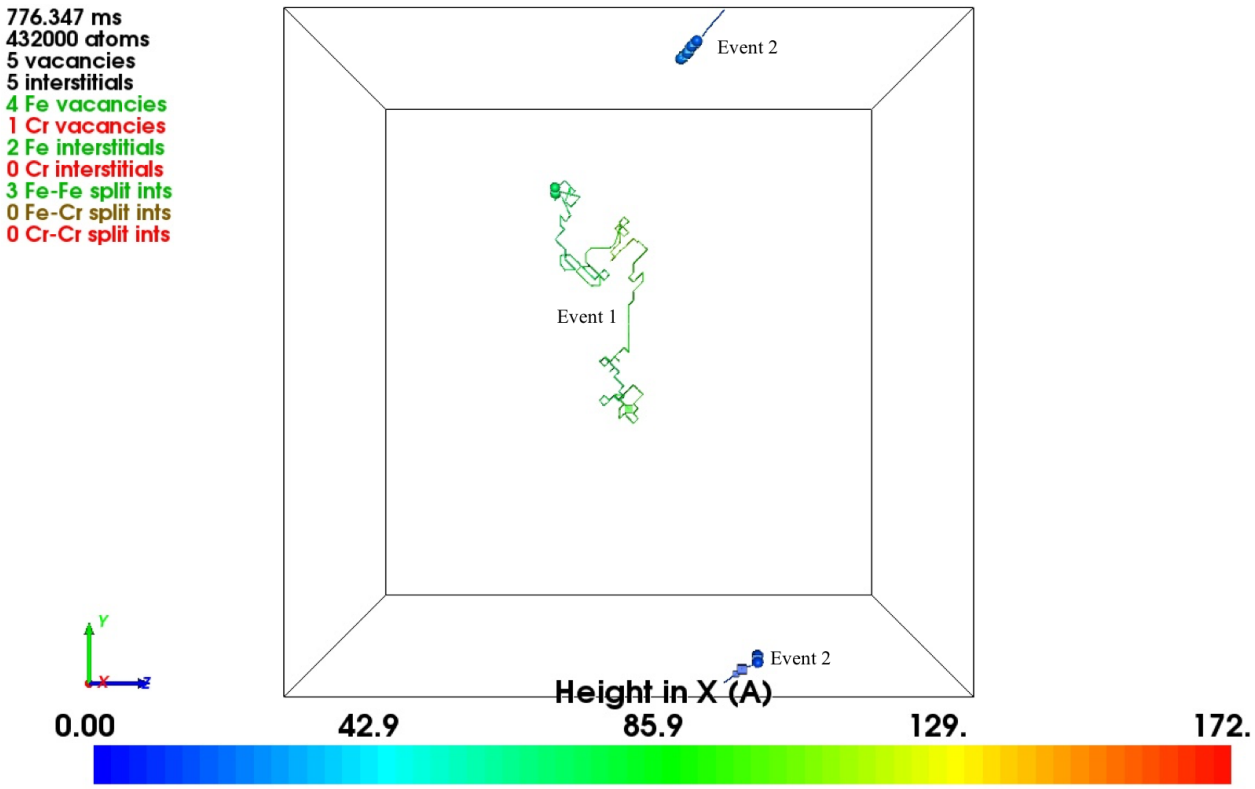

Figure 5.7: In system 10, a second cascade event is introduced at 0.776 s. The damage remaining from the previous cascade is seen towards the middle of the image, where the migration of the defect pair may be seen from the defect replacement chain. The cascade in progress is seen at the top and bottom of the image, with the event crossing the periodic boundary conditions, and being well separated from the location of the first event. Off lattice atoms are visualised as spheres and vacancies as with cubes, with colour denoting depth.

The examples where complete lattice recovery occurs do so on timescales far smaller than the 2.70 second mean interval between events, and consequently we do not have any examples of cascades occurring in systems where there are still defects present from prior events, with the exception of system 10. System 10's initial cascade produced one Frenkel pair and after 5.40 ms of AKMC simulation, it had not annealed, with the vacancy and interstitial

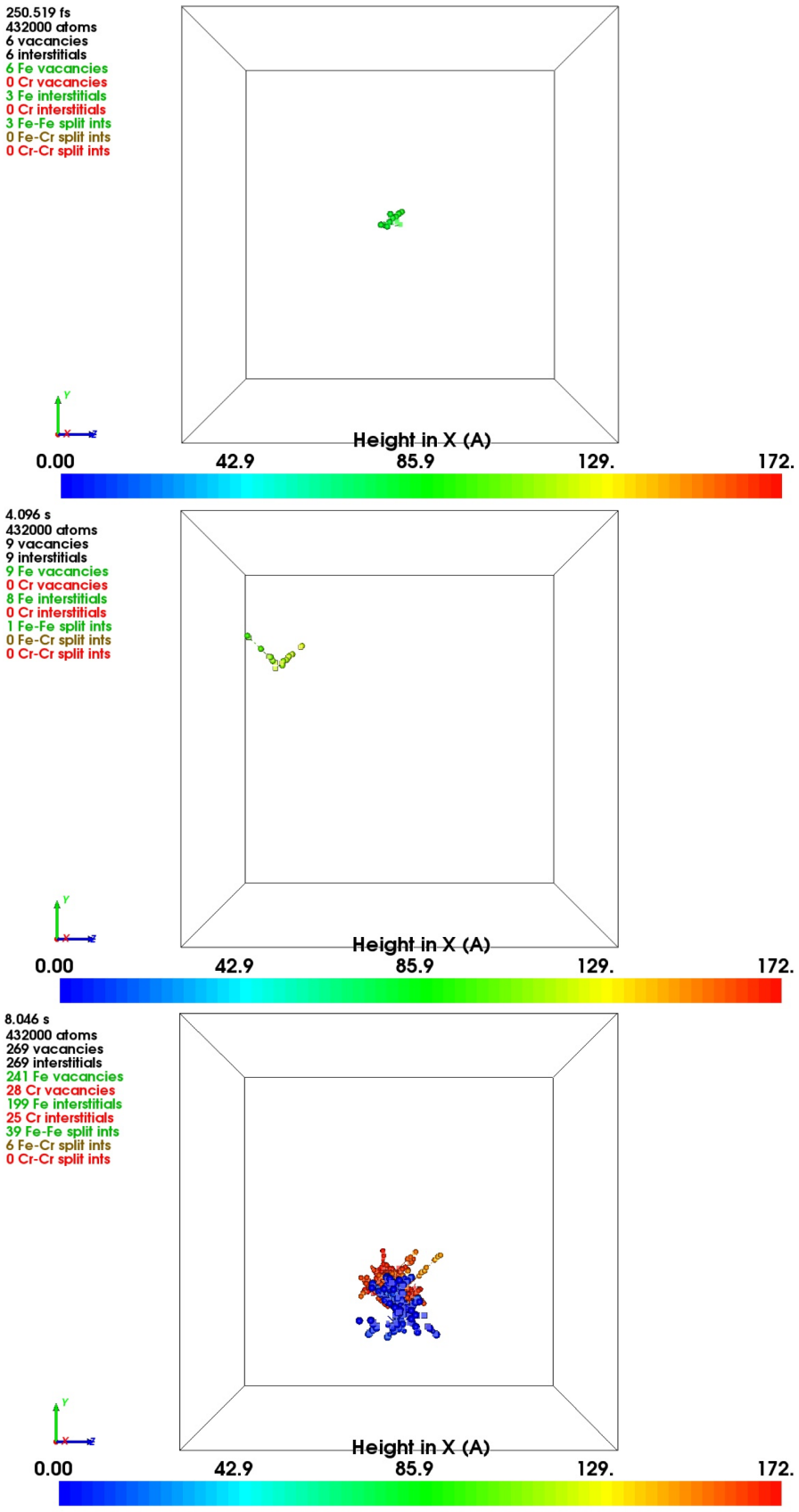

Figure 5.8: Snapshots from system 3, shortly after each of the three cascade events occur, with PKA energies 75 eV, 60 eV, and 960 eV respectively. Off lattice atoms are visualised as spheres and vacancies as with cubes, with colour denoting depth.

defects well separated from each other, and not making progress towards recombining. In these systems, larger than those used in section 4.2, the greatest possible separation between two defects is considerably further. Thus, this system was advanced to its second cascade. While system 10 therefore experienced a cascade event with existing lattice defects, the second event was low in energy, and its PKA's original location was not in proximity to either defect. Consequently, the region containing the cascade did not intersect the volume surrounding the existing damage, see figure 5.7. Similarly, in system 3, which experienced both the highest number of events, and the single most energetic event, the cascades are distant from each other, see figure 5.8. Examining the distribution of atomic species in the lattices before and after the simulations[4], we find that one to three cascade events occurring over timescales on the order of a few seconds is not sufficient to detect any segregation of elements.

5.3 MD Timescale Multiple Cascades

In the previous section, we saw that conducting our multiple cascade model with a physically representative event frequency means that the high expenditure of computing required during the recovery phase makes our simulations sufficiently slow that we do not accumulate high damage in the systems, or observe overlapping cascade regions. We considered continuing the model in its original form, or making alterations to the range of event energies available, but ultimately settled on constructing a model where we forego the AKMC recovery phase of the simulation. To this end, we took the ten $FeCr_{10\ at.\%}$ systems of 432,000 atoms created, and began new simulations, using the same probability distribution for the event energies as before. In these simulations, however, rather than switching to AKMC after each MD phase, the system would immediately be thermalised and the next cascade introduced. This scheme of modelling multiple cascades on MD timescales is similar to the technique used by Nord *et al.* 2003 [116] in GaN. Fifteen cascades were simulated per system, and a summary may be

[4] via the radial distribution function

Table 5.2: Summary of fifteen consecutive collision cascade events occurring in ten $FeCr_{10\ at.\%}$ systems of 432,000 atoms. PKA energies were selected probabilistically based on data generated by SRIM, see figure 5.5. Clusters are defined as multiple defect objects within 2.9 Å of each other.

System	Event															Total Cascade Energy /eV	Final Frenkel Pairs	Interstitial Clusters	Vacancy Clusters	Overlapping Cascades
	1	2	3	4	5	6	7	8	9	10	11	12	13	14	15					
	PKA Energy /eV																			
1	290	70	100	80	140	300	310	170	250	1020	140	170	100	120	1180	4440	25	2	4	0
2	290	70	180	80	70	70	500	90	140	90	280	80	140	60	970	3110	18	0	1	0
3	670	70	90	180	70	130	170	190	330	110	70	250	90	70	120	2610	22	1	2	0
4	70	180	60	140	70	130	70	190	3480	60	100	120	150	80	70	4970	24	1	2	0
5	60	130	160	80	140	100	140	260	60	100	80	130	1370	300	60	3170	20	3	1	1
6	90	300	110	2530	140	220	60	60	90	60	100	70	150	670	60	4710	28	2	1	2
7	80	70	150	60	280	180	60	70	370	140	110	80	90	80	110	1930	9	0	2	0
8	100	2050	100	150	60	60	110	80	80	60	70	60	80	280	110	3450	24	2	4	1
9	90	90	90	150	60	60	70	460	90	80	830	240	110	130	60	2610	26	3	5	1
10	90	100	100	140	60	800	100	340	90	150	80	70	70	70	330	2590	23	2	2	1
Average	220±30															3400±300	21.9±1.7	1.6±0.3	2.4±0.5	0.6±0.2

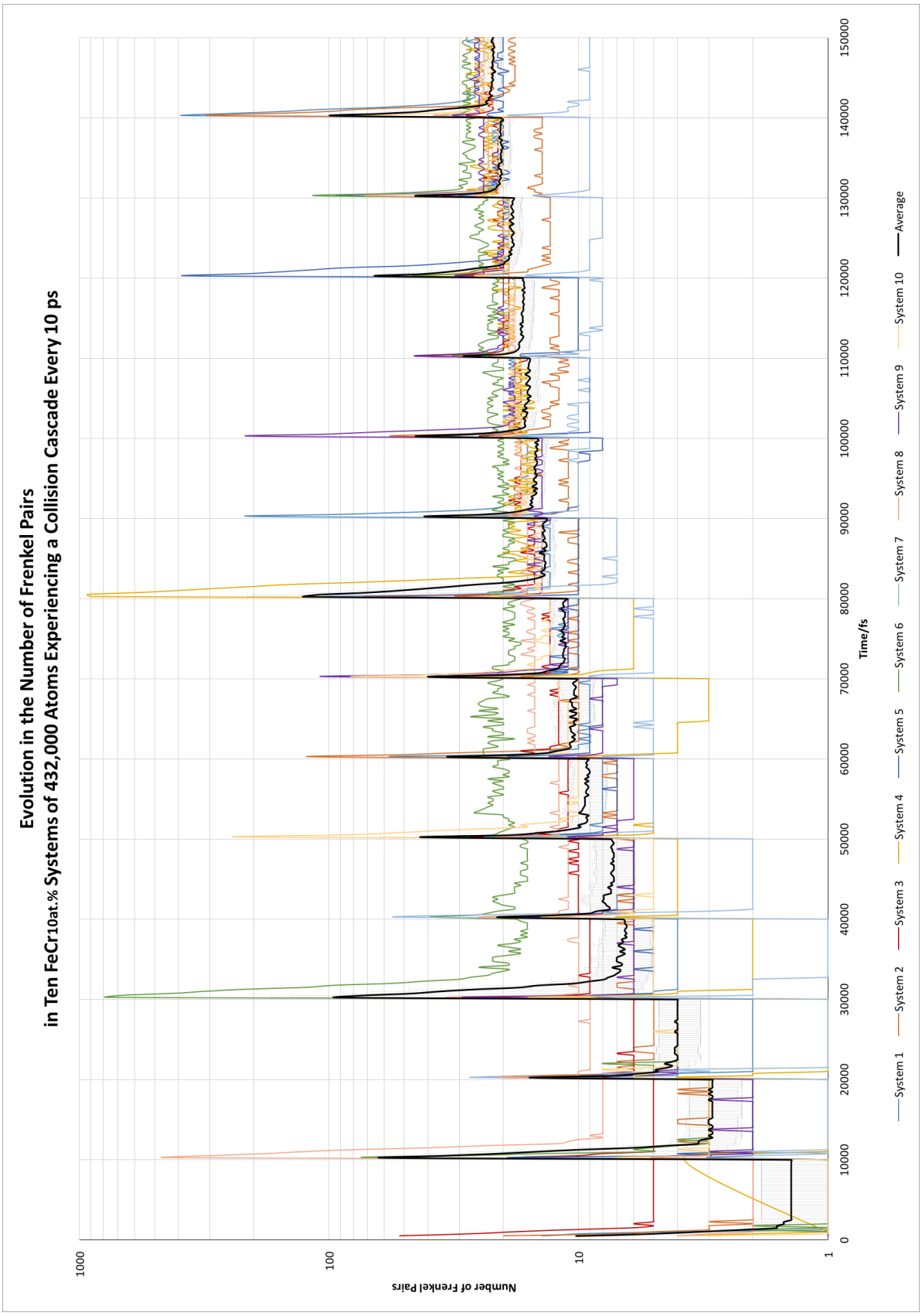

Figure 5.9: Evolution of the number of Frenkel pairs (NB: presented on a logarithm axis) during fifteen consecutive collision cascade events occurring in ten $FeCr_{10\ at.\%}$ systems of 432,000 atoms. PKA energies, found in table 5.2, were selected probabilistically based on data generated by SRIM, see figure 5.5.

found in table 5.2, with the evolution of the number of Frenkel pairs seen in figure 5.9. In figures 5.11 to 5.20, the final states of each lattice are shown; in these visualisations, colour is applied according to depth, and to aid in identifying where cascades have overlapped, defect replacement chains are rendered.

Over the course of the fifteen collision cascades, the number of Frenkel pairs steadily grows, with all but one system accumulating between eighteen to twenty-eight pairs by the end of their simulation; in system 7, no event larger than 370 eV occurred, leaving only nine Frenkel pairs by 150 ps. The average number of Frenkel pairs remaining at the end of the simulations is 21.9±1.7, which equates to $2.9 \pm 2 \times 10^{-4}$ Frenekel pairs nm^{-3} per cascade. These ten simulations do not give us sufficient data to permit any remarks with regard to chromium defect behaviour in the simulation that would be statistically meaningful.

As intended with the MD timescale multiple event model, in these simulations, we did observe cascades occurring in overlapping volumes, and this was found in exactly half of the systems. Defining clusters as regions where multiple defects are found within 2.9 Å [5] of each other, and excluding examples where vacancy-interstitial pairs are on the verge of recombination, see figure 5.10, we find that in the systems without examples of overlapping cascades, fifteen clusters are seen, whereas in systems with overlapping cascades, twenty-five are observed.

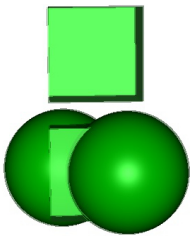

Figure 5.10: Vacancy and split-interstitial defects in close proximity. This Frenkel pair is close to recombination, and therefore these objects are excluded from the defect cluster count.

Taking a closer look at each of the overlapping events, we can make some remarks regarding the consequences for cascades that encounter existing damage:

[5] I.e. slightly larger than the lattice parameter, which in BCC systems is the second nearest neighbour distance.

- *System 5*: Event 14, with a PKA energy of 300 eV, has a cascade plume that encounters the interstitials left at the edge of the previous cascade, from event 13, which had a PKA energy 1370 eV. The plume does not extend beyond this point, and the interstitials it creates coalesce with those from the prior cascade to form a cluster, see figure 5.21.

- *System 6*: Event 4, with PKA energy of 2530 eV, totally engulfs the remaining damage from event 2, whose PKA energy was 300 eV. After the damage plume recedes, a cluster of interstitials is left in the approximate location of event 2, shifted in towards the position of event 4, see figure 5.22. Event 14, with PKA energy of 130 eV, also occurs in this region, and does not have a large effect on the existing defects, although the event's damage plume does not pass the existing damage it encounters.

- *System 8*: Event 2, with PKA energy of 2050 eV, creates a relativity isolated split-interstitial, and event 4, whose PKA energy was 150 eV, occurs in proximity to it, and the pre-existing defect is pushed aside by the later cascade, see figure 5.23. Note that the split-interstitial is composed of a different two atoms after the move.

- *System 9*: A replacement collision sequence from event 12, with PKA energy of 240 eV, passes through the volume which contained the damage plume from event 9, whose PKA energy was 90 eV. Within this region, it leaves a split-interstitial, which migrates towards vacancies left by event 9, see figure 5.24.

- *System 10*: The events 4 and 7, of PKA energies 140 eV and 100 eV respectively, both create only one Frenkel pair each. Over the course of the simulation, these interstitial defects meet and form a cluster, see figure 5.25.

These results show that when cascades occur in proximity to existing damage, the formation of defect clusters is promoted. In a real experiment or reactor, the long time-spans between cascade events will allow the annealing of damage, and thus the density of defects will be reduced. However, this will also allow isolated defects to spread more evenly through the lattice, and allow defects in proximity to each other to coalesce. Assuming that damage

is accumulated faster than the rate of recombination, the probability of a cascade event intersecting existing damage will rise as the total time of radiation exposure progresses, and as such, the clustering of defects will also increase.

5.4 Chapter Conclusions

In this chapter, we attempted to apply our atomistic modelling methods to create an analogue of an experimental system. To bridge the gap between the given proton radiation environment to which the material samples were exposed, and the simulation of collision cascades, we turned to the SRIM package. This estimated the number of events per incident proton as a function of depth, and provided a distribution for the energy exchanged in those events. This data, combined with the number of protons delivered per unit time, was used to construct a model in which collision cascades of PKA energy selected randomly from said distribution were simulated through Molecular Dynamics, followed by the simulation of the annealing of the resulting damage (if any) via Adaptive Kinetic Monte Carlo. The largest PKA energy permitted in the model was 5 keV and to contain an event of this size required a simulation cell with 432,000 atoms; however, low energy events, which create small cascade plumes and few Frenkel pairs, dominate the spectrum of event energies. As such, we did not encounter any examples of cascades intersecting the volume in which prior cascades had occurred, nor interacting with their pre-existing damage, if still present. With a new cascade event being initiated only once every 2.70 seconds on average, we were unable to achieve sufficiently long timescales to overcome this problem. Thus, we switched to introducing a new cascade at the immediate conclusion of the MD simulation, using the same event energy spectra as before, but neglecting any simulation of the recovery period previously attempted with AKMC. Therefore, these systems experienced an event every 10 ps, with a total of fifteen cascades simulated per system, and these models gave us the opportunity to examine overlapping cascade phenomena. As well as a greater tendency for clusters to form when events occurred overlapping or in proximity to prior cascade plumes, interstitial

damage engulfed by a cascade is seen to re-emerge when the plume recedes. Additionally, while pre-existing defects may be displaced to adjacent lattice sites by a later event, they appear to contribute to containing the maximum extent of cascade plumes.

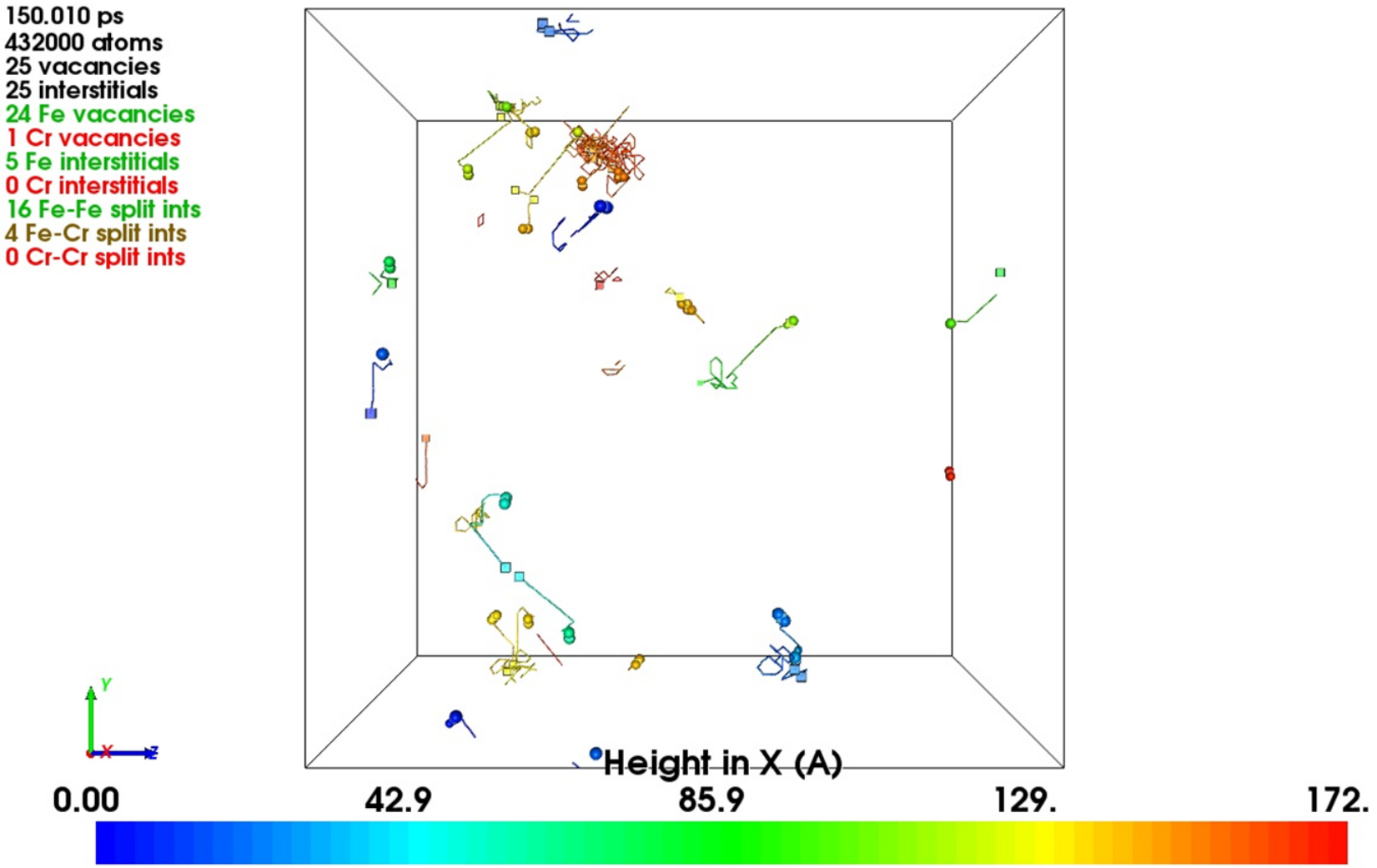

Figure 5.11: Visualisation of an $FeCr_{10\ at.\%}$ lattice (system 1) of 432,000 atoms, after the simulation of fifteen collision cascades via Molecular Dynamics, with an event beginning every 10 ps. The PKA energies, see table 5.2, were selected randomly, as per the distribution seen in figure 5.5. Off lattice atoms are visualised as spheres and lattice vacancies are shown as cubes. The lines seen on the image depict defect replacement chains. Colour is used to represent depth into the simulation cell, as seen head on.

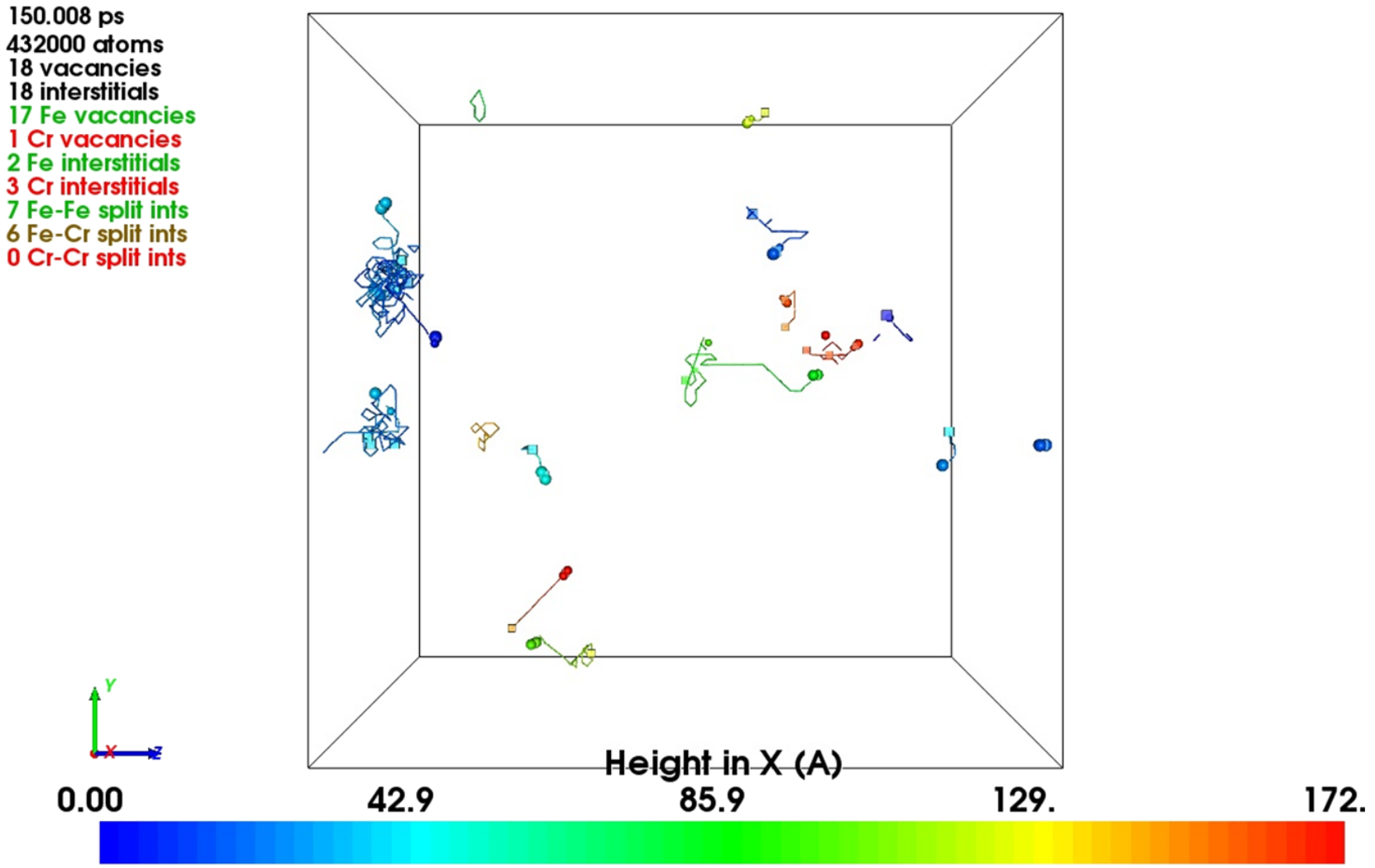

Figure 5.12: Visualisation of an $FeCr_{10\ at.\%}$ lattice (system 2) of 432,000 atoms, after the simulation of fifteen collision cascades via Molecular Dynamics, with an event beginning every 10 ps. The PKA energies, see table 5.2, were selected randomly, as per the distribution seen in figure 5.5. Off lattice atoms are visualised as spheres and lattice vacancies are shown as cubes. The lines seen on the image depict defect replacement chains. Colour is used to represent depth into the simulation cell, as seen head on.

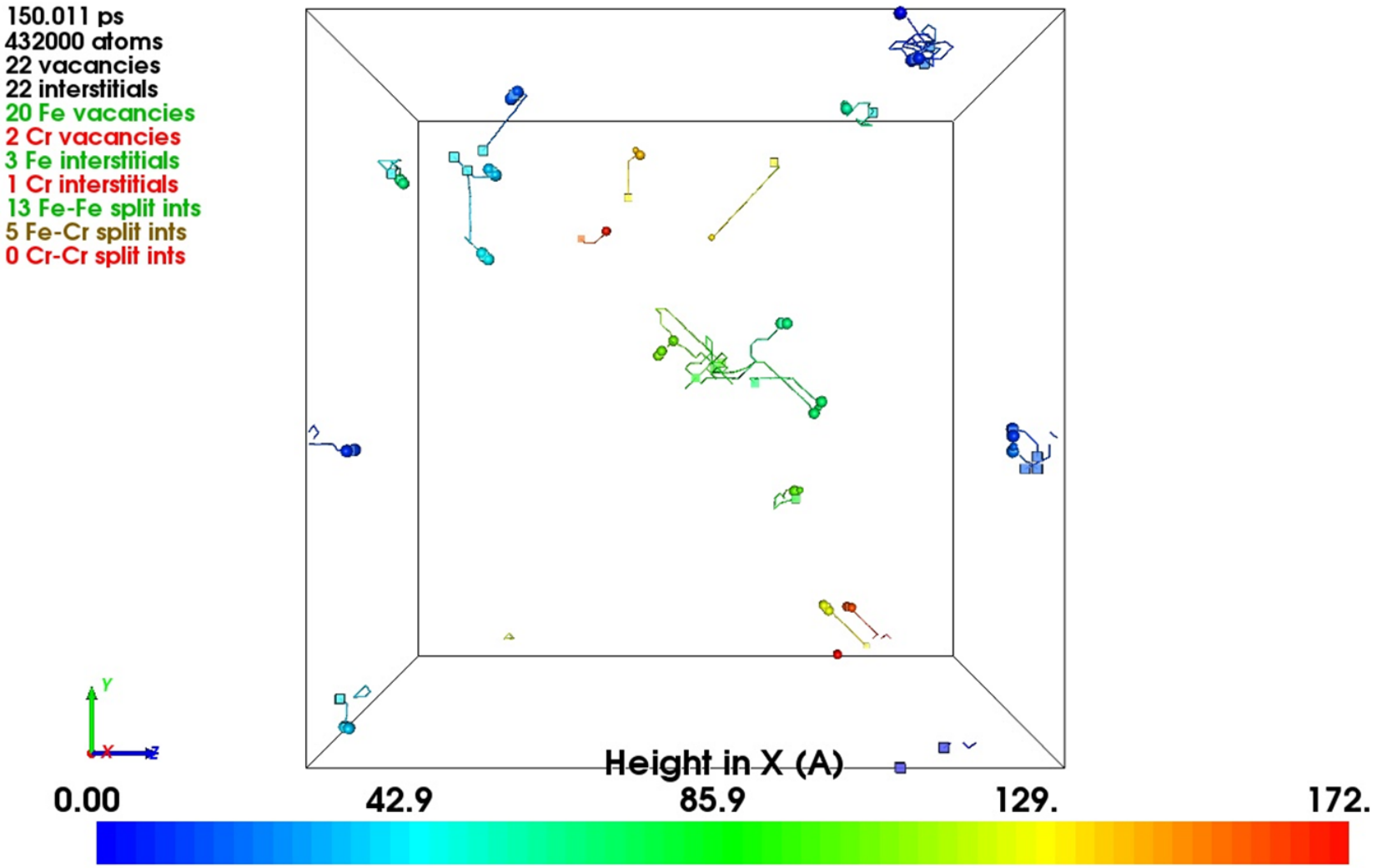

Figure 5.13: Visualisation of an $FeCr_{10\ at.\%}$ lattice (system 3) of 432,000 atoms, after the simulation of fifteen collision cascades via Molecular Dynamics, with an event beginning every 10 ps. The PKA energies, see table 5.2, were selected randomly, as per the distribution seen in figure 5.5. Off lattice atoms are visualised as spheres and lattice vacancies are shown as cubes. The lines seen on the image depict defect replacement chains. Colour is used to represent depth into the simulation cell, as seen head on.

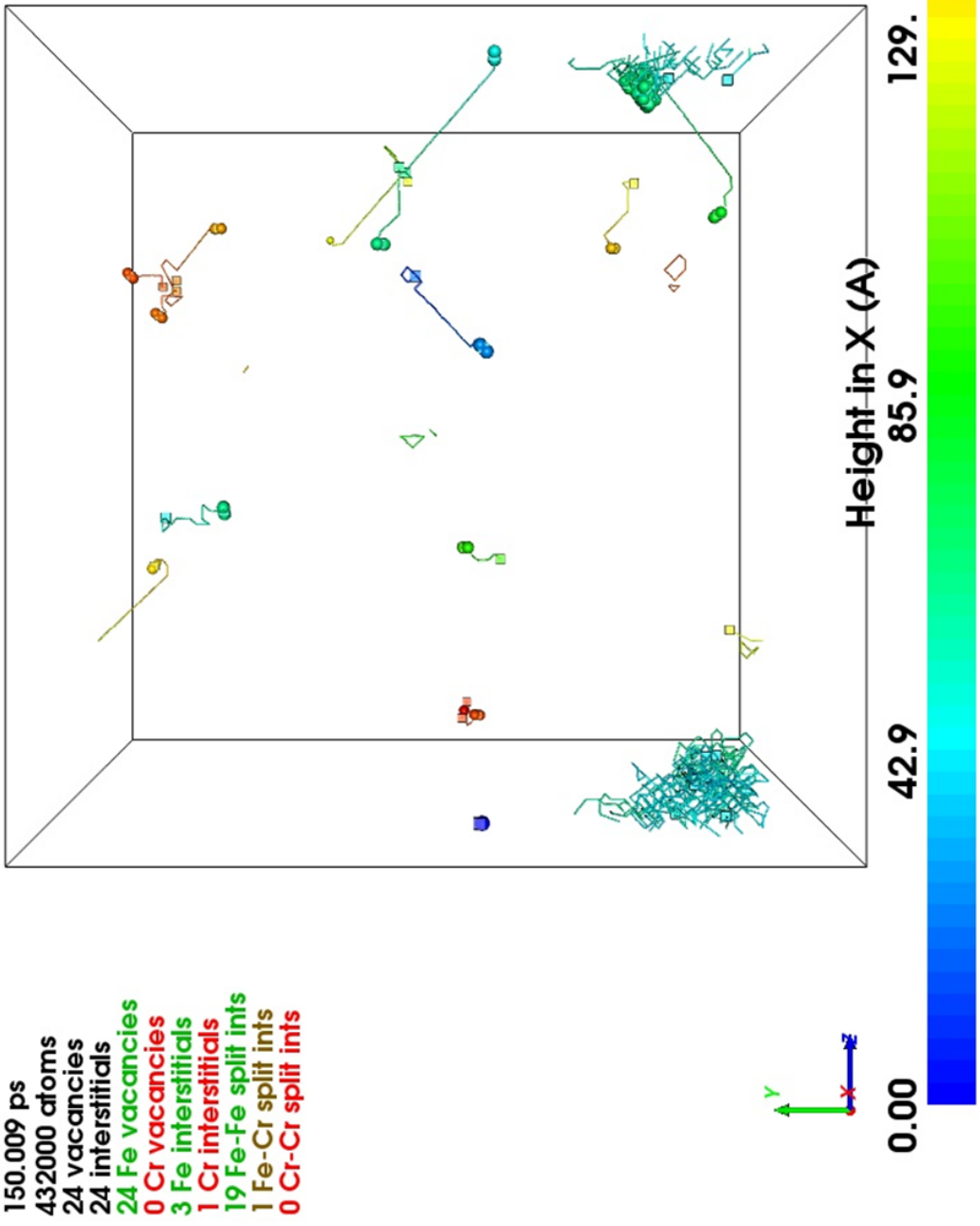

Figure 5.14: Visualisation of an $FeCr_{10\,at.\%}$ lattice (system 4) of 432,000 atoms, after the simulation of fifteen collision cascades via Molecular Dynamics, with an event beginning every 10 ps. The PKA energies, see table 5.2, were selected randomly, as per the distribution seen in figure 5.5. Off lattice atoms are visualised as spheres and lattice vacancies are shown as cubes. The lines seen on the image depict defect replacement chains. Colour is used to represent depth into the simulation cell, as seen head on.

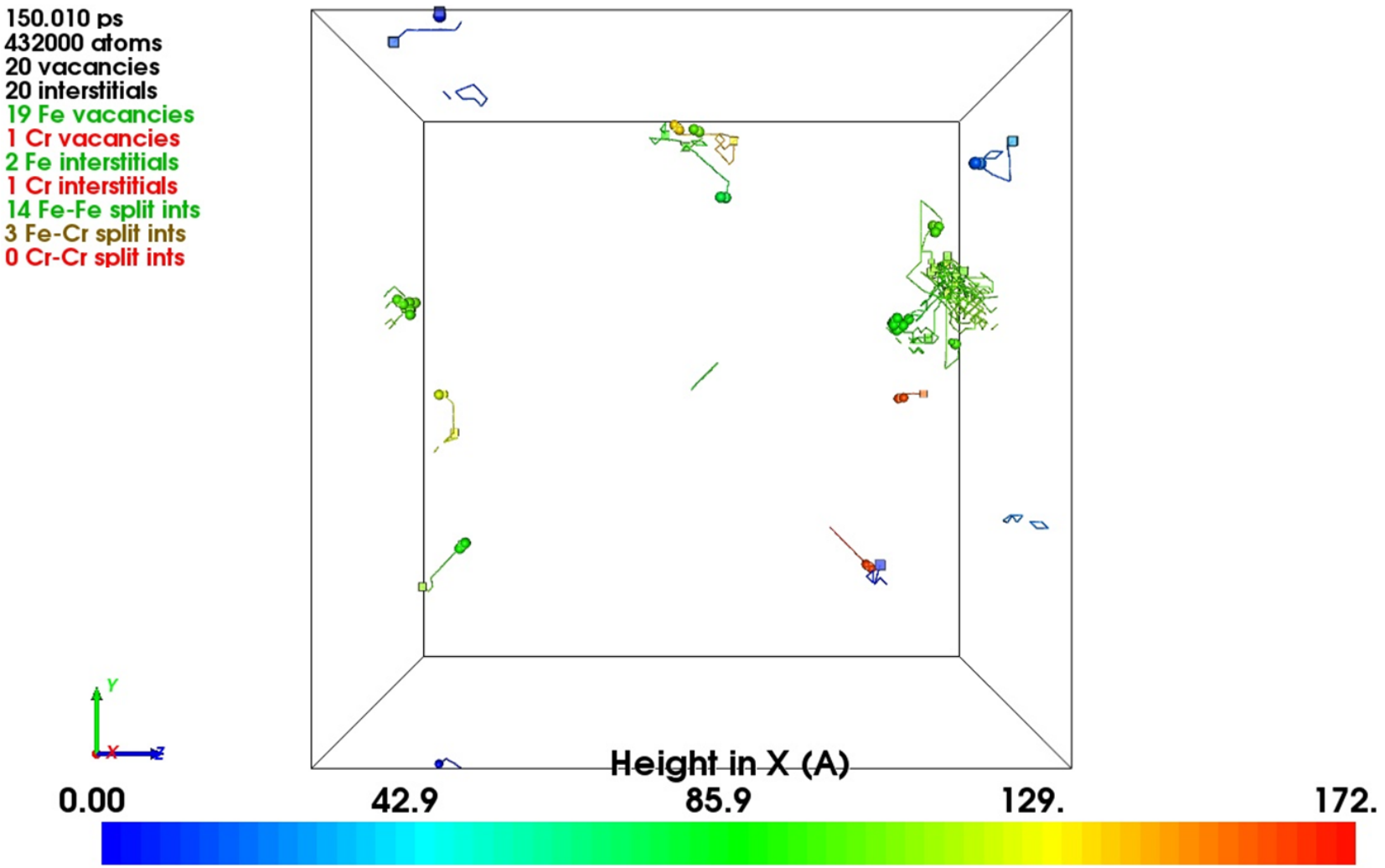

Figure 5.15: Visualisation of an $FeCr_{10\ at.\%}$ lattice (system 5) of 432,000 atoms, after the simulation of fifteen collision cascades via Molecular Dynamics, with an event beginning every 10 ps. The PKA energies, see table 5.2, were selected randomly, as per the distribution seen in figure 5.5. Off lattice atoms are visualised as spheres and lattice vacancies are shown as cubes. The lines seen on the image depict defect replacement chains. Colour is used to represent depth into the simulation cell, as seen head on.

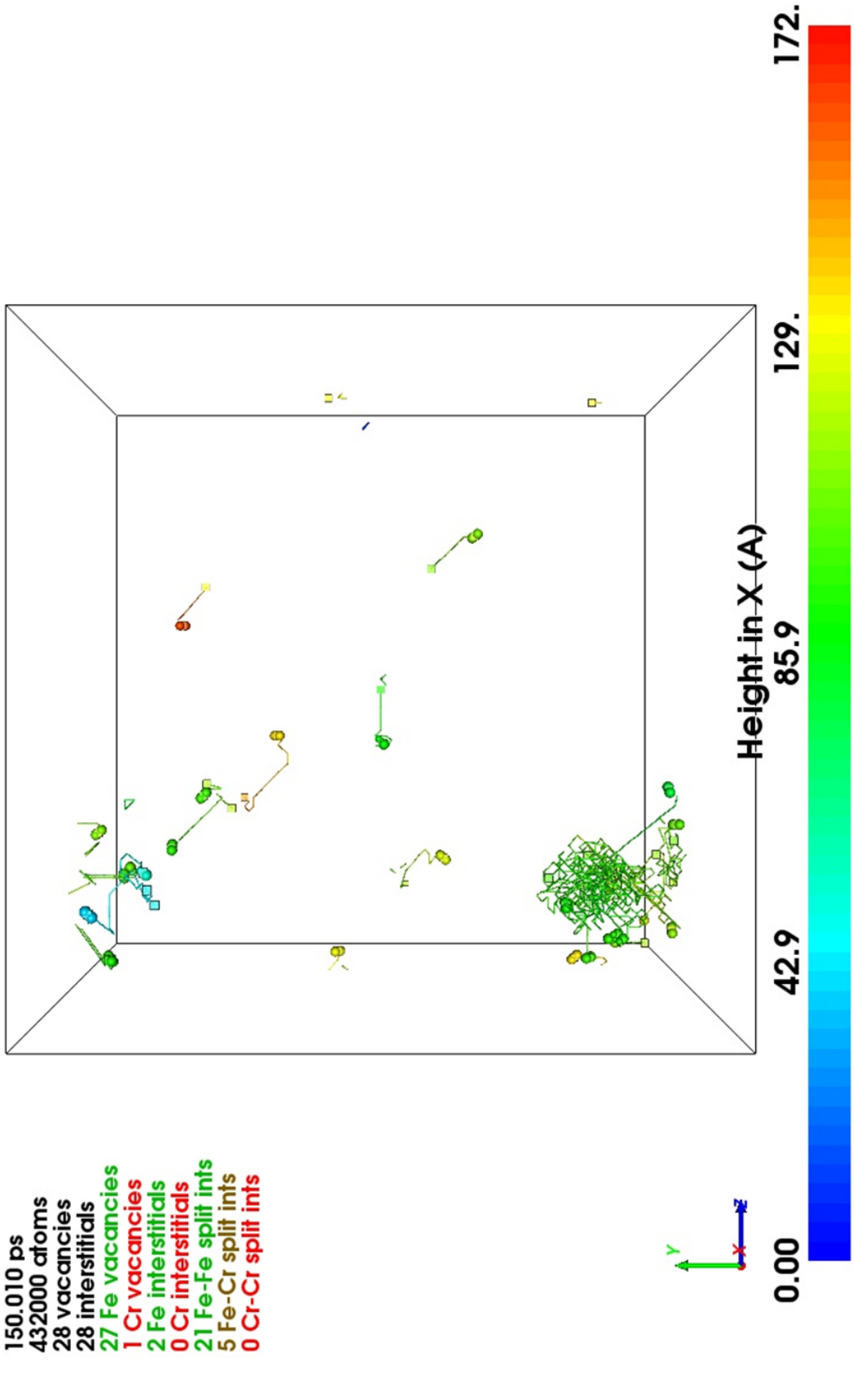

Figure 5.16: Visualisation of an $FeCr_{10\,at.\%}$ lattice (system 6) of 432,000 atoms, after the simulation of fifteen collision cascades via Molecular Dynamics, with an event beginning every 10 ps. The PKA energies, see table 5.2, were selected randomly, as per the distribution seen in figure 5.5. Off lattice atoms are visualised as spheres and lattice vacancies are shown as cubes. The lines seen on the image depict defect replacement chains. Colour is used to represent depth into the simulation cell, as seen head on.

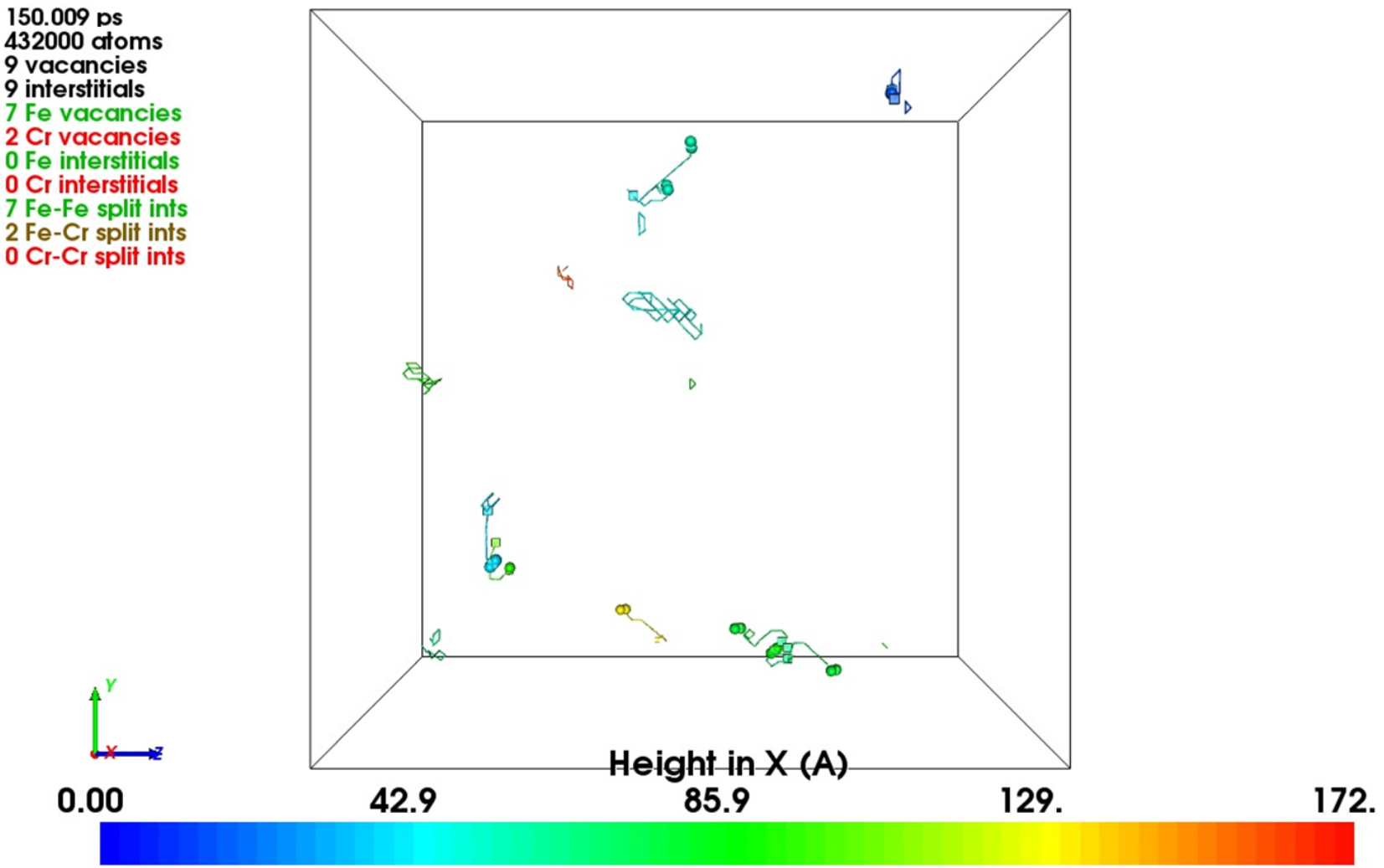

Figure 5.17: Visualisation of an $FeCr_{10\ at.\%}$ lattice (system 7) of 432,000 atoms, after the simulation of fifteen collision cascades via Molecular Dynamics, with an event beginning every 10 ps. The PKA energies, see table 5.2, were selected randomly, as per the distribution seen in figure 5.5. Off lattice atoms are visualised as spheres and lattice vacancies are shown as cubes. The lines seen on the image depict defect replacement chains. Colour is used to represent depth into the simulation cell, as seen head on.

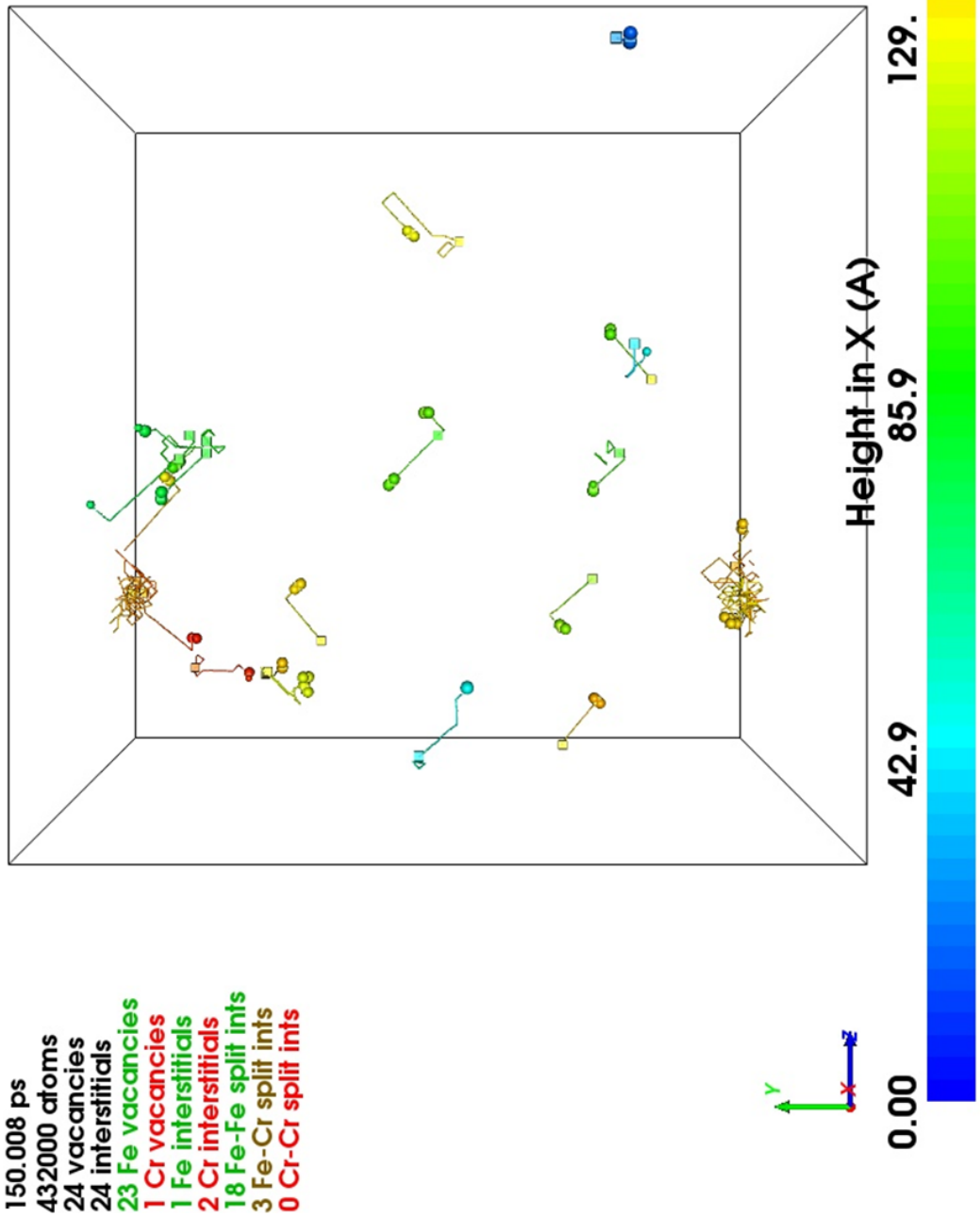

Figure 5.18: Visualisation of an $FeCr_{10\,\text{at.}\%}$ lattice (system 8) of 432,000 atoms, after the simulation of fifteen collision cascades via Molecular Dynamics, with an event beginning every 10 ps. The PKA energies, see table 5.2, were selected randomly, as per the distribution seen in figure 5.5. Off lattice atoms are visualised as spheres and lattice vacancies are shown as cubes. The lines seen on the image depict defect replacement chains. Colour is used to represent depth into the simulation cell, as seen head on.

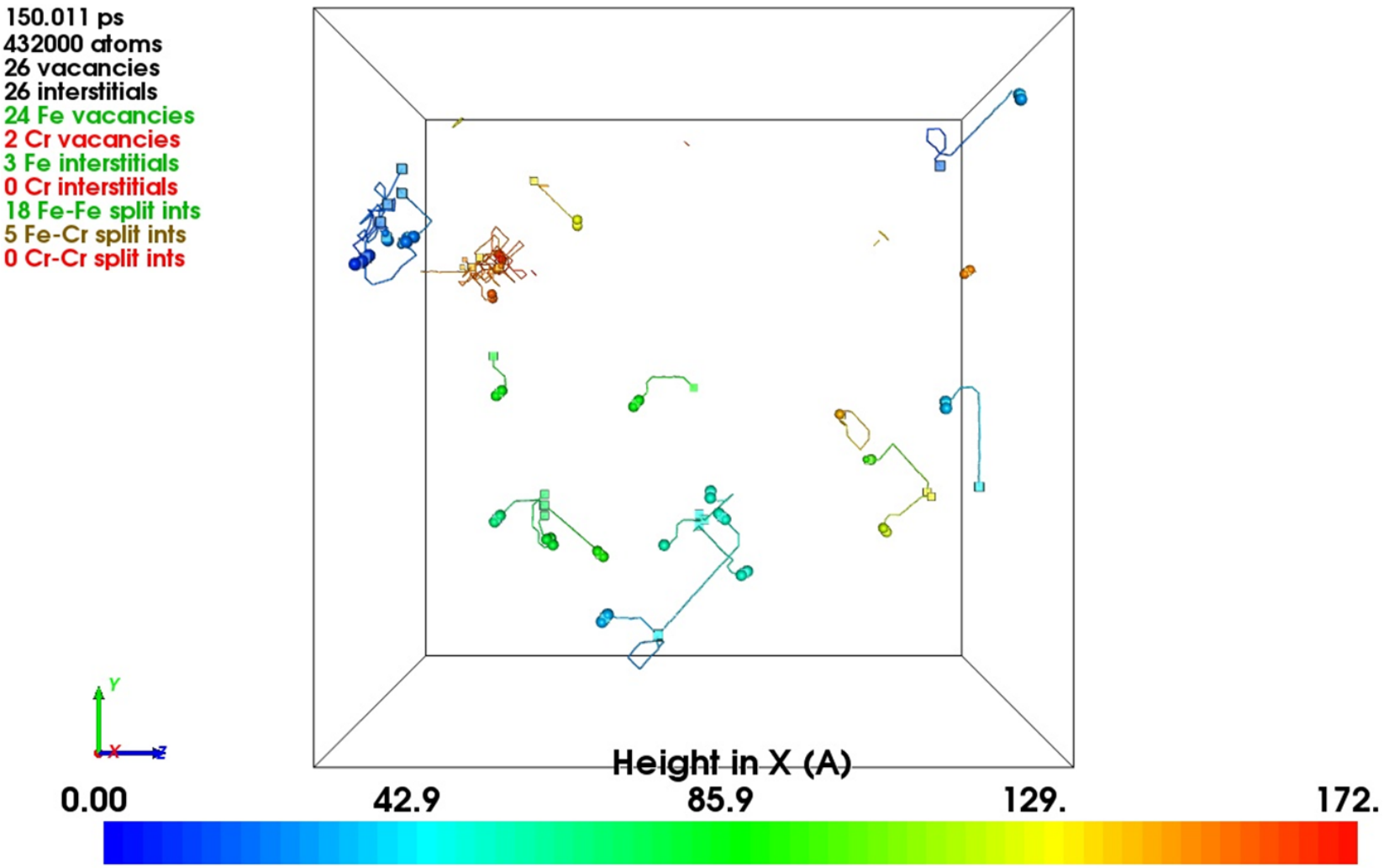

Figure 5.19: Visualisation of an $FeCr_{10\ at.\%}$ lattice (system 9) of 432,000 atoms, after the simulation of fifteen collision cascades via Molecular Dynamics, with an event beginning every 10 ps. The PKA energies, see table 5.2, were selected randomly, as per the distribution seen in figure 5.5. Off lattice atoms are visualised as spheres and lattice vacancies are shown as cubes. The lines seen on the image depict defect replacement chains. Colour is used to represent depth into the simulation cell, as seen head on.

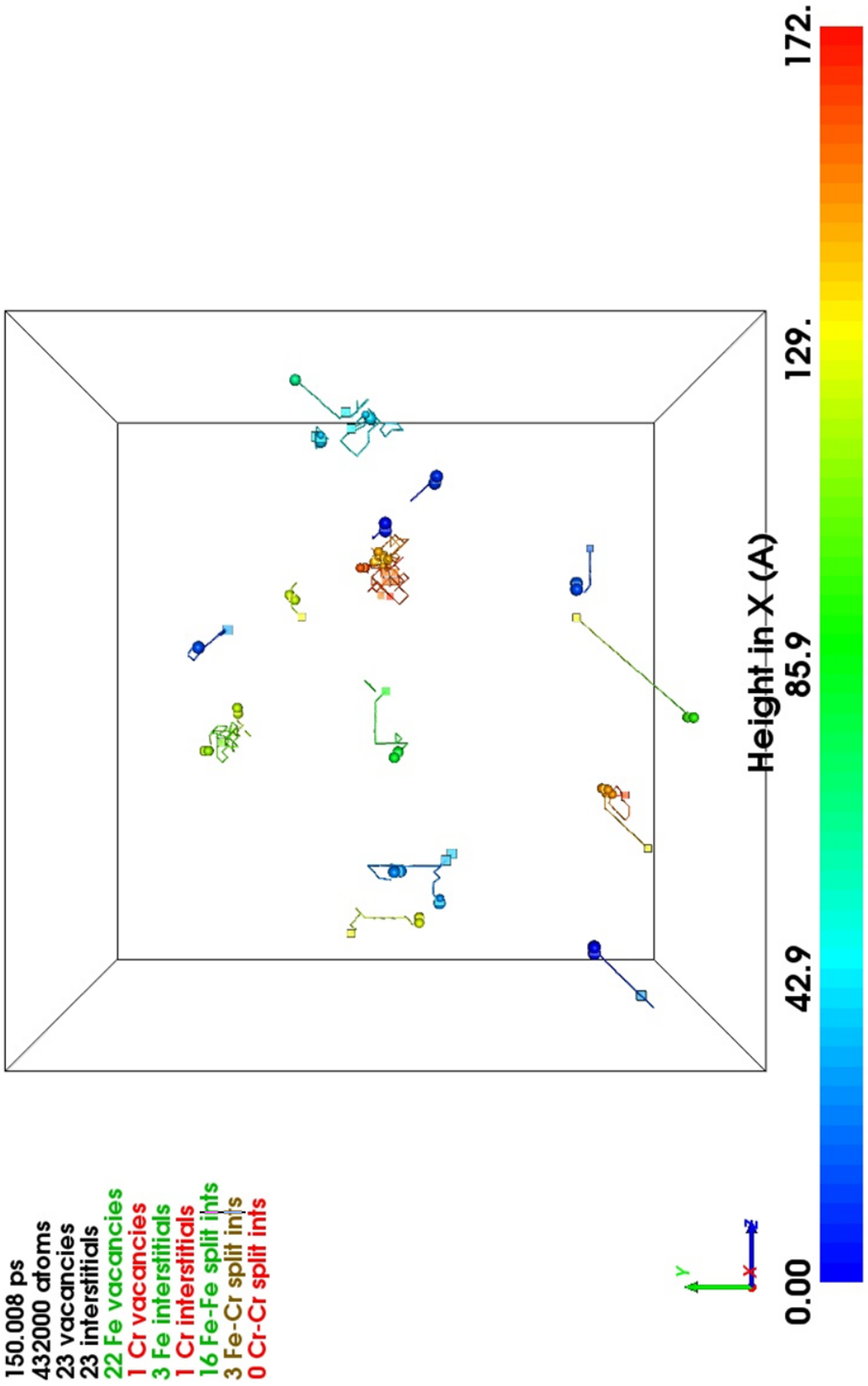

Figure 5.20: Visualisation of an $FeCr_{10\,\mathrm{at.\%}}$ lattice (system 10) of 432,000 atoms, after the simulation of fifteen collision cascades via Molecular Dynamics, with an event beginning every 10 ps. The PKA energies, see table 5.2, were selected randomly, as per the distribution seen in figure 5.5. Off lattice atoms are visualised as spheres and lattice vacancies are shown as cubes. The lines seen on the image depict defect replacement chains. Colour is used to represent depth into the simulation cell, as seen head on.

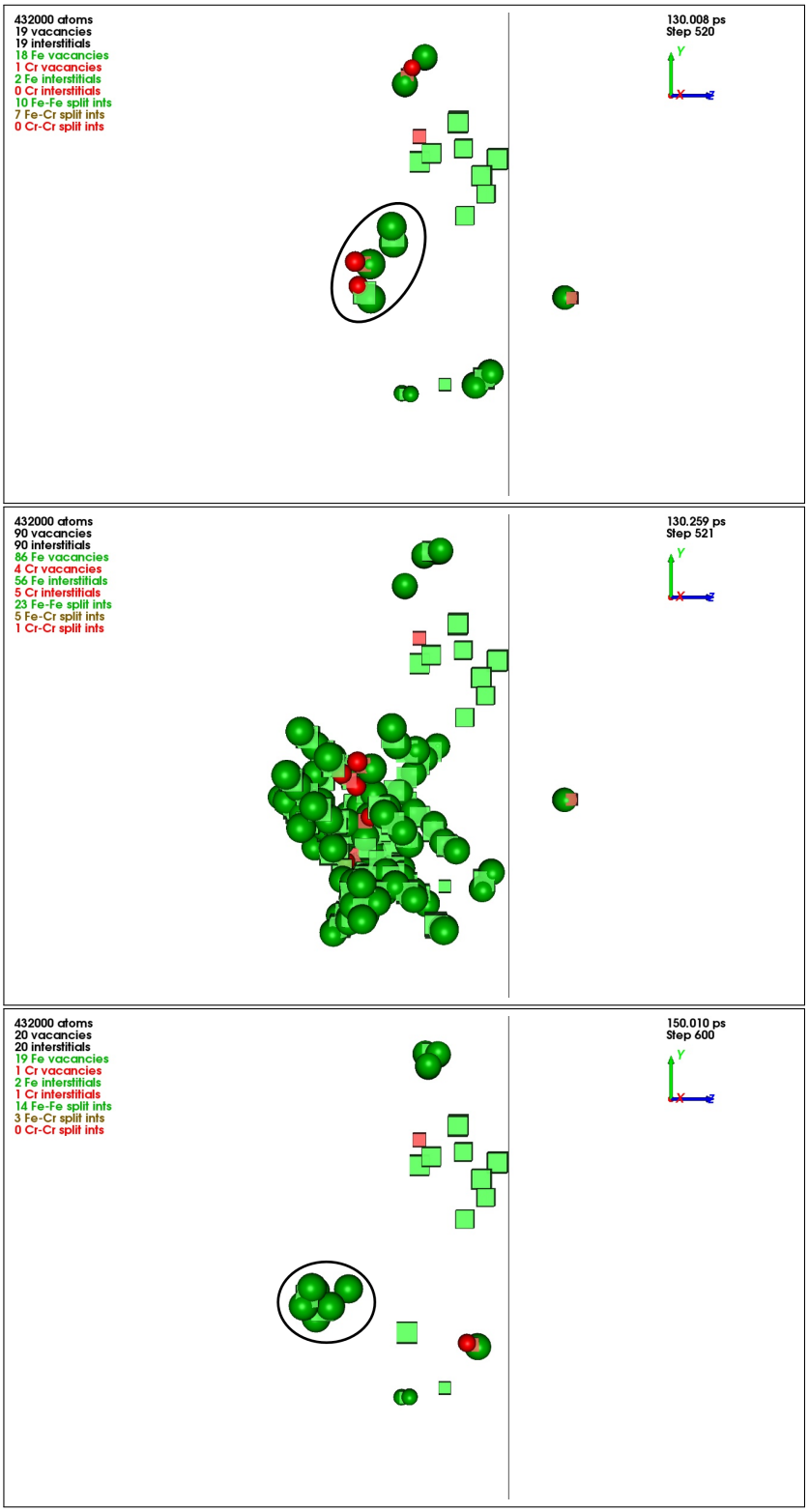

Figure 5.21: In system 5, events 13 and 14, with PKA energies of 1370 eV and 300 eV respectively, occur close to each other in the lattice. The latter cascade brings its new and existing interstitial atoms into a cluster. For a complete summary of events in this system, see table 5.2. Interstitial atoms are visualised as spheres, red for iron, green for chromium, and vacant lattice sites are represented as cubes, with on-lattice atoms being hidden.

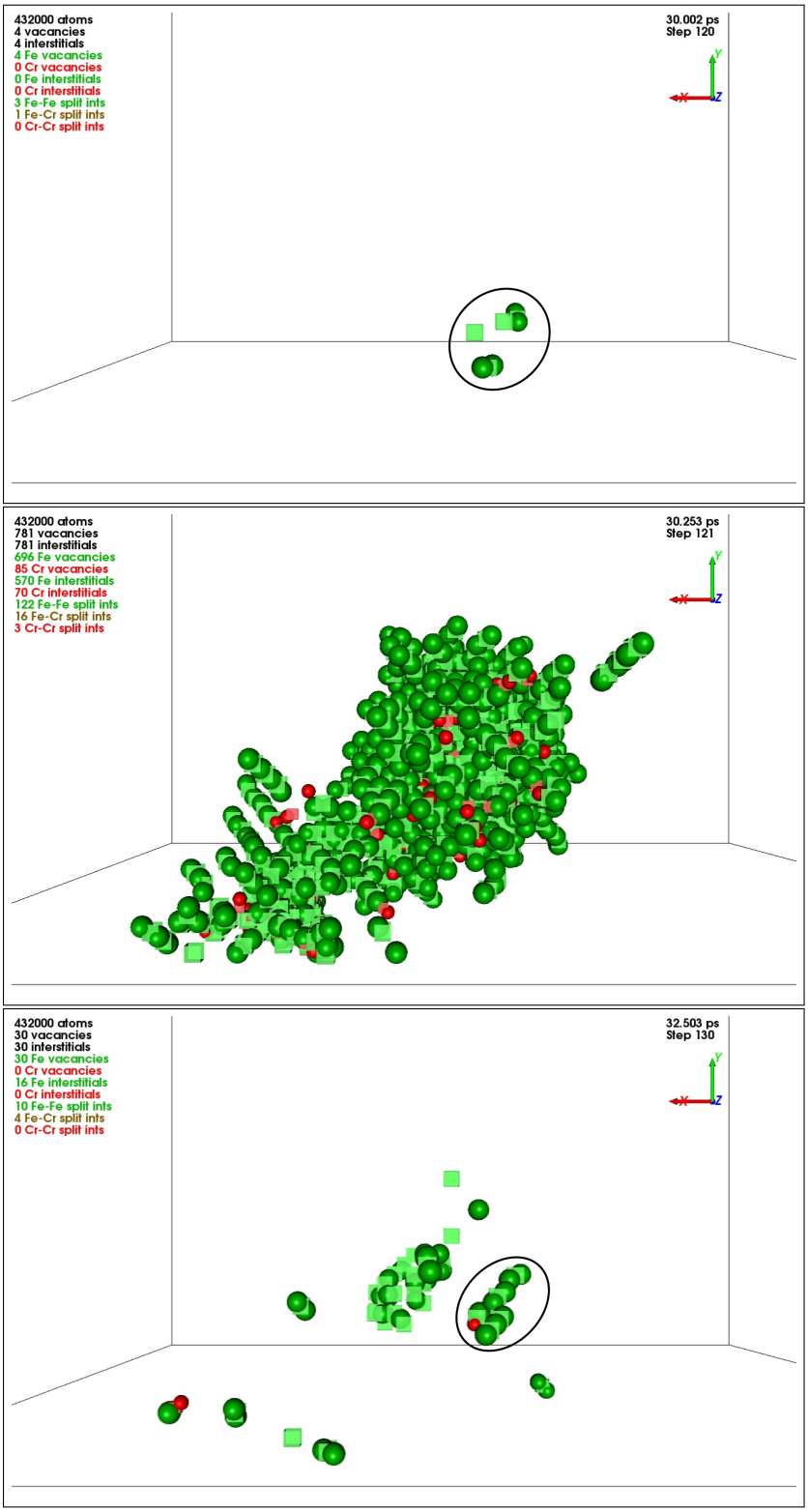

Figure 5.22: In system 6, event 4, with PKA energy 2530 eV, totally envelopes the damage remaining from the 300 eV cascade from event 2. After event 4's plume of damage recedes, a cluster of interstitial defects is left where the expanding region of new damage met the existing lattice defects. The damage before and after event 4 is circled in black. For a complete summary of events in this system, see table 5.2. Interstitial atoms are visualised as spheres, red for iron, green for chromium, and vacant lattice sites are represented as cubes, with on-lattice atoms being hidden.

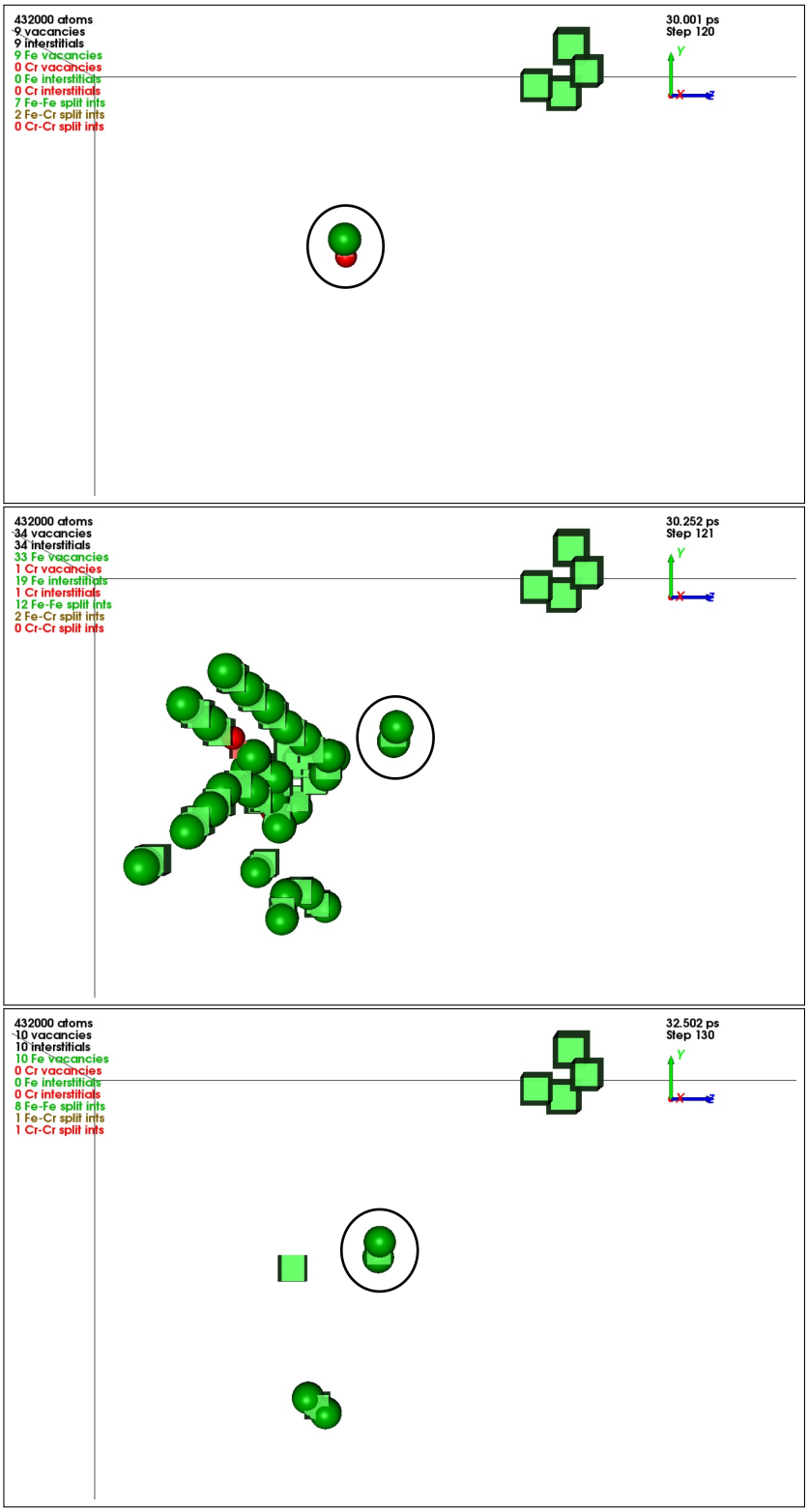

Figure 5.23: In system 8, the isolated split-interstitial left by PKA event 2, with PKA energy 2050 eV, is pushed over, by event 4, with PKA energy of 150 eV. After event 4, the split-interstitial, circled in black, shift back towards its original position, although its net motion is still to the right, from viewing angle of this image. For a complete summary of events in this system, see table 5.2. Interstitial atoms are visualised as spheres, red for iron, green for chromium, and vacant lattice sites are represented as cubes, with on-lattice atoms being hidden.

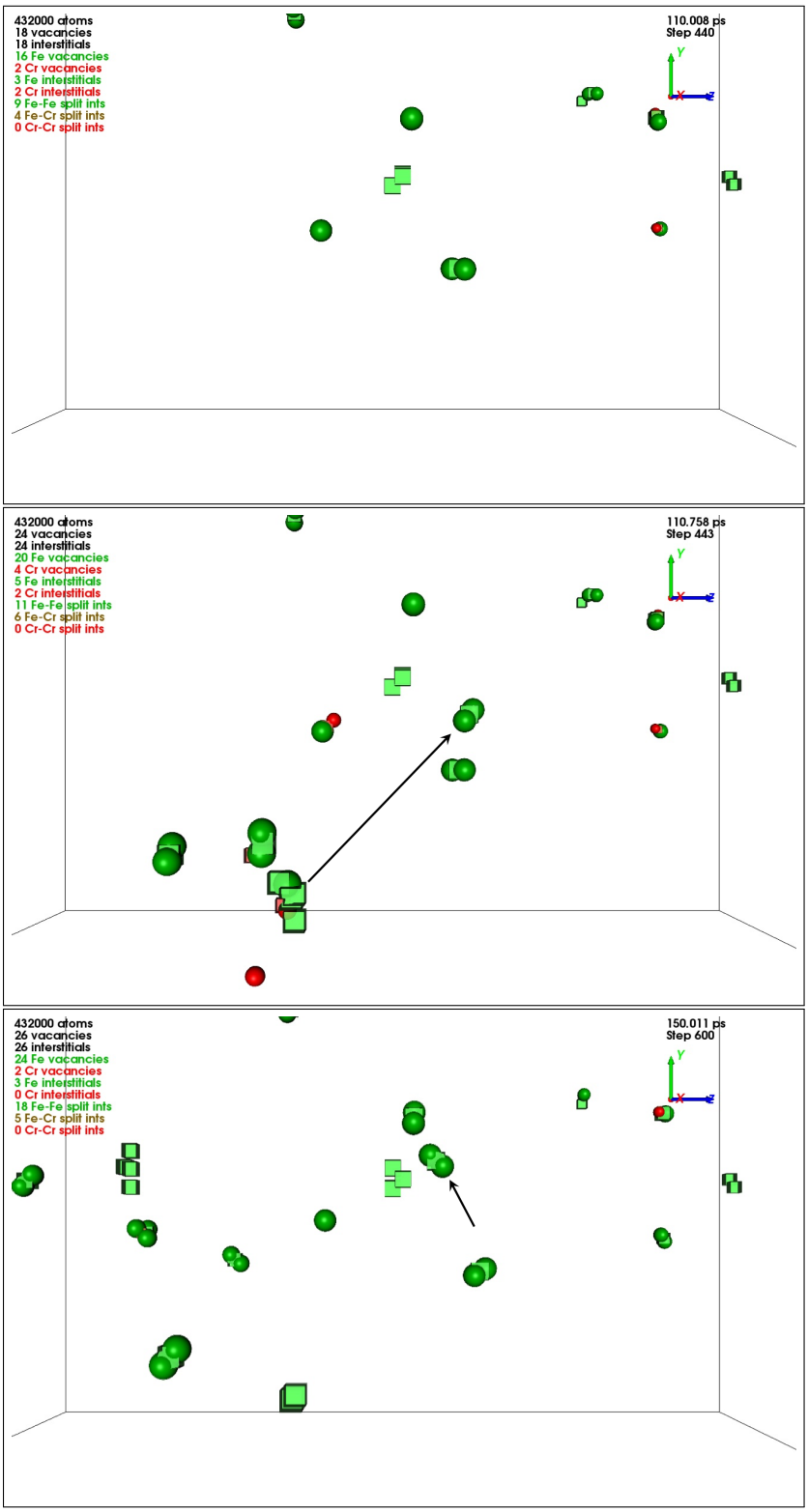

Figure 5.24: In system 9, a split-interstitial ejected by event 7, with PKA energy of 100 eV is left in proximity to the damage left by event 4, whose PKA energy was 140 eV, and over the rest of the simulation, it begins to migrate towards the vacancy cluster resulting from event 4, as depicted by the arrows. For a complete summary of events in this system, see table 5.2. Interstitial atoms are visualised as spheres, red for iron, green for chromium, and vacant lattice sites are represented as cubes, with on-lattice atoms being hidden.

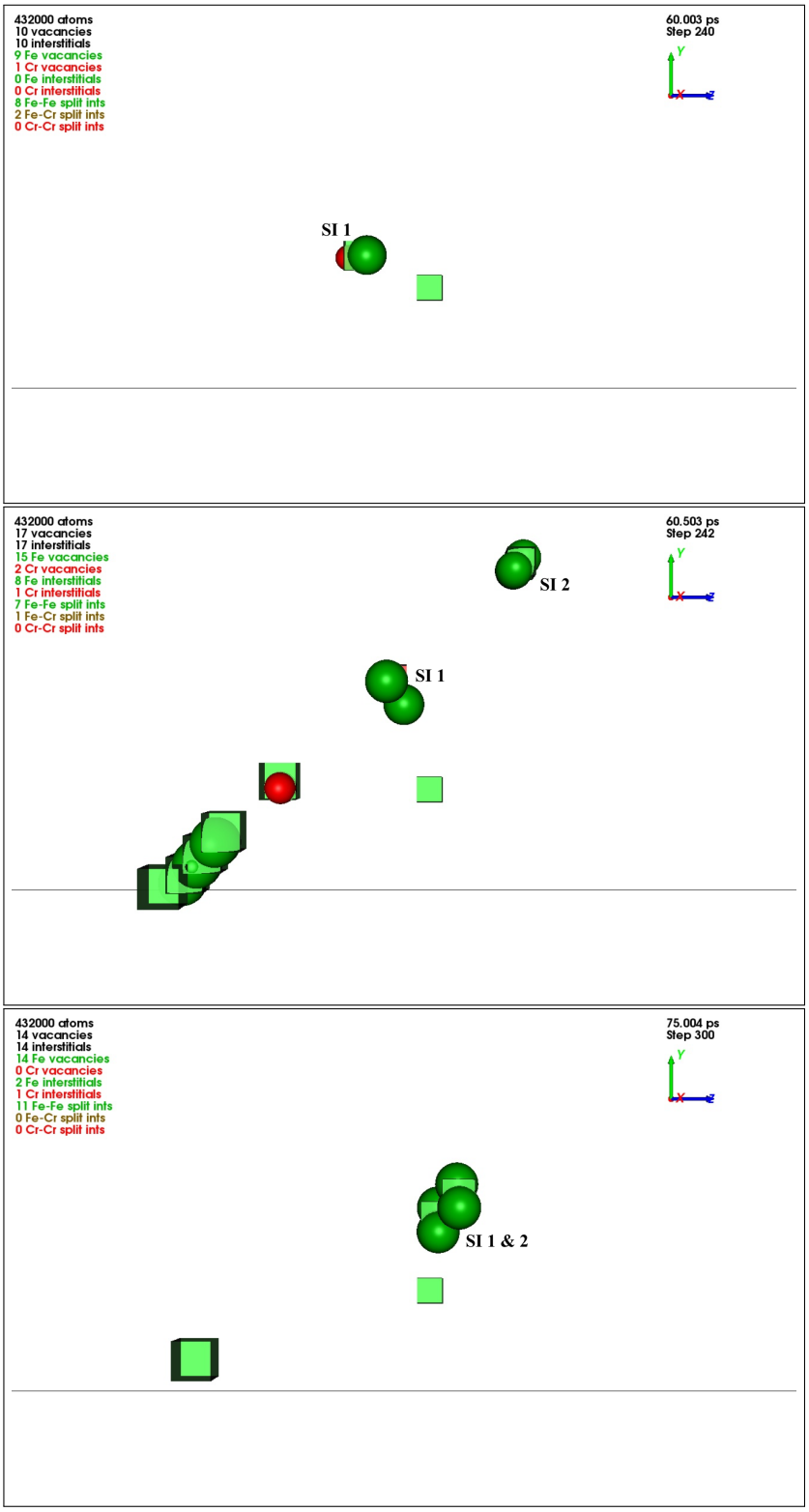

Figure 5.25: In system 10, damage is created by events 4 and 7, with PKA energies 140 eV and 100 eV, leaving two split interstitials in proximity, labelled SI 1 and SI 2. These migrate closer still to each other, eventually forming a cluster. For a complete summary of events in this system, see table 5.2. Interstitial atoms are visualised as spheres, red for iron, green for chromium, and vacant lattice sites are represented as cubes, with on-lattice atoms being hidden.

Chapter 6

Conclusions

6.1 Summary

In a world with an ever-growing demand for energy, the need for reliable materials with which to construct the next generation of nuclear power plants, becomes evermore vital as existing installations' operational lifespans expire. In this work, we used atomistic modelling techniques to simulate the production of radiation induced damage to BCC iron and iron-chromium binary alloys by way of collision cascade sequences, and to examine the subsequent migration and annihilation of interstitial defects. High purity iron-chromium binary alloys are of considerable interest to future nuclear construction applications, being relatively inexpensive, resistant to oxidation, and having demonstrated resilience to radiation in experimental studies.

To accomplish this we implemented an Fe-Cr interatomic potential [67, 68] to be called by our in-house Molecular Dynamics and Adaptive Kinetic Monte Carlo routines, LBOMD and LAKMC, as well as revamping features of the latter to include integrated Molecular Dynamics events and an improved execution of the Superbasin method [97, 107, 108].

Given that much of the literature focuses on cascades with PKA energies above 5 keV, and that large collision sequences can be considered as a series of subcascades, our simulations were conducted with PKAs with kinetic energetics of 1, 2, and 5 keV, and the lattices

modelled ranged between 0 and 10 at.% bulk chromium concentration. Simulations with a range of PKA energies were conducted at 0 Kelvin in $FeCr_{10\ at.\%}$ systems, and simulations with 1 keV PKAs were conducted at 500 Kelvin for Fe, $FeCr_{1\ at.\%}$, $FeCr_{5\ at.\%}$, and $FeCr_{10\ at.\%}$ systems.

Over the range of PKA energies studied, we found the number of Frenkel pairs produced to be linear, although this must break down at lower energies. Simulating at 500 Kelvin resulted in a modest reduction in defect production compared to the 0 Kelvin simulation, however chromium was under-represented in defect atoms in the latter, and by contrast, the simulations at the higher temperature produced the reverse. The variation of PKA energy in the low temperature simulations did not have an appreciable effect on chromium under/over-representation. In the high temperature cascades, varying the bulk concentration of chromium made no measurable difference to Frenkel pair production whatsoever, but the over-representation of chromium was considerably more pronounced at low concentration.

With the simulations conducted at higher temperature, we found that greater care is necessary when relaxing the post-cascade lattices. L-BFGS-B/CG minimisation, appeared to distort the results, so the more robust damped MD was applied to analyse this data. To a lesser extent, similar distortions were seen in the results conducted at 0 Kelvin, with these lattices already being closer to a relaxed state after a cascade due to their lower thermal vibration. The use of damped MD was applied sparingly due to the much high computation cost associated. Regardless of minimisation technique used, a reduction in the less stable lone interstitial defects, and a modest fall in Frenkel pairs, was seen.

Considering the concept of displacement threshold energy, we simulated the displacement of iron and chromium atoms in $FeCr_{10\ at.\%}$ systems, by upto 240 and 140 eV, respectively, and recorded the number of systems with off lattice atoms after 10 ps. Contrary to the aforementioned concept, a sharp threshold hold between displacement and non-displacement was not observed; however, the percentage of systems in which damage was successfully created did rise rapidly from 0 to 40 eV, before the trend flattened. For both atomic species,

the point at which damage was successfully produced in half of the systems was close to 55 eV.

Many computational studies will use a representative vector to collect statistics with small error bars, with lower expenditure of CPU hours, and to this end, $\langle 1\ 3\ 5 \rangle$, is a common choice. Having conducted our main simulations using even samples of the unit sphere, we ran simulations with only these PKA vectors to examine if any bias was introduced – no significant difference in Frenkel pair production was seen; however, the over-representation of chromium seen was massively exaggerated, and in papers using the $\langle 1\ 3\ 5 \rangle$ PKA vectors, this behaviour was also observed [39,47]. As such, we caution against its use when resources permit.

Using AKMC, we simulated the post-cascade migration of defects in $FeCr_{10\ at.\%}$ systems after a 1 keV event. Unsurprisingly, correlation between system energy loss and number of Frenkel pair recombinations, and between time and number of Frenkel pair recombinations, was observed. Only one of the systems fully annealed, doing so in 6 μs, falling in potential energy by 49.2 eV (9.11×10^{-4} eV per atom), having begun with seven Frenkel pairs. Visual inspection indicates that during the migration process, interstitial defects tend to form non-permanent clusters, while examples of vacancies aligning along adjacent sites is also seen. Potential energy hypersurface transition searches applied to single defects were suggestive of greater defect mobility in $FeCr_{10\ at.\%}$ by comparison to pure iron.

A study of the energies of the cascade events in $FeCr_{10\ at.\%}$ produced by protons, conducted via SRIM, found the overwhelming majority of interactions fall at the low magnitude end of the scale. This data was used to simulate systems experiencing a series of successive events, such as to be physically representative of a real experimental set-up, but the large lattices that this necessitated made the recovery process prohibitively slow.

Foregoing the recovery time, we simulated successive cascades every 10 ps, producing 1.46 ± 0.11 Frenkel pairs per event, and giving us the opportunity to observe the production of damage in regions intersecting that from prior events. Clustering is more prominent when

events overlap, and within the 150 ps simulation timescale, damage from separate events is seen to coalesce.

6.2 Recommendations for Future Work

As the final remarks made in this work, the author would like to make a series of suggestions for anyone who may wish to continue this research.

- Expand the range of PKA energies to include larger cascades. These events are rare, but should provide the opportunity to observe cascade-splitting. When we collected data on event energies from SRIM, that data includes secondary atom displacements, and it would be of interest to consider how these evolve in the more detailed MD regime. Note that a normal EAM potential becomes unsuitable when very high cascade energies are involved, and an approach that considers separate energy lost to nuclei and electrons separately is required [53].

- In all our simulations, chromium was evenly randomly distributed amongst the iron atoms. Given that the energetics of iron-chromium interaction favours segregation, there may be merit in experimentation with non-even distributions.

- As seen in figure 1.1, there is a very broad range of temperatures at which a reactor might operate. An expansion of this work could be to repeat the computational experiments with a broader range of temperatures.

- The overlapping cascade effects that we were able to study were dependant on the placement of randomly selected primary knock-on atoms. We would suggest a study of overlapping collision cascade volumes conducted in a more controlled manner. Generate lattices in which two events are simulated, observing the effects of the relative initial PKA locations on the cascades, varying the separation between that required for total overlap and total non-overlap.

- Investigate if there are any other bias introducing practices common in atomistic modelling, aside from that of the use of $\langle 1\ 3\ 5 \rangle$ PKA vectors.

- It would be of interest to compare the migration behaviour of defects during our AKMC simulations to similar systems at different temperatures and concentrations of chromium.

- Compare proton event energy spectrum with that of heavy and light ions. Third party extensions exist to allow SRIM to simulate neutrons, but we encountered a paywall when attempting to access them [117]. Similarly, SRIM cannot model electron irradiation without external assistance.

Chapter 7

References

[1] IAEA. PRIS - Miscellaneous reports - Operational by Age. *https://www.iaea.org/PRIS/WorldStatistics/OperationalByAge.aspx*, November 2016.

[2] World Nuclear Association. Nuclear Power in the United Kingdom | UK Nuclear Energy. *http://www.world-nuclear.org/info/Country-Profiles/Countries-T-Z/United-Kingdom*, October 2016.

[3] P. Yvon and F. Carré. Structural materials challenges for advanced reactor systems. *Journal of Nuclear Materials*, 385:217–222, 2009.

[4] H. Tanigawa, K. Shiba, A. Möslang, R. E. Stoller, R. Lindau, M. A. Sokolov, G. R. Odette, R. J. Kurtz, and S. Jitsukawa. Status and key issues of reduced activation ferritic/martensitic steels as the structural material for a DEMO blanket. *Journal of Nuclear Materials*, 417:9–15, 2011.

[5] Was *et al.*. *MRS Bulletin*, 2009.

[6] Gary S. Was. *Fundamentals of Radiation Materials Science – Metals and Alloys*. Springer-Verlag Berlin Heidelberg, 2007.

[7] Jannelle P. Wharry and Gary S. Was. A systematic study of radiation-induced segregation in ferritic-martensitic alloys. *Journal of Nuclear Materials*, 442:7–16, 2013.

[8] Ronald L. Klueh and Donald R. Harries. *High-chromium ferritic and martensitic steels for nuclear applications*, volume 3. ASTM International, 2001.

[9] A. Kostka, K. G Tak, R. J. Hellming, Y. Estrin, and G. Eggeler. On the contribution of carbides and micrograin boundaries to the creep strength of tempered martensite ferritic steels. *Acta Materialia*, 55:539–550, 2007.

[10] Rong Hu, George D. W. Smith, and Emmanuelle A. Marquis. Effect of grain boundary orientation on radiation-induced segregation in a Fe-15.2 at.% Cr alloy. *Acta Materialia*, 61:3490–3498, 2013.

[11] K. L. Murty and I. Charit. Structural materials for Gen-IV nuclear reactors: Challenges and opportunities. *Journal of Nuclear Materials*, 383:189–195, 2008.

[12] Shiori Ishino, Naoto Sekimura, Kenta Murakami, and Hiroaki Abe. Some remarks on in-situ studies using TEM-heavy-ion accelerator link from the stand point of extracting radiation damage caused by fast neutrons. *Journal of Nuclear Materials*, 471:167–174, 2016.

[13] Karl Ehrlich. Materials research towards a fusion reactor. *Fusion Engineering and Design*, 56-57:71–82, 2001.

[14] M. J. Swenson and J. P Wharry. The comparison of microstructure and nanocluster evolution in proton and neutron irradiated Fe-9% Cr ODS steel to 3 dpa at 500°C. *Journal of Nuclear Materials*, 467:97–112, 2015.

[15] Z. Yao, M. Hernández-Mayoral, M. L. Jenkins, and M. A. Kirk. Heavy-ion irradiations of Fe and Fe–Cr model alloys Part 1: Damage evolution in thin-foils at lower doses. *Philosophical Magazine*, 88(21):2851–2880, 2008.

[16] Straalsund and F. Garner. 1982.

[17] Computational Materials and Chemical Sciences Network. VI. G. Atomistic Simulations of Radiation Damage in Metals. *http://cmcsn.phys.washington.edu/book/export/html/507*, Last checked 24/08/2016.

[18] Paul C. Painter, John F. Graf, and Micheal M. Coleman. Effect of Hydrogen Bonding on the Enthalpy of Mixing and the Composition Dependence of the Glass Transition Temperature in Polymer Blends. *Macromolecules*, 24(20):5630–5638, 1991.

[19] I. Mirebeau, M. Hennion, and G. Parette. First measurement of short-range-order inversion as a function of concentration in a transition alloy. *Physicsal Review Letters*, 53:687–690, 1984.

[20] G. J. Ackland. Magnetically Induced Immiscibility in the Ising Model of FeCr Stainless Steel. *Physicsal Review Letters*, 97(1):015502, 2006.

[21] Anthony T. Paxton and Micheal W. Finnis. Magnetic tight binding and the iron-chromium enthalpy anomaly. *Physical Review B*, 77:024428, 2008.

[22] Marc Robinson. *Simulating Radiation Damage in Plutonium*. PhD thesis, Department of Mathematical Sciences, Loughborough University, 2010.

[23] Neil W. Ashcroft and N. David Mermin. *Solid State Physics*. Cengage Learning (Brooks/Cole), 1976.

[24] F. A. Garner, M. B. Toloczko, and B. H. Sencer. Comparison of swelling and irradiation creep behavior of fcc-austenitic and bcc-ferritic/martensitic alloys at high neutron exposure. *Journal of Nuclear Materials*, 276:123–142, 2000.

[25] Xu Wang, Qingzhi Yan, Gary S. Was, and Lumin Wang. Void swelling in ferritic-martensitic steels under high dose ion irradiation: Exploring possible contributions to swelling resistance. *Scripta Materialia*, 121:9–14, 2016.

[26] E .A. Little and D. A. Stow. Void-swelling in irons and ferritic steels. *Journal of Nuclear Materials*, 87(1):25 – 39, 1979.

[27] M.L. Jenkins, Z. Yao, M. Hernández-Mayoral, and M.A. Kirk. Dynamic observations of heavy-ion damage in Fe and Fe–Cr alloys. *Journal of Nuclear Materials*, 389:197–202, 2009.

[28] A. Bhattacharya, E. Melsin, J. Henry, C. Pareige, B. Décamps, C. Genevois, D. Brimbal, and A. Barbu. Chromium enrichment on the habit plane of dislocation loops in ion-irradiated high-purity Fe-Cr alloys. *Acta Materialia*, 78:394–403, 2014.

[29] The Engineering ToolBox. Metals - Melting Temperatures. *http://www.engineeringtoolbox.com/melting-temperature-metals-d_860.html*, Accessed Novemeber 2016.

[30] A. Kohyama, A. Hishinuma, D. S. Gelles, R. L. Klueh, W. Dietz, and K. Ehrlich. Low-activation ferritic and martensitic steels for fusion application. *Journal of Nuclear Materials*, 233-237(1):128–147, 1996.

[31] A. Brodyanski, S. Blomeier, H. Gnaser, W. Bock, B. Hillebrands, M. Kopnarski, and B. Reuscher. Interplay of energy dissipation, ion-induced mixing, and crystal structure recovery, and surface effects in ion-irradiated magnetic Fe/Cr/Fe trilayers. *Physical Review B*, 84(214106):1–23, 2011.

[32] Gary S. Was, Jannelle P. Wharry, Brian Frisbie, Brian D Wirth, Dane Morgan, Julie D. Tucker, and Todd R. Allen. Assessment of radiation-induced segregation mechanisms in austenitic and ferritic-martensitic alloys. *Journal of Nuclear Materials*, 411:41–50, 2011.

[33] Katsuki Suganuma, Hideo Kayano, and Seishi Yajima. Mechanical properties changes of Fe-Cr alloys by fast neutron irradiation. *Journal of Nuclear Materials*, 105(1):23–35, 1982.

[34] A. Okada, N. Kawaguchi, M. L. Hamilton, K. Hamada, T. Yoshiie, I. Ishida, and E. Hirota. Mechanical property change in neutron irradiated Fe-Cr and Fe-Mn alloys, and their defect structures. *Journal of Nuclear Materials*, 212-215:382–387, 1994.

[35] M. Matijasevic and A. Almazouzi. Effect of Cr on the mechanical properties and microstructure of Fe-Cr alloys after n-irradiation. *Journal of Nuclear Materials*, 377:147–154, 2008.

[36] Katsuaki Suganuma and Hideo Kayano. Irradiation hardening of fe-cr alloys. *Journal of Nuclear Materials*, 118(2-3):234–241, 1983.

[37] K. Arakawa, M. Hatanaka, H. Mori, and K. Ono. Effects of chromium on the one-dimensional motion of interstitial-type dislocation loops in iron. *Journal of Nuclear Materials*, 329-333(Part B):1194–1198, 2004.

[38] L. Malerba, D. Terentyev, P. Olsson, R. Chakarova, and J. Wallenius. Molecular dynamics simulation of displacement cascades in Fe–Cr alloys. *Journal of Nuclear Materials*, 329(33):1156–1160, 2004.

[39] D.A. Terentyev, L. Malerba, R. Chakarova, K. Nordlund, P. Olsson, M. Rieth, and J. Wallenius. Displacement cascades in Fe–Cr: A molecular dynamics study. *Journal of Nuclear Materials*, 349:119–132, 2005.

[40] C. Björkas, K. Nordlund, L. Malerba, D. Terentyev, and P. Olsson. Simulation of displacement cascades in $Fe_{90}Cr_{10}$ using a two band model potential. *Journal of Nuclear Materials*, 372:312–317, 2008.

[41] A. F. Calder, D. J. Bacon, A. V. Barashev, and Y. N. Osetsky. Effect of mass of the primary knock-on atom on displacement cascade debris in α-iron. *Philosophical Magazine Letters*, 88(1):43–53, 2008.

[42] K. Vörtler, C. Björkas, D. Terentyev, L. Malerba, and K. Nordlund. The effect of Cr concentration on radiation damage in Fe–Cr alloys. *Journal of Nuclear Materials*, 382:24–30, 2008.

[43] D. Terentyev, K. Vörtler, C. Björkas, K. Nordlund, and L. Malerba. Primary radiation damage in bcc Fe and Fe-Cr crystals containing dislocation loops. *Journal of Nuclear Materials*, 417:1063–1066, 2011.

[44] L. Malerba, G. Bonny, D. Terentyev, E. E. Zhurkin, M. Hou, K. Vörtler, and Nordlund K. Microchemical effects in irradiated Fe-Cr alloys as revealed by atomistic simulation. *Journal of Nuclear Materials*, 442:486–498, 2013.

[45] D. Terentyev, G. Bonny, C. Domain, G. Monnet, and L. Malerba. Mechanisms of radiation strengthening in Fe-Cr alloys as revealed by atomistic studies. *Journal of Nuclear Materials*, 442:470–485, 2013.

[46] Oriane Senninger, Frédéric Soisson, Enrique Martínez, and Maylise Nastar. Modeling radiation induced segregation in iron-chromium alloys. *Acta Materialia*, 103:1–11, 2016.

[47] J. Wallenius, P. Olsson, C. Lagerstedt, N. Sandberg, R. Chakarova, and V. Pontikis. Modelling of chromium precipitation in Fe-Cr alloys. *Physicsal Review B*, 69(094103):1–9, 2004.

[48] P. Olsson. *Ab initio* study of interstitial migration in Fe-Cr alloys. *Journal of Nuclear Materials*, 386-388:86–89, 2009.

[49] N. Juslin and K. Nordlund. Molecular dynamics simulations of collision cascades in FeCrHe. *Nuclear Instruments and Methods in Physics Research B*, 267:3420–3423, 2009.

[50] Tomas Lazauskas, Steven D. Kenny, Roger Smith, Gurpreet Nagra, Manan Dholakia, and M. C. Valsakumar. Simulating radiation damage in a bcc Fe system with embedded yttria nanoparticles. *Journal of Nuclear Materials*, 437:317–325, 2013.

[51] A. F. Calder and D. J. Bacon. A molecular dynamics study of displacement cascades in α-iron. *Journal of Nuclear Materials*, 207:25–45, 1993.

[52] R.E. Stoller. *1.11 - Primary Radiation Damage Formation.* Elsevier, Oxford, 2012.

[53] William J. Weber, Dorothy M. Duffy, Lionel Thomé, and Yanwen Zhang. The role of electronic energy loss in ion beam modification of materials. *Current Opinion in Solid State and Materials Science*, 19:1–11, 2015.

[54] Steve Plimpton, Aidan Thompson, Ray Shan, Stan Moore, Axel Kohlmeyer, Paul Crozier, and Mark Stevens. Lammps Molecular Dynamics Simulator. *http://lammps.sandia.gov*.

[55] Chris D.J. Scott. Atoman - analysis and visualisation of atomistic simulations. *https://github.com/chrisdjscott/Atoman*.

[56] J. F. Ziegler, J. P. Biersack, and U. Littmark. *The Stopping and Range of Ions in Matter.* Pergamon, New York/SRIM Company, 1985, 2008 Edition.

[57] James F. Ziegler. James Ziegler - SRIM & TRIM. *http://www.srim.org/*.

[58] William C. Swope, Hans C. Andersen, Peter H. Berens, and Kent R. Wilson. A computer simulation method for the calculation of equilibrium constants for the formation of physical clusters of molecules: Application to small water clusters. *The Journal of Chemical Physics*, 76:637–649, 1982.

[59] H. J. C. Berendsen, J. P. M. Postma, W. F. van Gunsteren, A. DiNola, and J. R. Haak. Molecular dynamics with coupling to an external bath. *Journal of Chemical Physics*, 81(8):3684–3690, 1984.

[60] Philippe H. Hünenberger. Thermostat Algorithms for Molecular Dynamics Simulations. *Advanced Polymer Science*, 173:105–149, 2005.

[61] William G. Hoover. Canonical dynamics: Equilibrium phase-space distributions. *Physical Review A*, 31(3):1695–1697, 1985.

[62] Zainab Al Tooq. *Simulating Radiation Damage in Austenitic Stainless Steel and Ni-based alloys.* PhD thesis, Department of Mathematical Sciences, Loughborough University, 2013.

[63] Murray S. Daw and Michael I. Bakes. Embedded-atom method: Derivation and application to impurities, surfaces, and other defects in metals. *Physical Review B*, 29:6443–6453, 1983.

[64] Murray S. Daw, Stephen M. Foiles, and Michael I. Bakes. Embedded-atom method: Derivation and application to impurities, surfaces, and other defects in metals. *Materials Science Reports*, 9:251–310, 1993.

[65] Pär Olsson, Janne Wallenius, Christophe Domain, Kai Nordlund, and Lorenzo Malerba. Two-band modelling of α–prime phase formation in Fe-Cr. *Physical Review B*, 72(214119):1–6, 2005.

[66] G.J. Ackland, M.I. Medelev, D.J. Stolovitz, S. Han, and A.V. Barashev. Developement of an interatomic potential for phosphorus impurities in α-iron. *Journal of Physics Condensed Matter*, 16:S2629–S2642, 2004.

[67] G. Bonny, R.C. Pasianot, D. Terentyev, and L. Malerba. Interatomic Potential to Simulate Radiation Damage in Fe-Cr Alloys. *Open Report SCK-CEN-BLG-1077 http://publications.sckcen.be/dspace/bitstream/10038/7442/1/blg_1077.pdf*, 2011.

[68] M.I. Mendelev, S. Han, D.J. Stolovitz, G. J. Ackland, D.Y. Sun, and M. Asta. Development of new interatomic potentials appropriate for crystalline and liquid iron. *Taylor & Francis Philosophical Magazine*, 83(35):3977–3994, 2003.

[69] G. Bonny, R.C. Pasianot, D. Terentyev, and L. Malerba. Iron Chromium potential to model high-chromium ferritic alloys. *Taylor & Francis Philosophical Magazine*, 91(12):1724–1746, 2011.

[70] A. Caro, D.A. Crowson, and M. Caro. Classical Many-Body Potential for Concentrated Alloys and the Inversion of Order in Iron-Chromium Alloys. *Physical Review Letters*, 95(075702), 2005.

[71] T. P. C. Klaver, G. Bonny, P. Olsson, and D. Terentyev. Benchmarking FeCr empirical potentials against density functional theory data. *IOP Publishing: Modelling and Simulation in Materials Science and Engineering*, 18:075004, 2010.

[72] T. P. C. Klaver, E. del Rio, G. Bonny, S. M. Eich, and A. Caro. Inconsistencies in modelling interstitials in FeCr with empirical potentials. *Computational Materials Science*, 121:204–208, 2016.

[73] Michael E. Wieser, Norman Holden, Tyler B. Coplen, John K. Böhlke, Michael Berglund, Willi A. Brand, Paul De Bièvre, Manfred Gröning, Robert D. Loss, Juris Meija, Takafumi Hirata, Thomas Prohaska, Ronny Schoenberg, Glenda O'Connor, Thomas Walczyk, Shige Yoneda, and Xiang-Kun Zhu. Atomic weights of the elements 2011 (IUPAC Technical Report). *Pure and Applied Chemistry*, 85(5):1047–1078, 2013.

[74] Magnus R. Hestenes and Eduard Stiefel. Methods of conjugate gradients for solving linear systems. *Journal of Research of the National Bureau of Standards*, 49(6):409–436, 1952.

[75] E. Polak and G. Ribiere. Note sur la convergence de méthodes de directions conjuguées (*In French*). *Revue française d'informatique et et de recherche opérationnelle*, 3(1):35–43, 1969.

[76] Richard H. Byrd, Peihuang Lu, Jorge Nocedal, and Ciyou Zhu. A Limited Memory Algorithm for Bound Constrained Optimization. *Society for Industrial and Applied Mathematics*, 16(5):1190–1208, 1995.

[77] José Luis Morales and Jorge Nocedal. Remark on "algorithm 778: L-BFGS-B: Fortran subroutines for large-scale bound constrained optimization". *ACM Transactions on Mathematical Software (TOMS)*, 38(7), 2011.

[78] SciPy.org. scipy.optimize.fmin_l_bfgs_b -- SciPy v0.18.0 Reference Guide. *http://docs.scipy.org/doc/scipy-0.14.0/reference/generated/scipy.optimize.fmin_l_bfgs_b.html*, August 2011.

[79] Daniel Faken and Hannes Jónsson. Systematic analysis of local atomic structure combined with 3D computer graphics. *Computational Materials Science*, 2:279–289, 1994.

[80] Alexander Stukowski. Structure identification methods for atomistic simulations of crystalline materials. *Modelling and Simulation in Materials Science and Engineering*, 20:045021, 2012.

[81] A. F. Calder, D. J. Bacon, A. V. Barashev, and Yu. N. Osetsky. On the origin of large interstitial clusters in displacement cascades. *Philosophical Magazine*, 90(7-8):863–884, 2010.

[82] Svante August Arrhenius. Über die dissociationswärme und den einfluß der temperatur auf den dissociationsgrad der elektrolyte (*In German*). *Zeitschrift für Physikalische Chemie*, 4:96–116, 1889.

[83] Arthur F. Voter, Francesco Montalenti, and Timothy C. Germann. Extending the Time Scale in Atomistic Simulation of Materials. *Annual Review of Materials Research*, 32:321–346, 2002.

[84] Graeme Henkelman and Hannes Jónsson. Long time scale kinetic Monte Carlo simulations without lattice approximation and predefined event table. *Journal of Chemical Physics*, 115(21):9657–9666, 2001.

[85] George Haller, T. Uzer, Jesús Palacián, Patricia Yanguas, and Charles Jaffé. Transition state geometry near higher-rank saddles in phase space. *IOP Publishing*, 24:527–561, 2011.

[86] M. Chiapetto, C. S. Becquart, C. Domain, and L. Malerba. Kinetic Monte Carlo simulation of nanostructural evolution under post-irradiation annealing in dilute FeMnNi. *Wiley Online Library: Physica Status Solidi C*, pages 1–5, 2014.

[87] George H. Vineyard. Frequency Factors amd Isotope Effects in Solid State Rate Processes. *J. Phys. Chem. Solids*, 3:121–127, 1957.

[88] Tomas Lazauskas. *Simulating Radiation Effects in Iron with Embedded Oxide Nanoparticles*. PhD thesis, Loughborough University, 2014.

[89] netlib.org. Lapck: dsyev. *http://www.netlib.org/lapack/explore-html/d2/d8a/group__double_s_yeigen_ga442c43fca5493590f8f26cf42fed4044.html*, June 2016.

[90] netlib.org. Lapck – Linear Algebra PACKage. *http://www.netlib.org/lapack/*, June 2016.

[91] Graeme Henkelman and Hannes Jónsson. Improved tangent estimate in the nudged elastic band method for finding minimum energy paths and saddle points. *Journal of Chemical Physics*, 113(22):9978–9985, 2000.

[92] Graeme Henkelman, Blas P. Uberuaga, and Hannes Jónsson. A climbing image nudged elastic band method for finding saddle points and minimum energy paths. *Journal of Chemical Physics*, 113(22):9978–9985, 2000.

[93] G. T. Barkema and Normand Mousseau. Event-Based Relaxation of Continuous Disordered Systems. *Philosophical Review Letters*, 77(21):4358–61, 1996.

[94] Wolfram MathWorld. L^2-Norm -- from Wolfram MathWorld. *http://mathworld.wolfram.com/L2-Norm.html*, 2016.

[95] Normand Mousseau and G. T. Barkema. Activated mechanisms in amorphous silicon: An activation-relaxation-technique study. *Physical Review B*, 61(3):1898–1906, 2000.

[96] Louis J. Vernon. *Modelling Growth of Rutile TiO_2.* PhD thesis, Loughborough University, 2010.

[97] Miao Yu. *Modelling CdTe thin film growth over realistic time scales.* PhD thesis, Loughborough University, 2015.

[98] Graeme Henkelman and Hannes Jónsson. A dimer method for finding saddle points on high dimensional potential surfaces using only first derivatives. *Journal of Chemical Physics*, 111(15):7010–7022, 1999.

[99] Charles J. Cerjan and William H. Miller. On Finding Transition States. *Journal of Chemical Physics*, 75(6):2800–2806, 1981.

[100] Andreas Pedersen, Sigurdur F. Hafstein, and Hannes Jónsson. Efficient sampling of saddle points with the minimum-mode following method. *SIAM Journal on Scientific Computing*, 33(2):633–652, 2011.

[101] Cornelius Lanczos. An Iteration Method for the Solution of the Eigenvalue Problem of Linear Differential and Integral Operators. *Journal of Research of the National Bureau of Standards*, 45(4):255–282, 1950.

[102] C. C. Paige. Computational Variants of the Lanczos method for the Eigenproblem. *Journal of the Institute of Mathematics and its Applications*, 10:373–381, 1972.

[103] netlib.org. QR Factorization. *http://netlib.org/lapack/lug/node40.html*, October 1999.

[104] James M. Ortega and Henry F. Kaiser. The LL^T and QR methods for symmetric tridiagonal matrices. *The Computer Journal*, 6(1):99–101, 1963.

[105] Brendan D. McKay. Practical graph isomorphism. *10^{th} Manitoba Conference on Numerical Mathematics and Computing (Winnipeg, 1980); Congressus Numerantium*, 30:45–87, 1981.

[106] Brendan D. McKay and Adolfo Piperno. *nauty* and *Traces* User's Guide (Version 2.5). *http://users.cecs.anu.edu.au/∼bdm/nauty/nug25.pdf*, January 2013.

[107] Brian Puchala, Michael L. Falk, and Krishna Garikipati. An energy basin finding algorithm for kinetic Monte Carlo acceleration. *The Journal of Chemical Physics*, 132(134104):1–14, 2010.

[108] Kristen A. Fichthorn and Yangzheng Lin. A local superbasin kinetic Monte Carlo method. *The Journal of Chemical Physics*, 138(164104):1–11, 2013.

[109] Laurent Karim Béland, Peter Brommer, Fedwa El-Mellouhi, Jean-François Joly, and Normand Mousseau. Kinetic activation-relaxation technique. *Physical Review E*, 84(046704), 2011.

[110] M. Robinson, N. A. Marks, K. R. Whittle, and G. R. Lumpkin. Systematic calculation of threshold displacement energies: Case study in rutile. *Physical Review B*, 85(104105):1–11, 2012.

[111] R. Chakarova, V. Pontikis, and J. Wallenius. Development of FeCr many body potential and cohesion model. *Delivery Report WP 6 - SPIRE project, EC contract №FIKW-CT-2000-00058*
www. neutron.kth.se/publications/library/DR-6.pdf, 2002.

[112] P. Olsson, L. Malerba, and A. Almazouzi. A first step towards a multiscale modelling of Fe–Cr alloys. *SCKCEN Report, BLG-950*, 2003.

[113] Email conversation with Chris Cooper. *Materials Degradation in Energy Systems Research Grouo, School of Metallurgy and Materials, College of Engineering and Physical Sciences, University of Birmingham*, September 2015.

[114] Mark T. Robinson and Ian M. Torrens. Computer simulation of atomic-displacement cascades in solids in the binary-collision approximation. *Physical Review B*, 9(12):5008–5024, 1974.

[115] SR-NIEL. Electronic Stopping Power and Ionizing Dose Calculators for Protons & Ions. *www.sr-niel.org/index.php/electronic-stopping-power-and-ionizing-dose-calculators-for-protons-ions*, 2015.

[116] J. Nord, K. Nordlund, and J. Keinonen. Molecular dynamics study of damage accumulation in GaN during ion beam irradiation. *Physical Review B*, 68(184104), 2003.

[117] Radiation Safety Information Computational Center Oak Ridge National Laboratory. Rsicc catalog (*See MCNP-DSP and MCNPX-POLIMI*). *https://rsicc.ornl.gov/Catalog.aspx*, 2016.

Chapter 8

Appendix

Catalogue of Paper Corrections

In the various source papers used for the potentials used in this investigation, there are a number of errors which must be accounted for in order to use them.

Olsson 2005/Ackland 2004

- The ζ_s coefficient is given incorrectly and should be 2.5 Å^{-1}.
- The a_2 coefficient is incorrectly given as negative, where it should be positive.
- The substitutional energy for potential A given in Table IV should be -0.26 eV.
- NB: In the tabulated data provided for this potential, Bonny uses Kelvin-based units to represent energies. Since we work in electron volts, one has to multiply his V and F values by the Boltzmann Constant, 8.617×10^{-5}eV K^{-1}
- The values given for the pairwise term in Table III are given in terms of a lattice parameter where they should be given in terms of the corresponding nearest-neighbour distance. The correct reference value is 2.4777 Å

Bonny 2011/Mendelev 2003

- Looking at the tabulated data provided by Bonny, transformations are applied to tabulated data. Therefore one may use the tabulations as they are and as they appear in the equations. However, contrary to as implied in the paper, the transformations are not applied to the mixed case functions.

- In Bonny's papers, it appears that he sets the transformation constant, C as $\frac{\mathrm{d}}{\mathrm{d}\rho}F(\rho_{\mathrm{eq}})$, but in fact he uses $C = -F(\rho_{\mathrm{eq}})$. This is not actually a mistake in the paper, but a confusing choice of notation.

- The formula used for the s-band in the paper is incorrect and returns values a factor of five too small. It should be:

$$\phi_s(r_{ij}) = \frac{\left(N_s r_{ij}^3 \exp[-\frac{\zeta_s r_{ij}}{r_b}]\right)^2}{S} \tag{8.1}$$

  where $N_s = 5$, $\zeta_s = 1.323$, $S = 0.245811927$ and R_b is the Bohr Radius, 0.529177210818181818 Å. Alternatively, one can correct the formula by using it as given, but with $K = 101.703771273881$ and $\zeta_s = 2.50010766328062$.

- In the source paper for the pure iron potential, Mendelev 2003, the 7^{th} coefficient for the pairwise term, a_7^{φ}, should be negative.

- There is a typographical error in the formula used for chromium's ϕ_d term given in the paper. One should replace the φ_0 term with $\frac{1}{\varphi_0}$.

- For chromium's ϕ_d, x_{cut} is given incorrectly and should be $x_{\mathrm{cut}} = 1.65$

- The coefficients for V_{FeCr} are *all* sign flipped.